

**The Microstructures and Mechanical Properties of Powder Metallurgy
(PM) Ti-48Al-2Cr-2Nb-(0-1)W**

By

Scott W. Bulmer, B.Eng.

A thesis submitted to
The Faculty of Graduate Studies and Research
in partial fulfilment of
the degree requirements of
Master of Applied Science

Ottawa-Carleton Institute for
Mechanical and Aerospace Engineering

Department of Mechanical and Aerospace Engineering
Carleton University
Ottawa, Ontario, Canada
Sept 2008

Copyright ©
2008 – Scott W. Bulmer



Library and
Archives Canada

Published Heritage
Branch

395 Wellington Street
Ottawa ON K1A 0N4
Canada

Bibliothèque et
Archives Canada

Direction du
Patrimoine de l'édition

395, rue Wellington
Ottawa ON K1A 0N4
Canada

Your file *Votre référence*
ISBN: 978-0-494-44033-9
Our file *Notre référence*
ISBN: 978-0-494-44033-9

NOTICE:

The author has granted a non-exclusive license allowing Library and Archives Canada to reproduce, publish, archive, preserve, conserve, communicate to the public by telecommunication or on the Internet, loan, distribute and sell theses worldwide, for commercial or non-commercial purposes, in microform, paper, electronic and/or any other formats.

The author retains copyright ownership and moral rights in this thesis. Neither the thesis nor substantial extracts from it may be printed or otherwise reproduced without the author's permission.

AVIS:

L'auteur a accordé une licence non exclusive permettant à la Bibliothèque et Archives Canada de reproduire, publier, archiver, sauvegarder, conserver, transmettre au public par télécommunication ou par l'Internet, prêter, distribuer et vendre des thèses partout dans le monde, à des fins commerciales ou autres, sur support microforme, papier, électronique et/ou autres formats.

L'auteur conserve la propriété du droit d'auteur et des droits moraux qui protègent cette thèse. Ni la thèse ni des extraits substantiels de celle-ci ne doivent être imprimés ou autrement reproduits sans son autorisation.

In compliance with the Canadian Privacy Act some supporting forms may have been removed from this thesis.

Conformément à la loi canadienne sur la protection de la vie privée, quelques formulaires secondaires ont été enlevés de cette thèse.

While these forms may be included in the document page count, their removal does not represent any loss of content from the thesis.

Bien que ces formulaires aient inclus dans la pagination, il n'y aura aucun contenu manquant.

■*■
Canada

Abstract

Titanium Aluminides have in more recent years come under intensive research due to their promising characteristics, light weight and high temperature properties. Envisaged usages include high pressure compressor blades and low pressure turbine blades in aero engines. This thesis elucidates the effects of W additions to a base alloy Ti-48Al-2Cr-2Nb (at. %). After an optimised step cooled heat treatment of 1400 °C for 40 min, followed by furnace cooling to 1270 °C and subsequent air cooling to room temperature, aging conditions ranging from 8 to 472 hrs were examined. Aging produces a stabilized microstructure with precipitate formation along lamellar interfaces and grain boundaries in W containing alloys. Discontinuous and continuous coarsening occur as well, however, W additions reduce the severity. Hardness, tensile and creep testing also revealed improvements with W additions and aging. However, decreased ductility was observed in the tensile tests with increased W and aging.

Acknowledgements

I would foremost like to thank my two thesis supervisors, Dr. Henry Saari and Dr. Dongyi Seo who have both provided me with invaluable guidance and support. Support from my family and friends through this process has also been excellent and I am indebted to you all. I would also like to thank a number of people from the National Research Council of Canada where I completed the majority of work. Dave Morphy, Olga Lupandina, Luke and Pascal Lafleur, and Ryan MacNeil all helped me in their own areas of expertise. A special thanks goes out to Peter L'Abbe for encapsulating the large number of my samples in quartz tubes, our discussion were always enjoyable. Finally, I have to thank my co-conspirators, Tom Henhoeffler and Aleks Wisniewski who made the long hours spent at Carleton University and the National Research Council always enjoyable.

Table of Contents

Abstract	iii
Acknowledgements	iv
Table of Contents	v
List of Tables	ix
List of Figures	xi
Nomenclature	xxi
Chapter 1: Introduction	1
Chapter 2: γ-TiAl Overview	5
2.1 Microstructure.....	7
2.1.1 Duplex.....	10
2.1.2 Fully Lamellar.....	13
2.1.3 Effects of Microstructure on Mechanical Properties	14
2.1.3.1 Grain Size and Boundary Morphology.....	15
2.1.3.2 Lamellar Spacing.....	19
2.1.3.3 Precipitates	21
2.1.3.4 Deleterious Phases.....	22

2.1.4 Microstructural Control	28
2.2 Alloying	30
2.2.1.1 Al Sensitivity	33
2.2.1.2 Cr and Nb Additions	34
2.2.1.3 W Additions	35
2.3 Deformation Modes	36
2.3.1 Creep	37
2.3.1.1 Power Law Relationship	37
2.3.1.2 Diffusional Creep	38
2.3.1.3 Dislocation Creep	40
2.3.1.4 Creep in TiAl	41
2.3.2 Tensile	44
2.4 Summary	45
Chapter 3: Thesis Objectives and Scope.....	46
Chapter 4: Experimental Details.....	48
4.1 Sample Production	49
4.1.1 Powder Materials	49
4.1.2 HIP Processes.....	49
4.1.3 Heat Treatments	53
4.1.3.1 Step Cooled Heat Treatment (SCHT).....	53
4.1.3.2 Aging.....	56
4.2 Metallography	57

4.2.1 Sample Preparation	57
4.2.2 Microstructural Analysis Techniques	63
4.2.2.1 OM, SEM and TEM Analysis	63
4.2.2.2 Equiaxed γ Measurements	66
4.2.2.3 γ_m Measurements	66
4.2.2.4 Grain Size Measurements	67
4.3 Mechanical Testing Procedures	67
4.3.1 Sample Preparation	67
4.3.2 Hardness	69
4.3.3 Tensile	69
4.3.4 Creep	70
Chapter 5: Results and Discussion	74
5.1 Microstructural Analysis	74
5.1.1 As HIP'ed Condition	74
5.1.2 Step Cooled Heat Treatment (SCHT)	76
5.1.2.1 Effect of Hold Time above the α -Transus	77
5.1.2.2 Effect of Transition Temperature ($T_{F/A}$)	81
5.1.3 Aging	87
5.1.3.1 Equiaxed γ and Discontinuous Coarsening	87
5.1.3.2 Continuous Coarsening and Lamellar Thickness	92
5.1.3.3 Precipitates	103
5.2 Micro-Hardness Data	119
5.3 Mechanical Testing	126

5.3.1 Creep Testing	126
5.3.2 Tensile Testing.....	151
Chapter 6: Summary and Conclusions	163
6.1 Future Research	166
References	169

List of Tables

Table 1 - Effects of different alloying elements	31
Table 2 - Compositional analysis provided by Crucible Research on the powders used for this study	49
Table 3 - Thermal processing summary for samples not encased in quartz tubes.....	55
Table 4 - Thermal processing summary for samples encased in quartz tubes.....	56
Table 5 - TiAl etchant composition	59
Table 6 - Electro-polishing solution	60
Table 7 - Twin-jet polishing parameters	61
Table 8 – Semi-quantitative SEM-EDS results after the optimized solution heat treatment, average of 5 large area scans for each composition (40 min hold time, $T_{F/A}$ of 1270 °C) 87	
Table 9 - Average Lamellar Spacing (nm)	102
Table 10 - TEM-EDS results from point scans on small precipitates at the lamellar interfaces on the 1%W alloy	112
Table 11 - TEM-EDS results from point scans on large precipitates at the lamellar interfaces on the 1%W alloy	112
Table 12 - SEM-EDS results from point scans on large precipitates at the lamellar interfaces on the 1%W alloy	113

Table 13 - SEM-EDS results from point scans on large precipitates at the lamellar interfaces on the 0.5%W alloy	113
Table 14 - Creep results comparing unaged and isothermally aged times only	134
Table 15 - Instantaneous Strain (%).....	135
Table 16 – Minimum Creep Strain Rate (%/sec).....	135
Table 17 - Total Creep Life (hrs).....	135
Table 18 - Creep results comparing stepped aging to the isothermally aged 8 hr sample	145
Table 19 - Summary of tensile data	152

List of Figures

Figure 1 – Illustration of a high bypass ratio turbofan engine. Modified from [7].....	2
Figure 2 - The ordered crystal lattice structures for a) $D0_{19}$ HCP and b) $L1_0$ FCT [1]	6
Figure 3 - Ordered BCC B2 unit cell.....	6
Figure 4 - Relevant section for the binary phase diagram for titanium and aluminum [2].	7
Figure 5 - a) Duplex; b) Near γ (NG); c) Nearly Lamellar (NL); d) Fully Lamellar (FL) [20].....	8
Figure 6 - Binary phase diagram from [2] with heat treatment temperatures used to develop particular microstructures marked; FL: Fully Lamellar, NL: Nearly Lamellar, D: Duplex, NG: Near Gamma	9
Figure 7 - Effect of decreasing equiaxed gamma content on creep [26]	11
Figure 8 - Plot showing the temperature dependence of fracture toughness on temperature for the fully lamellar (FL), near gamma (NG) and duplex (D) microstructures [5]	12
Figure 9 - Data showing how different microstructures retain their properties at high temperatures [5] (Duplex have the lowest brittle-to-ductile transition temperature (T_{bd}) while FL has the highest) (temperatures range from about ~ 620 °C up to ~ 800 °C)(as ϵ increases, so does T_{bd} , indicating T_{bd} is controlled by thermally activated process).....	12

Figure 10 - Illustration and TEM micrograph of the FL microstructure with alternating γ and α_2 phases (TEM micrograph from [28])	13
Figure 11 - Work from Beddoes et al. showing grain size growth compared to isothermal heat treatment time [37]	16
Figure 12 - Plot demonstrating the effects of decreasing grain size. Base material was Ti-47Al-1Cr-1V-2.5Nb (at.%) with a FL microstructure (Modified from [5])	17
Figure 13 - Work from Au demonstrating the effects of decreasing grain size on minimum creep rates. (Tested at 760 °C and 240 MPa) [21]	18
Figure 14 - Illustration of the two types of grain boundaries, interlocking (a) and planar (b), indicated by arrows [18].....	19
Figure 15 - Massively transformed γ [58].....	23
Figure 16 - Partial phase diagram for the binary Ti-Al system [57].....	25
Figure 17 - OM showing the feathery microstructure (Fy) along with Widmanstätten laths (Wid) and typical lamellae (Lamellar) [32]	27
Figure 18 - Widmanstätten microstructure (Wid) formed within a fully lamellar colony [32]	27
Figure 19 – An optical microscope (OM) micrograph of a near stoichiometric cast alloy [2]	29
Figure 20 - Effect of varying Al content on plastic elongation with various heat treatments [76]	33

Figure 21 - Effect of varying Al content on yield strength with various heat treatments [76].....	34
Figure 22 - Results from a cyclic oxidation test at 850 °C with 1 hr cycles in air [70, 75]	35
Figure 23 - Creep deformation map [84]	41
Figure 24 - Creep curves of a Ti-48Al-2W alloy in the unaged (0hrs) condition as well as multiple aging times (24, 48, 96 and 192 hrs) [18].....	44
Figure 25 - Glove box with an argon atmosphere where the powder metal was stored ...	50
Figure 26 - Stainless steel tube sealed at one end, filled with TiAl powder and closed at the other end with a section of rubber glove to minimize oxygen contamination during transport from the glove box to the vacuum	50
Figure 27 - Steel tubes connected to the vacuum being degassed at 350 °C.....	51
Figure 28 - Stainless steel tubes with TiAl powder sealed inside under a vacuum prior to HIP'ing	52
Figure 29 - TiAl after HIP'ing, the sample on top is still clad in the stainless steel tube while the sample on the bottom has been de-canned.....	53
Figure 30 - Illustration of the stepped cooling process during the Step Cooled Heat Treatment (SCHT)	54
Figure 31 - Illustration of the stepped aging process.....	57
Figure 32 - Buehler IsoMet 2000 with a diamond wafering blade	58
Figure 33 - Polishing wheels for metallographic samples.....	58

Figure 34 - Struers Polipower, used to electro-polish SEM samples	59
Figure 35 - Electro-polishing setup.....	60
Figure 36 - Illustration showing the cut to produce SEM and OM samples.....	62
Figure 37 - Illustration showing the product of the axial and transverse cuts described above	62
Figure 38 – Olympus PMG-3 optical microscope	63
Figure 39 – Philips XL30S FEG equipped with an EDAX from Phoenix Systems	64
Figure 40 - Philips EM430 STEM	65
Figure 41 - Jeol JEM-2100F field emission electron microscope	65
Figure 42 - Detailed creep and tensile sample dimensions.....	68
Figure 43 - Machined tensile / creep specimen	68
Figure 44 - Leco microhardness tester (LM-247AT)	69
Figure 45 - Constant load creep frame.....	71
Figure 46 - Satec extensometers; a) single LVDT extensometer (RT-214) and b) dual LVDT extensometer (DA-214).....	72
Figure 47 - Creep specimen with two thermocouples attached	72
Figure 48 - SEM-BSE micrograph of the 1%W sample HIP'ed for 2 hrs at 1200 °C and 200 MPa (SEM-EDS results from area (a) found in Figure 50).....	75
Figure 49 - Optical micrograph of the 1%W sample HIP'ed for 2 hrs at 1200 °C and 200 MPa.....	75

Figure 50 - SEM-EDS results from the 1%W sample (in at. %) after HIP'ing (Taken from area (a) in Figure 48).....	76
Figure 51 - SEM-BSE micrographs of a) 0%W, b) 0.5%W, and c) 1%W taken after 1400 °C for 20 min with $T_{F/A} = 1270$ °C. Bright spots (arrows) are W and Cr rich areas.	78
Figure 52 - SEM-EDS results from the 1%W samples (in at.%) after 1400 °C for 20 min with $T_{F/A} = 1270$ °C.	79
Figure 53 - SEM-BSE micrographs of a) 0%W, b) 0.5%W, and c) 1%W taken after 1400 °C for 40 min with $T_{F/A} = 1270$ °C. Bright spots (arrows) are W and Cr rich areas.	80
Figure 54 - Comparison of optical micrographs in the SCHAT condition with hold times of 20 and 40 min.....	81
Figure 55 - Optical micrographs illustrating the effects of varying transition temperature and composition. Arrows indicate γ_m	82
Figure 56 - Volume percent of massive gamma produced during cooling while varying the transition temperature	83
Figure 57 - Possible phase diagram shift due to W additions. ΔT indicates the temperature reduction caused by the shift in the T_o line. Modified from [57]	85
Figure 58 - Optical micrographs showing a comparison of the different aging times. Arrows indicate equiaxed γ formation.	89
Figure 59 - Volume fraction of equiaxed γ in each of the aging conditions.....	90
Figure 60 - SEM images comparing 8 and 144 hr aging times. Arrows show break up of lamellae	93

Figure 61 - TEM micrographs with arrows indicating coarsening a) 0%W aged for 8 hrs, b) 0%W aged for 144 hrs, c) 1%W aged for 8 hrs, d) 1%W aged for 144 hrs	94
Figure 62 - SEM-BSE micrograph showing the spheroidized α_2 lamellae (arrows) in the 0%W sample after aging for 432 hrs.	95
Figure 63 - SEM-EDS results from the 0%W sample after aging for 432 hrs showing the spheroidized α_2 lamellae	96
Figure 64 - SEM micrographs of the 0%W alloy after a) isothermal 8 hrs aging, b) stepped aging (~50 hrs) and c) isothermal 72 hrs aging.	97
Figure 65 - Illustration of two coarsening modes for γ lamellae under different aging conditions; (a) Longitudinal dissolution (movement of ledges) at lower temperatures changing to lateral dissolution (diffusion across α_2/γ interfaces) at higher temperatures (resembles stepped aging), (b) Lateral dissolution [35].....	98
Figure 66 - Line scan across a prior α_2 lamellae in the 1%W alloy after 8 hrs aging.....	100
Figure 67 - Line scan across a prior α_2 lamellae in the 1%W alloy after 144 hrs aging.	100
Figure 68 - Relationship between average lamellar spacing and aging time.....	102
Figure 69 - SEM-BSE micrographs showing precipitate density after aging (All micrographs at the same magnification).....	104
Figure 70 - TEM micrographs from lamellar interfaces showing precipitate formation (Please note the 0.5%W samples aged for 8 and 72 hrs are much closer to an edge on orientation than the others)	105

Figure 71 - Dark field TEM micrograph from the 1%W sample aged for 72 hrs showing precipitates	106
Figure 72 - SEM-BSE micrograph showing the precipitates at the grain boundary (arrows) and lamellar interfaces in a 1%W sample aged for 144 hrs	107
Figure 73 – TEM-BF image showing both the large and small precipitates in the 1%W sample after 72 hrs aging	108
Figure 74 - Angular dark field (ADF) TEM image from the 1%W alloy aged for 72 hrs showing large (arrows) and small precipitates.....	108
Figure 75 - TEM-EDS line scan results from the 1%W alloy after the SCHT. Arrows indicate increased W and Cr concentrations near the α_2/γ interfaces.	110
Figure 76 - TEM-EDS line scan results of the 1%W sample following the SCHT + 8 hrs aging. Line scan is across a precipitate.....	111
Figure 77 - TEM-EDS line scan results of the 1%W sample following the SCHT + 144 hrs aging. Line scan is across a precipitate. Arrows indicate a small deficit in W and Cr near the β/γ interfaces	111
Figure 78 - Excited volumes from SEM and TEM-EDS analysis.....	114
Figure 79 - Logarithmic plot of data presented in Table 11	115
Figure 80 - Comparison of 1%W samples. Top - Stepped aging. Bottom - Aged 72 hrs	117

Figure 81 - TEM-BF micrograph showing the lamellar region of a 1%W alloy aged for 72 hrs which contains both large and small precipitates. Arrows indicate a rare instance of the small and large precipitates on the same lamellar interface.	119
Figure 82 - Vickers micro-hardness test results against aging time	120
Figure 83 - Vickers micro-hardness test results against log aging time	121
Figure 84 - Constant load creep curves generated by testing samples at 760 °C and 276 MPa.....	127
Figure 85 - Constant load creep curves generated by testing samples at 760 °C and 276 MPa (0 – 40 hrs)	127
Figure 86 - Constant load creep curves generated by testing samples at 760 °C with a 276 MPa load (0 – 2 hrs).....	128
Figure 87 - Creep curves of 0%W alloys with different aging conditions (760 °C and 276 MPa load).....	128
Figure 88 - Creep curves of 0.5%W alloys with different aging conditions (760 °C and 276 MPa load).....	129
Figure 89 - Creep curves of 1%W alloys with different aging conditions (760 °C and 276 MPa load).....	129
Figure 90 - Creep curves of the alloys in the unaged condition (760 °C and 276 MPa load)	130
Figure 91 - Creep curves of the alloys after 8 hrs isothermal aging (760 °C and 276 MPa load)	130

Figure 92 - Creep curves of the alloys after 144 hrs isothermal aging (760 °C and 276 MPa load).....	131
Figure 93 - Creep curves of the alloys after stepped aging (760 °C and 276 MPa load)	131
Figure 94 - OM micrographs showing cracking in the 0%W sample after creep testing in the a) unaged, b) aged for 8 hrs, c) stepped aging, and d) aged for 144 hrs conditions. Loading was in the vertical direction on the page.	137
Figure 95 - OM micrographs showing cracking in the 0.5%W sample after creep testing in the a) unaged, b) aged for 8 hrs, c) stepped aging, and d) aged for 144 hrs conditions. Loading was in the vertical direction on the page.	138
Figure 96 - OM micrographs showing cracking in the 1%W sample after creep testing in the a) unaged, b) aged for 8 hrs, c) stepped aging, and d) aged for 144 hrs conditions. Loading was in the vertical direction on the page.	139
Figure 97 - As crept 0%W sample aged for 144 hrs. Arrows indicate wavy lamellae...	140
Figure 98 - SEM micrographs of the 1%W sample after creep testing in the a) unaged, b) aged for 8 hrs, c) stepped aging, and d) aged for 144 hrs conditions	141
Figure 99 - 1%W unaged before creep testing, no precipitates visible	141
Figure 100 - TEM images taken of the 1%W sample after creep testing in the a) unaged, b) aged for 8 hrs and c) aged for 144 hrs conditions. Small precipitates indicated by short arrows and large precipitates indicated by long arrows.....	142
Figure 101 - Creep curves from each alloy comparing the 8 hrs aged and stepped aged conditions (760 °C and 276 MPa load).....	146

Figure 102 - Void nucleation comparison after creep in the 1%W alloy a) 8 hrs aging, b) stepped aging 151

Figure 103 – Stress and strain curves for the three alloys in the unaged and aged for 8 hrs conditions..... 152

Figure 104 - Low and high magnification SEM-SE micrographs of the 0%W sample unaged (left column) and aged for 8 hrs (right column)..... 156

Figure 105 - Low and high magnification SEM-SE micrographs of the 0.5%W sample aged for 8 hrs. Arrow indicates de-lamination..... 157

Figure 106 - Low and high magnification SEM-SE micrographs of the 1%W sample unaged (left column) and aged for 8 hrs (right column). Arrow indicates de-lamination. 158

Figure 107 - 0%W alloy aged for 8 hrs showing a distinct cleavage river pattern. Arrow indicates direction of crack propagation 160

Figure 108 - Fracture surface of a FL thin tensile test specimen with microcracks encircled with a black line. Microcracks comprise 29% of the fracture surface [97] 161

Figure 109 - Delamination occurring ahead of the crack tip [99]..... 162

Nomenclature

- α - Alpha phase (unordered HCP D0₁₉ crystal)
- α_2 - Alpha 2 phase (ordered HCP D0₁₉ crystal)
- $\dot{\epsilon}$ - Strain rate
- $\dot{\epsilon}_{min}$ - Minimum strain rate
- γ - Gamma phase (ordered FCT L1₀ crystal)
- γ' - Lamellar gamma
- γ_m - Massively transformed γ
- λ_L - Lamellar spacing
- T_α - α transus temperature
- T_{bd} - Brittle-to-ductile transition temperature
- $T_{F/A}$ - Stepped cooling transition temperature
- T_m - Melting temperature
- ADF - Angular dark field
- ASTM - American Society for Testing and Materials
- BF - Bright field
- BSE - Back scattered electron
- CCD - Charge-coupled device

DAQ - Data acquisition system

DF - Dark field

DSC - Differential scanning calorimetry

EDS - Energy dispersive spectroscopy

FCT - Face centered tetragonal

FEG - Field emission gun

FL - Fully lamellar

GB - Grain boundary

HCP - Hexagonal close packed

HIP - Hot isostatic press

HPC - High pressure compressor

LPT - Low pressure turbine

LVDT - Linear variable displacement transducer

NG - Near gamma

NL - Nearly lamellar

OM - Optical microscope

SAD - Selected area diffraction

SCHT - Step cooled heat treatment

SE - Secondary electron

SEM - Scanning electron microscope

SHT - Solution heat treatment

STEM - Scanning transmission electron microscope

TEM - Transmission electron microscope

TIG - Tungsten inert gas

Chapter 1: Introduction

The aviation industry, since its beginning over a century ago, has been constantly striving for improvements to aircraft. In a commercial setting, the main driving force has been to improve profit margins. To help achieve this goal, aircraft have been increasing in size and carrying capacity, which in turn has required more thrust from engines. Since the introduction of the jet engine in the late 1930's and early 1940's, the thrust to weight ratio has been steadily improving. Titanium aluminides offer an avenue to continue this trend by providing further weight reductions over their superalloy counterparts and have come under the spotlight for this reason [1-3]. Depending on exact compositions, the density for titanium aluminides is roughly half that of heavier superalloys, weighing only 4 g/cm^3 [4]. These new alloys are being investigated for uses in aero engines to replace the high pressure compressor (HPC) and low pressure turbine (LPT) blades. Weight savings are not limited to the lighter blades alone but will also come by reducing the mass of any other components such as discs, shafts, bearing and support structures. Advantages of TiAl include low density, high specific strength, high specific stiffness, retention of properties at higher temperatures (700 – 800 °C) and compared to typical titanium alloys, a much better resistance to titanium fire [5]. In addition, TiAl alloys also have improved coefficients of thermal expansion compared to regular titanium alloys which is beneficial

in reducing thermal fatigue in jet engines [6]. TiAl could be a suitable replacement for the blades on some select stages within the jet engine, in particular, the HCP and the LPT, where temperatures and stresses are suitable for these alloys. Figure 1 shows a schematic of a high bypass ratio turbofan engine with the compressor and turbine stages labelled.

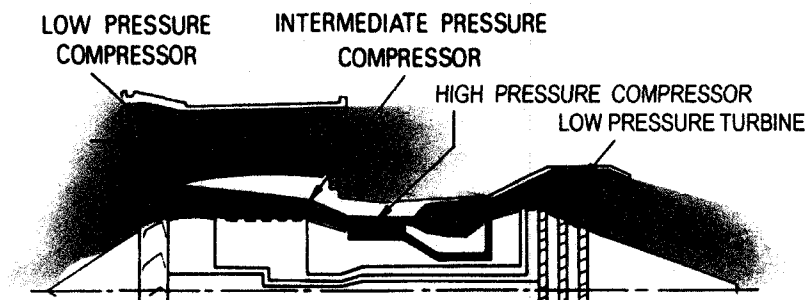


Figure 1 – Illustration of a high bypass ratio turbofan engine. Modified from [7]

General Electric (GE) and Rolls Royce have both been investigating these alloys to design newer engines that consume less fuel and pollute less, lowering both noise and emissions. GE has been testing their newest engine, the GENx with TiAl blades in stages 6 and 7 of the low pressure turbine [8]. Currently there are two variations, the GENx-1B which is designed for the new Boeing Dreamliner and the GENx-2B which is slated for the Boeing 747-8 [9, 10]. The GENx-1B received FAA certification March 31, 2008 [11].

Other applications for TiAl include turbocharger blades and valves for automotive internal combustion engines [12-16]. Motivation for using these materials is increased operating efficiency and decreased emissions.

Motivation for this thesis comes from the need to improve the primary creep of the alloys under investigation. Fully lamellar microstructures have superior minimum strain rates compared to the more ductile duplex microstructure; however, they can sometimes

have worse primary creep [1]. The need to improve primary creep properties in the fully lamellar condition is paramount since many applications are limited to 1% strain or less. If the primary creep can be shortened and the minimum strain rate achieved sooner, then time to 1% strain can be increased to more favourable levels. In the fully lamellar condition, the high primary strain has been attributed to the high number of dislocations emitted from the lamellar interfaces [1]. Therefore, to improve the primary strain, it would seem beneficial to limit the dislocation motion and generation at lamellar interfaces. A number of studies have shown that W additions form precipitates at the lamellar interfaces, which has the desired effect on primary creep [17-19].

The objective of this thesis is to investigate the effect of W on the microstructure and mechanical properties of the GE Ti-48Al-2Cr-2Nb (at. %) (48-2-2) alloy in powder metallurgy form. GE is currently using their 48-2-2 alloy in a cast form for the low pressure turbine blades of their GENx engine. The materials under examination are Ti-48Al-2Cr-2Nb-xW where $x = 0, 0.5$ and 1 at. % (unless otherwise specified, all compositions will be given in at. %). It is expected that by adding the W additions, mechanical properties of the base fully lamellar microstructure could be improved. By improving creep life or temperature capabilities, costs can be reduced by increasing intervals between inspections and replacement or by increasing operating temperatures.

An in depth discussion of background information follows, which will highlight the technical aspects of TiAl. A description of the thesis objectives will then be given

followed by the experimental details. The results and discussion are presented after this and summarized in the summary and conclusion section.

Chapter 2: γ -TiAl Overview

An overview of TiAl will be given, which will cover the different phases present and the respective crystallography as well as properties. A discussion on the different microstructures that can be produced through different thermal treatments follows as well as a description of compositional effects. The different deformation modes will then be covered and an ideal microstructure will be described at the end of this section. The focus of this thesis is on the Ti-48Al-2Cr-2Nb alloy with a fully lamellar microstructure and the literature review will focus on this microstructure as well. In addition to this, the duplex microstructure will be briefly discussed since the original Ti-48Al-2Cr-2Nb alloy created by GE is in a cast duplex condition.

Titanium aluminides are composed primarily of two intermetallic phases, alpha-2 (α_2) and gamma (γ). The α_2 phase is an ordered intermetallic with a DO_{19} hexagonal close packed (HCP) structure composed of Ti_3Al . It remains ordered until 1125 °C. The γ phase is also ordered, however, it has an $L1_0$ face centered tetragonal (FCT) structure composed of TiAl and it will remain ordered until melting at 1440 °C. Because of the ordering, the FCT crystal has a c/a ratio of 1.02 at a stoichiometric composition and varies between 1.01 and 1.03 if Al content is either decreased or increased, respectively

[6]. Each of the crystal structures are illustrated in Figure 2. In addition to the two phases present in the binary system, a third β phase can be stabilised by the addition of appropriate ternary elements. The β phase forms as an ordered BCC B2 unit cell as shown in Figure 3. The volume fraction of the α_2 and γ phases depends on the Al content. Figure 4 shows the relevant section within the Ti-Al phase diagram highlighting the compositional range of engineering importance [3].

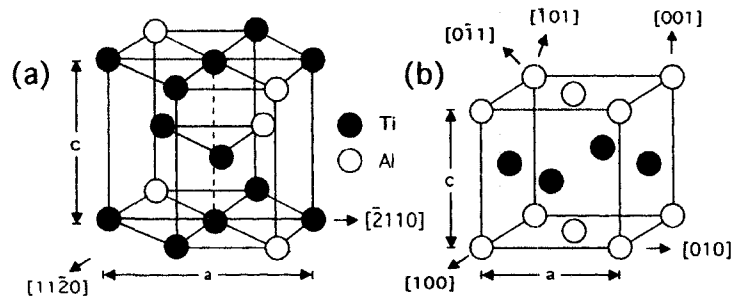


Figure 2 - The ordered crystal lattice structures for a) $D0_{19}$ HCP and b) $L1_0$ FCT [1]

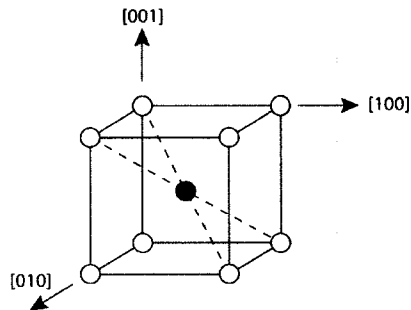


Figure 3 - Ordered BCC B2 unit cell

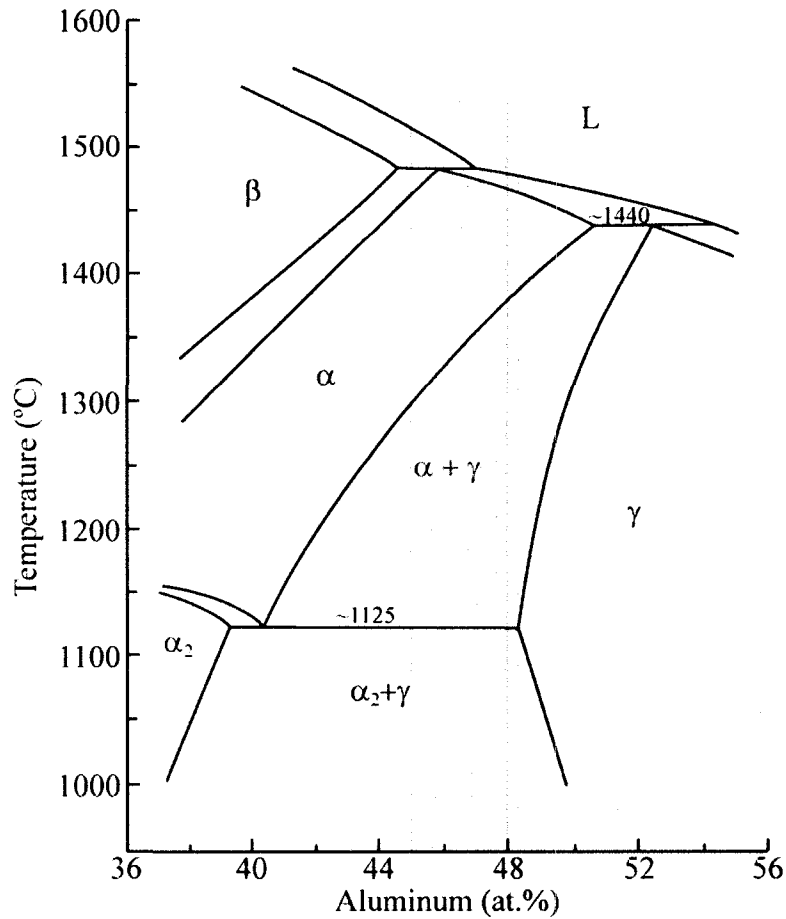


Figure 4 - Relevant section for the binary phase diagram for titanium and aluminum [2]

2.1 Microstructure

There are four main microstructures which can be developed through different heat treatments: duplex, near γ (NG), near lamellar (NL) and fully lamellar (FL) (See Figure 5). Each is composed of two phases, α_2 and γ in varying ratios. The duplex microstructure is composed of equiaxed γ grains mixed with fully lamellar grains roughly the same volume fraction. The near γ microstructure is mainly equiaxed γ grains with smaller α_2 grains at the grain boundaries or possibly no α_2 grains, in which case it would

be referred to simply an equiaxed γ structure. The nearly lamellar microstructure is very similar to the FL microstructure with the addition of smaller equiaxed γ grains around the grain boundaries. The FL microstructure is composed of lamellar grains with alternating α_2 and γ lamellae. The four microstructures can be formed by performing heat treatments at specific temperatures illustrated in Figure 6.

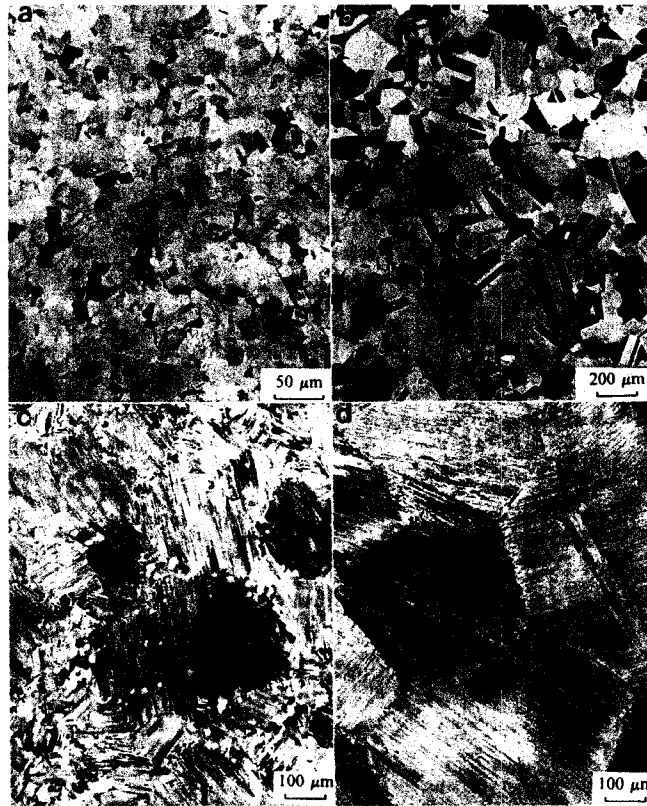


Figure 5 - a) Duplex; b) Near γ (NG); c) Nearly Lamellar (NL); d) Fully Lamellar (FL) [20]

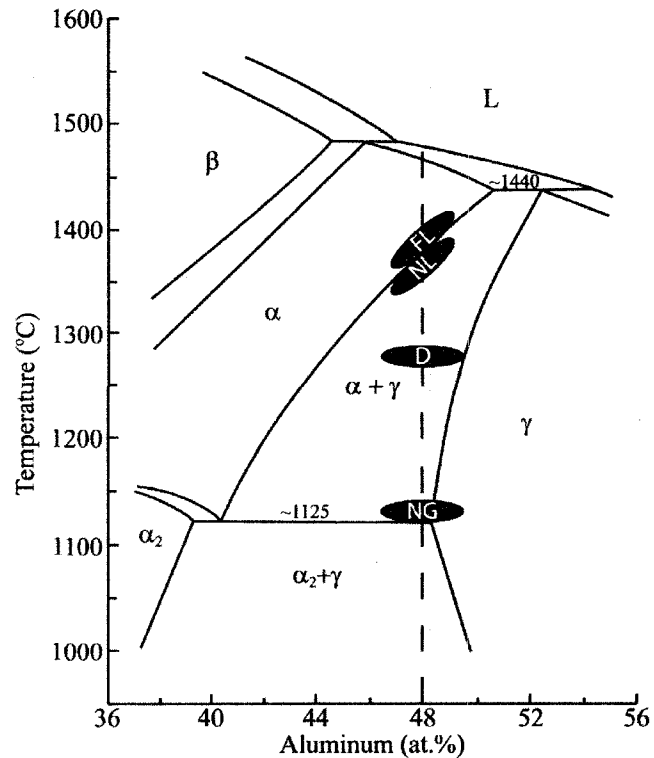


Figure 6 - Binary phase diagram from [2] with heat treatment temperatures used to develop particular microstructures marked; FL: Fully Lamellar, NL: Nearly Lamellar, D: Duplex, NG: Near Gamma

To form the FL microstructure, the alloy undergoes a heat treatment within the single phase α region, typically only 20 °C above the α transus to minimize unwanted grain growth. The nearly lamellar (NL) microstructure is formed by heating to 10 °C below the α -transus while the duplex microstructure is formed when heat treating within the two phase field ($\alpha+\gamma$). Near γ (NG) microstructures are formed by heating slightly above the eutectoid temperature (~1125 °C) [5].

2.1.1 Duplex

The duplex microstructure is composed of approximately 50% equiaxed γ grains and 50% FL grains (α_2 and γ lamellae). The advantages of the duplex microstructure are good room temperature ductility and strength while disadvantages include poor creep resistance and fracture toughness [5]. It is possible to have room temperature ductility up to 4% [21]. The relatively high ductility is due to the increased number of γ grains [22]. Equiaxed γ grains and γ lamellae show the highest dislocation density while the α_2 lamellae remain free of dislocations [23, 24]. The major deformation mode in duplex microstructures is slip of the $\langle 110 \rangle$ unit dislocations as well as very active twinning [25].

Of the disadvantages, the additional equiaxed γ grains are related to the poor creep resistance as seen in Figure 7. The plot demonstrates the effect of decreasing equiaxed γ content on creep resistance. As the amount of equiaxed γ is reduced, the creep resistance continually improves until a fully lamellar microstructure is achieved. It was suggested by Zhao et al. [26] that the γ grains can provide easy pathways for creep deformation.

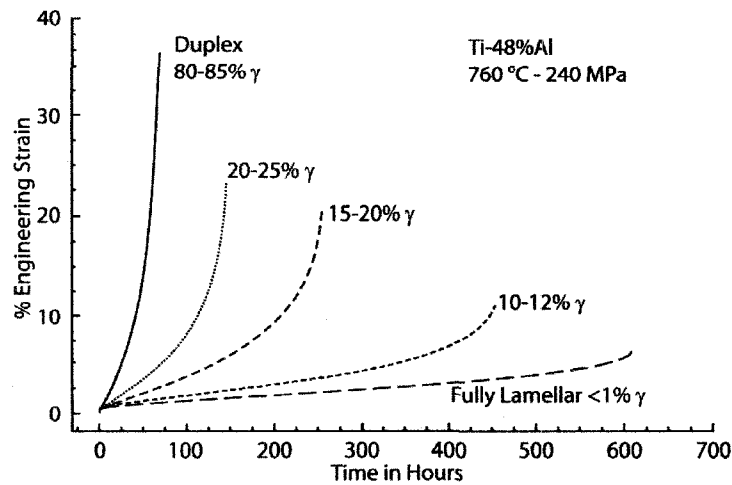


Figure 7 - Effect of decreasing equiaxed gamma content on creep [26]

Additionally, the poor fracture toughness compared to FL alloys is indicated by typical K_{IC} values ranging from ~ 11 to ~ 18 MPa \sqrt{m} depending on the fraction of γ to lamellar grains present [5]. Fracture toughness is also very dependent on temperature in duplex alloys compared to FL alloys showing an increase of K_{IC} up to ~ 20 MPa \sqrt{m} at 700 °C, as illustrated in Figure 8. In addition to the temperature dependence of the fracture toughness, the duplex microstructure shows lower brittle to ductile transition temperatures than the FL microstructure as shown in Figure 9

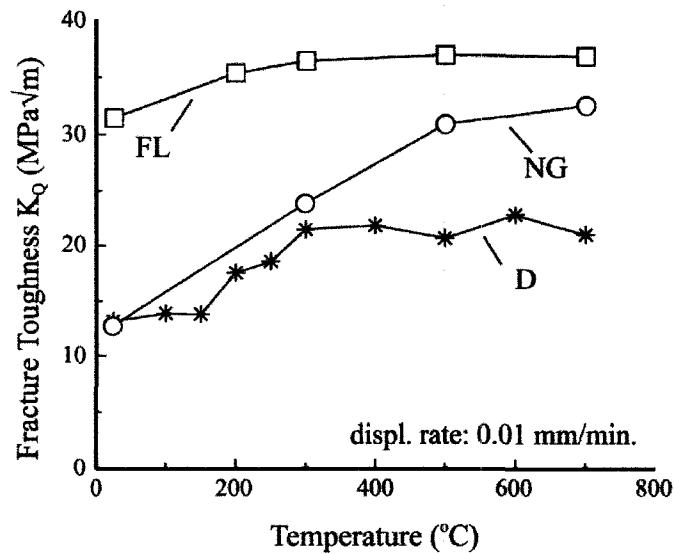


Figure 8 - Plot showing the temperature dependence of fracture toughness on temperature for the fully lamellar (FL), near gamma (NG) and duplex (D) microstructures [5]

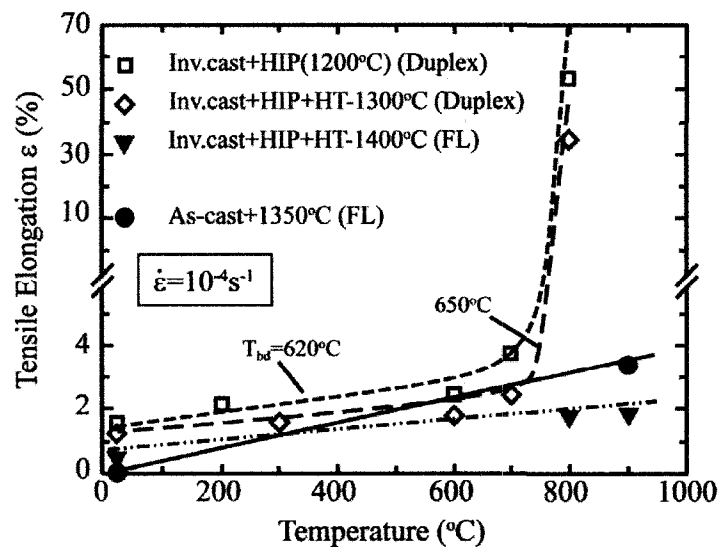


Figure 9 - Data showing how different microstructures retain their properties at high temperatures [5] (Duplex have the lowest brittle-to-ductile transition temperature (T_{bd}) while FL has the highest) (temperatures range from about ~ 620 °C up to ~ 800 °C)(as $\dot{\epsilon}$ increases, so does T_{bd} , indicating T_{bd} is controlled by thermally activated process)

2.1.2 Fully Lamellar

The FL microstructure's main advantage lies in its improved creep resistance and fracture toughness compared to the duplex microstructure [5]. The FL microstructure is composed of alternating α_2 and γ lamellae (illustrated in Figure 10) which form along the cooling path $\alpha \rightarrow \alpha + \gamma \rightarrow \alpha_2 + \gamma$ after heat treating within the single phase α region [3]. An alternative route is also possible in alloys with <45Al where ordering of the α phase occurs before formation of the lamellar structure, $\alpha \rightarrow \alpha_2 \rightarrow \alpha_2 + \gamma$ [27].

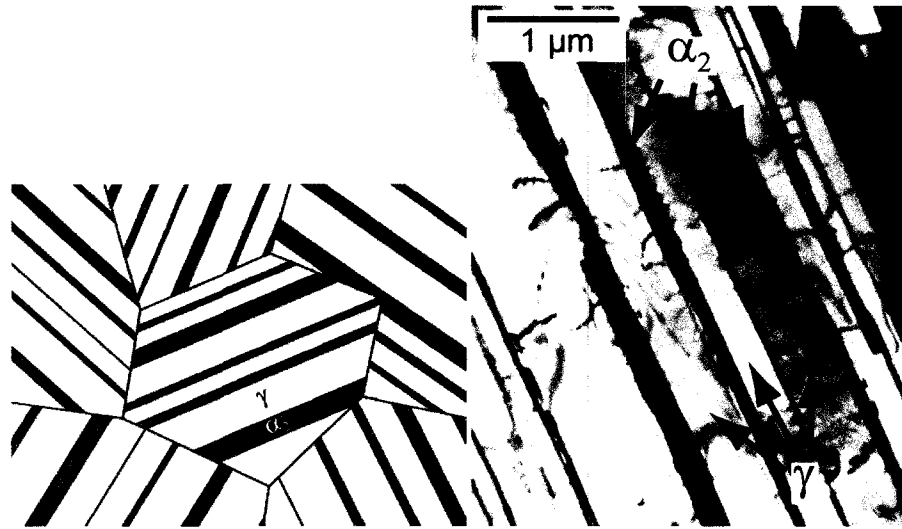


Figure 10 - Illustration and TEM micrograph of the FL microstructure with alternating γ and α_2 phases (TEM micrograph from [28])

The γ lamellae typically nucleate at stacking faults along α or α_2 grain boundaries upon cooling into the two phase region [29]. Long parallel plates form following the Blackburn orientation relationship $(111)_\gamma \parallel (0001)_{\alpha_2}$ and $\langle 11\bar{2}0 \rangle_{\alpha_2} \parallel \langle 1\bar{1}0 \rangle_\gamma$ [5, 30]. The number of γ nucleation sites is governed by the amount of undercooling available. Increasing the amount of undercooling and therefore the number of γ nucleation sites,

causes more γ to nucleate, which reduces the thickness of the γ lamellae [31]. Further cooling into the $\alpha_2 + \gamma$ region causes ordering of the α phase and a thickening of the γ lamellae [3]. In addition to the α_2/γ interfaces that form, there are also γ/γ interfaces. There are six different orientations about the [111] plane for these interfaces which fit into three categories, true twins (180°), pseudo twins ($\pm 60^\circ$) and order domain related ($\pm 120^\circ$) [32]. The γ lamellae form at random multiples of 60° relative to the next γ lamellae [33].

The creep resistance is very dependent on different microstructural features within the FL designation. The four governing features are lamellar thickness, grain size, grain boundary morphology and precipitates which will each be discussed in section 2.1.3.

Fracture toughness in FL microstructures is typically around $20 - 30 \text{ MPa} \sqrt{m}$ and does not show the same temperature dependence as the duplex microstructures which is shown in Figure 8 [5]. Although temperature does not have a large impact on the fracture toughness, the orientation of the FL grain to the crack does have a large impact. Since the FL grains are anisotropic, if the crack is propagating parallel to the lamellar interfaces, fracture toughness is relatively low. Likewise, if the crack is propagating perpendicular to the lamellar interfaces, fracture toughness is much higher [5].

2.1.3 Effects of Microstructure on Mechanical Properties

The mechanical properties of TiAl are very sensitive to any microstructural features present in the alloy from either thermo/mechanical processing or alloying. Large swings in the properties are possible by modifying the heat treatments to alter the microstructure

or through small additions of alloying elements. This section will discuss the impact of grain size and boundary morphology, lamellar spacing, precipitates and deleterious phases that may form.

2.1.3.1 Grain Size and Boundary Morphology

Grain size impacts many material properties including ductility, strength, fracture toughness and to a limited extent, creep resistance. Grain growth occurs when the material is heated to the single phase α region. Once dissolution of the γ phase is complete, the α grains begin to grow. To try and maintain balanced material properties, it is important to minimize the length of time heat treatments linger in the single phase α region in an effort to lessen grain growth. Alloying additions offer a measure of control over grain size; B has been shown to effectively inhibit grain growth [1, 5, 34, 35] and Fuchs also found that W reduces grain size in some conditions [36]. Beddoes et al. has examined the two alloys shown in Figure 11 and shown that they both follow the relationship in Equation 1 for diffusion controlled grain growth [37];

$$D = kt^n \qquad \text{Equation 1}$$

where D is the grain size, k and n are material constants and t is the heat treatment time. It has also been shown that cooling rates do not have a large effect on grain size [37].

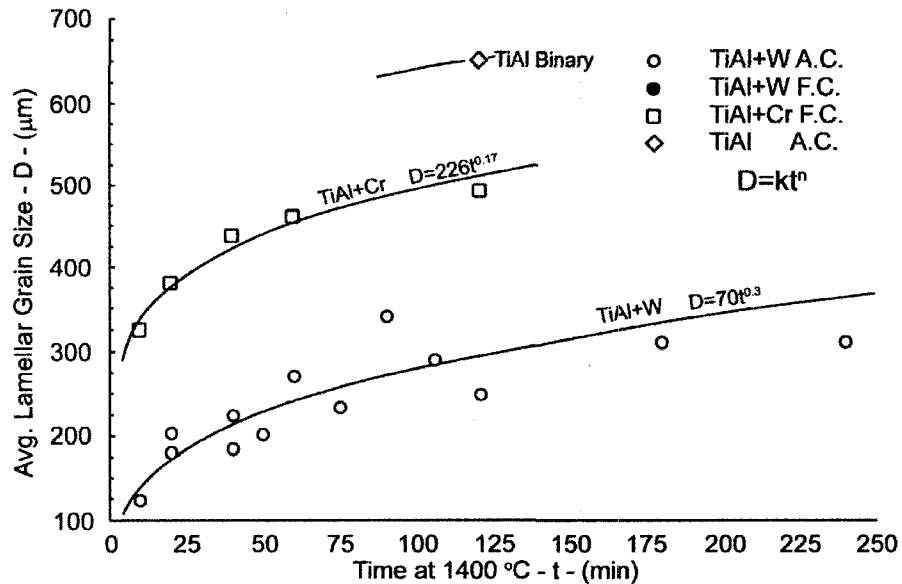


Figure 11 - Work from Beddoes et al. showing grain size growth compared to isothermal heat treatment time [37]

Since γ -TiAl is inherently brittle, researchers tend to minimize the grain size to improve ductility. Figure 12 shows the effects decreasing grain size can have on room temperature tensile properties. It is important to note that the ductility was roughly doubled by reducing the grain size from the range 700 - 1300 μm to 250 - 500 μm . Additional improvements to ductility are possible by producing microstructures with uniform grain sizes. Cast TiAl typically does not have as high of a ductility as other processing routes such as HIP'ing which offers fine uniform grain sizes and improved ductility [5].

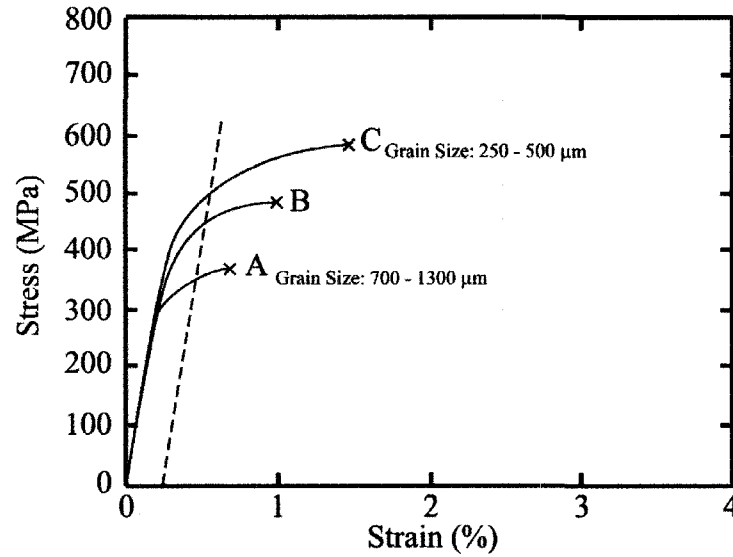


Figure 12 - Plot demonstrating the effects of decreasing grain size. Base material was Ti-47Al-1Cr-1V-2.5Nb (at.%) with a FL microstructure (Modified from [5])

A Hall-Petch type relationship exists between grain size and yield stress as found in Equation 2 [5];

$$\sigma_y = \sigma_o + k_y d^{-1/2} \quad \text{Equation 2}$$

where σ_o and k_y are materials constants, d is microstructural length parameter and σ_y is the yield stress. There exists, however, some controversy as to whether grain size, lamellar thickness or domain size, acts as the microstructural length parameter [5]. Work from Cao et al. [38] seems to show that both grain size and lamellar spacing have definite effects on yield strength in fully lamellar alloys with lamellar spacing having the most obvious impact. Figure 12 also shows the yield stress was improved from ~350 MPa to ~500 MPa by reducing the grain size from ~1200 μm to ~300 μm .

Additionally, reducing the grain size will cause the fracture toughness to decrease slightly [3].

Reduction in grain size also affects creep resistance but detrimental effects appear to be limited. Work from Kim and Hong has shown that varying grain size from 400 to 135 μm had almost no discernable effect on the minimum strain rate during creep [39] while it has been speculated that further reductions beyond 100 μm will be detrimental to creep resistance [3, 21]. Work from Au [21], shown in Figure 13, demonstrates the effects decreasing grain size has on the minimum creep strain rates.

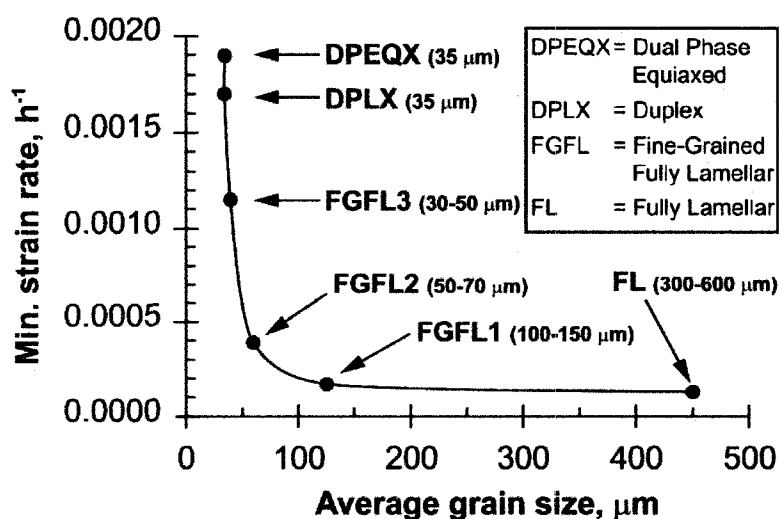


Figure 13 - Work from Au demonstrating the effects of decreasing grain size on minimum creep rates. (Tested at 760 °C and 240 MPa) [21]

There are two main types of grain boundary (GB) morphology, planar and interlocked. In addition, there is a third which is a combination of the two called mixed GB's [18]. Figure 14 illustrates the different types of GBs. GB morphology can affect creep since it governs the ease at which grains can slide against each other as well as the length of the crack path and how quickly it propagates [40]. By resisting cracking, the interlocked GB's increase the fracture ductility of crept samples by forcing more strain to occur in each of the grains [41]. This affects duration and onset of tertiary creep [41].



Figure 14 - Illustration of the two types of grain boundaries, interlocking (a) and planar (b), indicated by arrows [18].

The cooling rate from the α -transus governs which type of GB's form. Faster cooling rates such as water quenching or air cooling will generate planar GB's while slower cooling rates such as furnace cooling will form interlocked GB's. Intermediate cooling rates will produce the mixed GB's. The interlocked GB's exist due to coarser lamellae forming at the GB's [37]. Interlocked GB's appear to be the most beneficial for improved creep resistance in light of the above points.

2.1.3.2 Lamellar Spacing

Lamellar thickness plays an important role in the strength and creep resistance of lamellar TiAl alloys. As mentioned in section 2.1.3.1 there exists a Hall-Petch relationship (Equation 2) between lamellar spacing and yield strength showing improved yield strength with decreasing lamellar spacing [42-44]. According to work from Beddoes et

al., reducing the lamellar spacing will decrease the ability of dislocations to move down the γ lamellae through dislocation glide and climb [41, 45]. Other studies have also shown an inverse relationship between creep strength and lamellar spacing [25, 46]. The α_2/γ interfaces act as obstacles to dislocation motion [39, 47]. During dislocation climb, dislocations trapped at α_2/γ interfaces could reduce the motion of other dislocations causing bowing between the interfaces [20]. By reducing the lamellar thickness, both the fatigue strength [3] and creep strength [3, 26] are improved as well as yield strength and ductility [44]. Lamellar thickness is controlled by the cooling rate from temperatures above the α -transus [28]. As the cooling rate increases, the lamellae will become thinner. Care must be taken to avoid the formation of unwanted microstructures such as Widmanstätten or massively transformed γ (γ_m) (discussed in more detail in section 2.1.3.4) by controlling the cooling rate.

γ_m will decompose into an ultra-fine FL microstructure at higher temperatures according to work from Wang and Xie [43]. Wang and Xie have purposely caused the γ_m phase to form and then followed this with an aging heat treatment to convert the metastable γ_m to an ultra-fine FL microstructure through a number of rapid heating and cooling cycles. Although the end product (an ultra-fine FL microstructure) is developed, it is not advantageous to have any unstable features during creep testing since this can reduce creep resistance [48].

2.1.3.3 Precipitates

Precipitate size, location, number and distribution have a large impact on creep resistance and tensile strength [17, 18, 49]. In TiAl alloys that are precipitation hardened by the β phase, typically an initial solution heat treatment is performed to produce a homogeneous microstructure free of any precipitates. The solution heat treatment consists of heating into the single phase α region followed by a cooling rate rapid enough to avoid precipitation. Following this, an aging heat treatment is performed at a lower temperature which will cause the precipitates to form. In the Al-Cu binary system, the main driving force for precipitation is the reduction of energy in the system [50]. Due to the material being supersaturated from the rapid cooling following the solution heat treatment, the material will spontaneously decompose into more stable phases at the particular aging temperature [50]. The precipitates are able to increase hardness and strength by inhibiting dislocation motion but for the same reason, ductility is reduced. With a dispersion of precipitates, the dislocations are forced to either cut through the precipitates or bow between them [51]. It is, therefore, beneficial to have a fine dispersion of precipitates as compared to larger more dispersed precipitates.

In the case of Ti-48Al-2W, precipitates form at lamellar interfaces and grain boundaries by aging. Previous studies have examined the impact of interfacial precipitates on the creep resistance and tensile strength of a Ti-48Al-2W alloy [17, 18, 49]. A comparison was made between the alloy in the SHT condition (no precipitates) to the aged condition (precipitates at GB's and lamellar interfaces) and found that the

primary creep was dramatically improved while the total creep life was reduced. It was shown that precipitates at the lamellar interfaces reduce dislocation emission and mobility along lamellar interfaces which improved primary creep resistance. However, these precipitates also reduced the total creep life and rupture ductility. It was also shown that increasing aging time increased the amount of precipitation at the lamellar interfaces and grain boundary regions [18]. Lee had found that β particles at grain boundaries may promote micro-cracking [52] so the size of the precipitates at the grain boundary is an important factor in determining their effectiveness.

The precipitates can be formed by a number of beta stabilizing elements such as Cr, Nb, Mo, etc. but W was found to be the strongest with 1 at.% W \approx 6 at.% Cr [20, 53]. When these precipitates form at the lamellar interfaces during aging, they form with an orientation relationship of $\langle \bar{1}01 \rangle_{\gamma} // \langle 111 \rangle_{\beta}$, $\langle 111 \rangle_{\gamma} // \langle \bar{1}10 \rangle_{\beta}$ [54]. There are 6 different orientations on the (111) plane of the γ phase with 60° rotation between each [55]. The precipitates found in Ti-48Al-2W after an aging heat treatment were also shown to be the β phase with a BCC B2 crystal structure [18].

2.1.3.4 Deleterious Phases

Massive Transformation

A massive transformation has been defined as a “diffusional transformation producing a new metastable phase of the same composition as the parent phase, i.e., evolving without solute partitioning. It is observed at an increased cooling rate, as well as at an increased

undercooling” [56]. In the TiAl system, this happens when the material is rapidly cooled from the single phase α region. An early massive transformation in γ -TiAl was found by Wang et al. [57] in 1992. Wang verified that the γ_m transformation is indeed partitionless by performing a microprobe analysis across the $\alpha_2 - \gamma_m$ interface. Samples ranging in composition from Ti-46.5Al to Ti-49.5Al reveal a nearly identical composition between the two phases. The exact cooling rate or undercooling that must be supplied to cause the γ_m transformation varies greatly depending on the composition of the alloy. A massively transformed microstructure is shown in Figure 15.

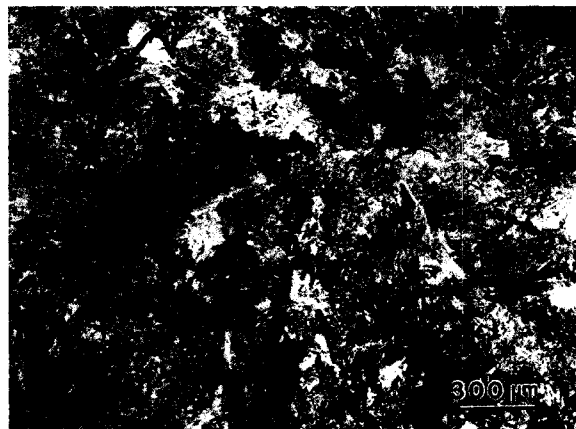


Figure 15 - Massively transformed γ [58].

Variations in the amounts of elements such as Nb, Al or α_2 stabilizers impact the γ_m formation. Alloying elements, such as Nb, which could decrease diffusivity through the TiAl system would lower the cooling rates required to form γ_m [58]. Any element which decreases the diffusion rates through the alloy would likely have a similar effect. Slowing the diffusion rate inhibits the long range diffusion required for the FL transformation to proceed. By restraining the FL transformation, it makes the γ_m transformation easier to

ensue. Similarly, increasing Al content will increase the likelihood γ_m will form during cooling. If the Al content is reduced to 45 at.%, studies have shown that no γ_m will form [59]. Additionally, stabilising the α_2 phase sooner may also increase the cooling rates required to form γ_m . By increasing the temperature at which the α phases order, the γ_m transformation can be inhibited [58].

Wang et al. [57] has suggested that some undercooling below the T_0 line (in the $\alpha + \gamma$ region) in Figure 16 is required to start the γ_m transformation. The T_0 line follows the middle of the $\alpha + \gamma$ phase and represents the location where the Gibbs free energy for each competing phase is equal. It was proposed that the available driving force was the distance between the T_0 line in the $\alpha + \gamma$ region and the T_0 line in the $\alpha_2 + \alpha$ region. This would mean that samples with Al content lower than roughly 45 at.% would not be capable of forming γ_m because there is no longer any driving force to cause the transformation.

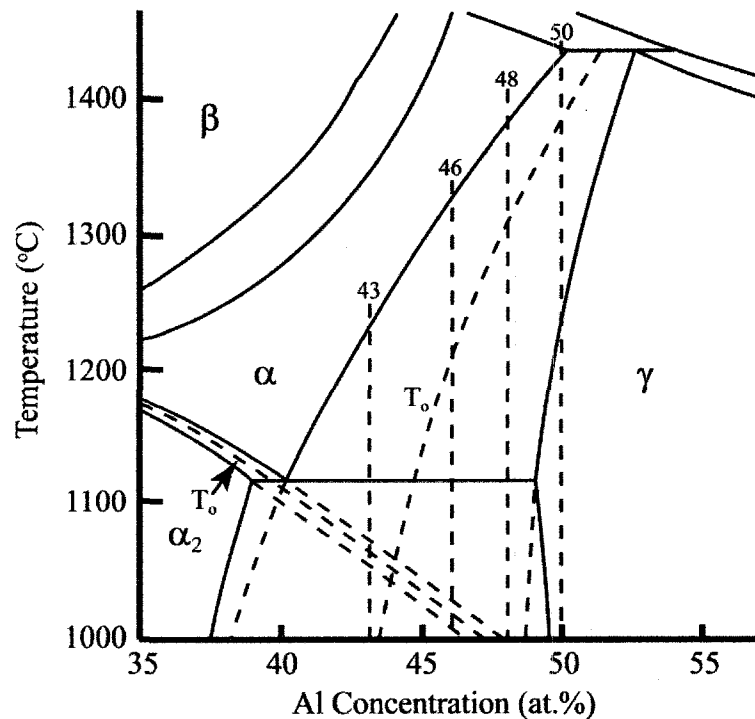


Figure 16 - Partial phase diagram for the binary Ti-Al system [57]

As well as the required cooling rate to initiate the γ_m transformation, composition also impacts the speed at which it proceeds. Alloying elements which alter the α grain size (such as Mn) while being heat treated in the single phase α region, can affect the rate of γ_m formation [58]. Since γ_m primarily nucleates at the prior α GB's, elements that restrict grain growth will provide more GB's for γ_m to nucleate at. With more nucleation sites the transformation, once initiated, can proceed more rapidly.

Equiaxed gamma

Equiaxed γ forms when solution heat treating in the two phase $\alpha + \gamma$ region followed by cooling slower than that used to form the duplex microstructure [20]. It can also form

during aging since the aging temperature generally approaches the eutectoid temperature. In the case of FL microstructures, equiaxed γ forms at grain boundaries during aging. It is considered as a detrimental phase since it has poor creep properties. Work from Kim and Hong [39] has shown that as the volume fraction of equiaxed γ is reduced, so does the minimum creep rate. This agrees with work from Beddoes as well, increasing the amount of equiaxed γ at GB's in a FL microstructure increases the minimum strain rate ($\dot{\epsilon}_{min}$) [20].

Feathery / Widmanstätten transformations

Cooling rates slower than those required to form γ_m will produce a feathery type microstructure, Figure 17 [32]. Herrouin et al. [60] has shown that the feathery microstructure can reduce creep rates. Herrouin has suggested that this may be occurring as a result of the lack of α_2 laths or by the imperfection of the lamellar morphology. However, the feathery microstructure does seem to improve the room temperature tensile strength [60].

Further reducing the cooling rate from the α phase region will produce the Widmanstätten microstructure, Figure 18, which forms within lamellar grains. Widmanstätten laths have some similarities with the α_2 and γ lamellae in the typical fully lamellar microstructure. Both Widmanstätten and the lamellar morphology have α_2 and γ platelets that share the Blackburn orientation relationship. Differences between the two microstructures include the α_2 phase morphology which is typically present but in much lower quantities and appears sparse and discontinuous within the Widmanstätten laths.

The α_2 phase is even sometimes seen within the γ lamellae of the Widmanstätten laths [32].

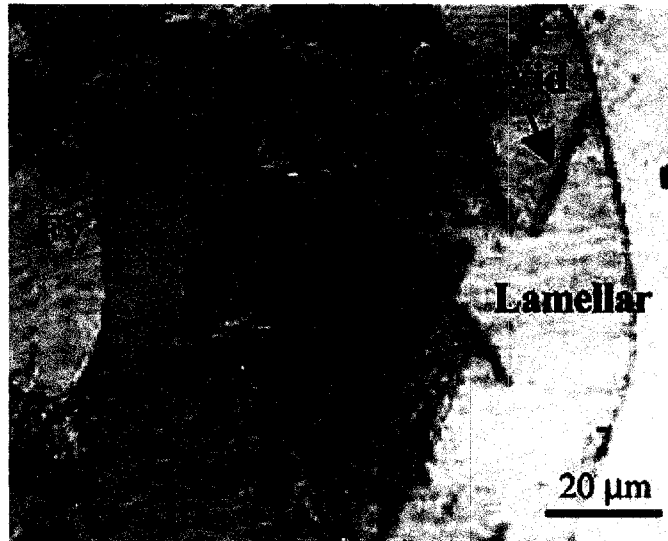


Figure 17 - OM showing the feathery microstructure (Fy) along with Widmanstätten laths (Wid) and typical lamellae (Lamellar) [32]



Figure 18 - Widmanstätten microstructure (Wid) formed within a fully lamellar colony [32]

To summarize, the highest cooling rates produce γ_m followed closely by feathery and then Widmanstätten laths at decreasing cooling rates. Reducing cooling rates further will produce a fully lamellar microstructure with thin lamellar spacing gradually increasing as the cooling rate is decreased further. At the slowest cooling rates, the lamellar morphology is completely lost and a near γ morphology becomes dominant.

2.1.4 Microstructural Control

Depending on the processing route taken to form the solid parts, samples, or ingots, different morphologies within the metal will exist. When parts are formed from a process where the metal has undergone a transition from liquid to solid, dendrites will exist. Cast microstructures are typically dendritic and exhibit large compositional variations from the dendrite core to interdendritic regions, Figure 19 [2, 61]. The dendrites form in the direction of heat extraction and cause both micro and macro-segregation. The segregation is caused as the material passes through the mushy zone, the elements with the highest melting temperatures solidify first forming the dendrites while the lower melting point elements are pushed to the interdendritic regions which solidify last. Further thermo-mechanical processing is required to minimize the texture and the dendrites form as well as to improve the homogeneity of the material. Unfortunately, it is very difficult to remove all of the texture, and usually some remains. HIP'ing is also required to close any porosity that may have formed during casting. To avoid these problems, pre-alloyed powder materials as part of a powder metallurgy processes can be used. The powder material is formed by gas atomizing an ingot of the target composition. Each powder

particle then contains a composition which closely reflects the nominal composition. The powders are then HIP'ed to produce a solid part with a homogeneous, uniform and fine grained microstructure.



Figure 19 – An optical microscope (OM) micrograph of a near stoichiometric cast alloy [2]

There are two main methods for controlling the microstructures developed in TiAl alloys, thermal processing and alloying. By varying the initial solution heat treatment temperature, any of the four main microstructures can be developed (near γ , duplex, nearly full lamellar, and fully lamellar) as discussed in section 2.1. Grain growth occurs when the material has been heated above or near the single phase α region. The exact temperature of the α -transus varies significantly depending on Al content and with the addition of alloying elements. Homogenization also occurs in the single phase α region so any heat treatments must be adjusted accordingly to balance grain growth with homogenization. According to Beddoes et al. complete dissolution of the γ phase in a

binary Ti-48Al alloy takes less than 10 min at 1400 °C, after which, grain growth proceeds rapidly and then slowing exponentially as the heat treatment proceeds [37]. Ideally, a completely homogeneous structure should be formed with a fine grain size. Alloying elements can be added to help restrict grain growth such as boron [1, 5, 34, 35]. Additionally, cyclic heat treatments can be used to reduce the grain size [21, 43, 62-65]. It was demonstrated that through multiple cycles consisting of rapid heating to the single phase α region, short hold times and subsequent rapid cooling, a fully lamellar grain size of 10 – 20 μm is achievable.

During the initial solution heat treatment, the cooling rate must also be controlled to develop the desired microstructure. Cooling rates affect the grain boundary morphology, lamellar thickness, ternary phases and the stability of the remaining α_2 phase. The cooling rate can also cause deleterious phases to form, so careful control over this aspect of the heat treatment must be maintained.

So the ideal cooling rate should be one in which the lamellar spacing is minimized and precipitation of any strengthening phases are avoided while developing interlocked grain boundaries and avoiding the formation of any deleterious phases.

2.2 Alloying

The mechanical properties of TiAl are very sensitive to any changes in the microstructure [66]. In addition to thermal processing, alloying is used to modify the properties of TiAl for specific purposes. This can be done for a number of different reasons some of which are to cause different phases to precipitate, to improve room temperature ductility, or to

improve high temperature mechanical properties. Table 1 describes the effect of different elements on TiAl in terms of microstructure, mechanical and environmental properties.

Table 1 - Effects of different alloying elements

Al	<ul style="list-style-type: none"> - Reducing Al will help suppress γ_m formation [59] - Increases mean lamellar thickness [67-69] - Reduces strength [69] but increases ductility and oxidation resistance [1, 70] - Reduces fracture toughness [21]
B	<ul style="list-style-type: none"> - Refines grains [1, 5, 34, 35] - Reduces chance of γ_m formation and helps stabilize the microstructure during high temperature operation [1]
Cr	<ul style="list-style-type: none"> - β stabilizer [37, 71] - Lowers the α-transus 13 °C for each at.% added [37] - Can improve oxidation resistance if more than 8 at.% is added [4, 70] - Enhances ductility [5, 37, 66, 70] up to a maximum of about 2 at.% [1] - Improves room temperature strength of the γ phase [5, 42]
Mn	<ul style="list-style-type: none"> - γ phase stabilizer which promotes the lamellar transformation during cooling as opposed to forming γ_m [58] - Can enhance ductility [5, 66, 70] up to about 2 at.% [1] - Improves strength of the γ phase at room temperature [5] - Reduces oxidation resistance [21]

Mo	<ul style="list-style-type: none"> - β stabilizer [66, 71] - Increases oxidation resistance [70, 72] - Can improve creep resistance [5, 70] up to about 2 at.% [1] - Improves ductility [5]
Nb	<ul style="list-style-type: none"> - β stabilizer [66, 71] - Improves oxidation resistance [4, 66] requires a minimum of 1 – 2at.% [1] - Improves strength significantly with 5 – 10 at.% additions [1, 66] - Improves strength of the γ phase at room temperature [5]
O	<ul style="list-style-type: none"> - Stabilizes the α_2 phase against the γ_m phase [58, 59] - Embrittles the γ phase [5]
Ta	<ul style="list-style-type: none"> - Improves oxidation resistance [70] - Increases chances for hot cracking and dendritic segregation [21]
V	<ul style="list-style-type: none"> - Generally reduces oxidation resistance [70] - Improves strength [21]
W	<ul style="list-style-type: none"> - β stabilizer [4, 37] much stronger than Cr [73] - Enhances creep resistance [5, 37, 74] - Improves oxidation resistance [37, 75] - Significantly increases tensile strength [37] - Lowers the α-transus 13 °C for each at.% added [37] - Reduces grain size [36]

2.2.1.1 Al Sensitivity

TiAl is very sensitive to Al among a number of other things. Small variations in Al content can have large effects on mechanical properties which is why it is so important to maintain control over Al content. By increasing or decreasing Al content, the volume fraction of α_2 will fluctuate (Figure 4), causing both the yield strength and the ductility to change. Figure 20 and 21 help illustrate how small changes in Al content can have much larger effects on the mechanical properties. Figure 20 and 21 were both created using identical material compositions for each Al point. The microstructures were varied which provides a large amount of scatter in the data for the same composition.

In addition to the room temperature properties, increasing Al content in a single phase γ alloy was found to increase in the minimum strain rate during creep testing [20]. Increasing Al content is also beneficial for improved oxidation resistance [75].

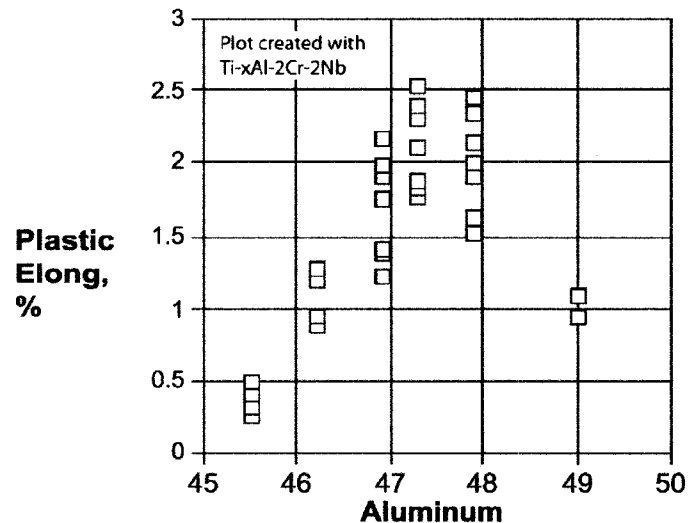


Figure 20 - Effect of varying Al content on plastic elongation with various heat treatments [76]

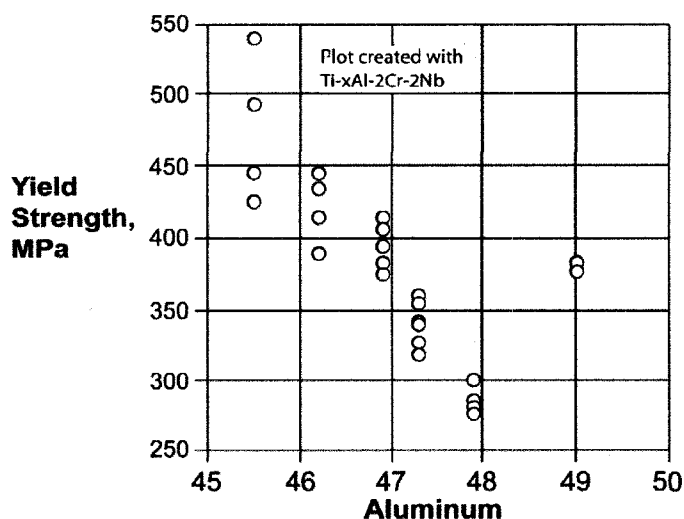


Figure 21 - Effect of varying Al content on yield strength with various heat treatments [76]

2.2.1.2 Cr and Nb Additions

Cr and Nb are added to the binary 48Al alloy to improve ductility and oxidation resistance, respectively. Huang has suggested that the improvements to ductility from Cr additions are due to a weakening of the Ti-Al covalent bond which promotes the formation of the γ phase containing thermal twins [23]. The maximum benefit for ductility is realised with a 2% Cr addition [1]. Cr has also been shown to reduce grain growth kinetics [37] which can also improve ductility. Cr has been reported to lower the α transus 13 °C for each atomic percent added in one study [37] and almost 20 °C per atomic percent from another [23].

2 at.% Nb additions to a Ti-48Al-2Cr alloy show large improvements to both isothermal and cyclic oxidation resistance [77]. Ti-48Al-2Cr-2Nb is oxidation resistant up to 850 °C showing 3 mg/cm² weight gain after 500 hrs of rapid cycling as shown in Figure 22 [70, 75]. Thin banded oxide scales form with a titania rich outer layer and a

dense alumina rich inner layer [75]. Oxidation improvements from Cr additions are possible but not before more than 8% Cr is added [75]. Less than 8% as seen in Figure 22 will reduce oxidation resistance. The improvement with 8% Cr additions is due to the formation of very thin protective alumina scales.

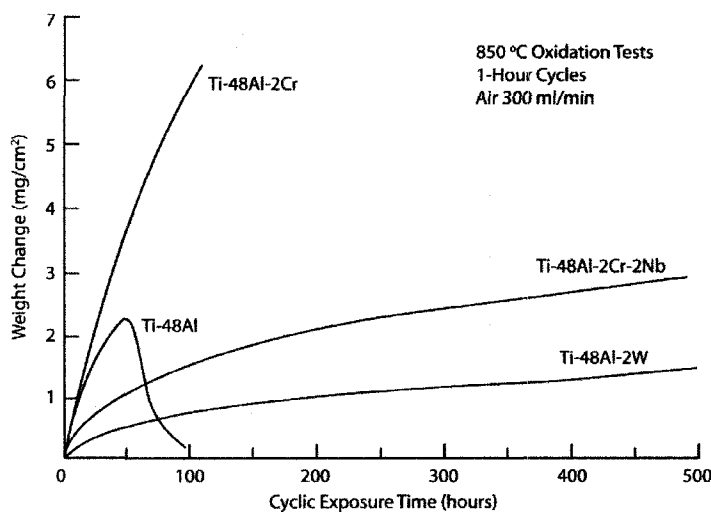


Figure 22 - Results from a cyclic oxidation test at 850 °C with 1 hr cycles in air [70, 75]

2.2.1.3 W Additions

W is usually added to alloys for improvements to strength and creep resistance [74]. Compared to Mo, Nb and Cr, W causes the greatest improvement to creep resistance [20]. W seems to be an effective solid solution strengthener as well [78, 79], however, a greater impact to creep resistance can be achieved by causing W to form precipitates as discussed in section 2.1.3.3. Hodge et al. [79] argues this statement and claims that W is more beneficial if precipitation of the β phase is avoided. It seems that of the alloys Hodge investigated, precipitates were not formed at lamellar interfaces which could be the cause of the poor creep results he found.

Other benefits related to W additions include reduced grain growth during heat treatments [36, 37, 75], stabilization of the α_2 phase during aging against γ growth and coarsening [80], and improved oxidation resistance as seen in Figure 22 [75]. The slow grain growth kinetics have been suggested to be a result of the slow diffusing W [81] suppressing diffusional migration of grain boundaries [37]. Stabilization of the α_2 phase has been described by Larson et al. [80] who suggested that W slows the coarsening mechanisms of the γ phase. γ coarsens through the motion of ledges that move parallel to the α_2/γ interface and W segregates at these ledges as it is being rejected from the γ lamellae. Larson has postulated that since W diffuses very slowly, it could impede the motion of these ledges.

As a final note on W, it has been shown that it lowers the α transus 13 °C for each atomic percent added to a binary 48Al alloy [37]. In the B2 phase, W substitutes for Al but in the $L1_0$ phase, W substitutes for Ti [82].

2.3 Deformation Modes

Deformation occurs primarily in the γ phase when dealing with the two phase γ -TiAl alloys and the deformation generally occurs only on the close packed planes through both normal and super dislocations as well as twinning [33]. Since the γ phase is FCT, not all the γ orientations are equivalent so depending on the orientation of the grain to the load axis, deformation could be accommodated through either dislocations or twinning [20]. At both high and low temperatures, in the FL microstructure, dislocations are generated from the lamellar interfaces.

2.3.1 Creep

Creep typically occurs in metals at temperatures above $0.4 - 0.5 T_m$ [83]. It is characterised by increasing strain with time, under a constant stress and temperature. There are three main stages that occur during creep denoted as primary, secondary and tertiary creep. Preceding primary creep is an instantaneous strain that is generated as the load is applied. Primary creep follows this as the strain rate slowly decreases as the material strain hardens. Once the rate of strain hardening is equal to the rate of recovery, the strain rate remains steady until the tertiary creep stage [50]. Tertiary creep consists of an increasing creep rate caused by cavitation and crack growth [83]. Finally, fracture occurs once the small cracks link together and form a crack larger than the critical crack length. It is important to highlight that not all materials undergo a well defined secondary creep phase. For example, in the case of TiAl, primary creep tends to lead directly to tertiary creep. Therefore, the minimum creep strain rate, or the inflection point, of the creep curve is assumed to be close to the steady state creep rate [83]. An outline of basic creep theories will be discussed, followed by a discussion on creep in TiAl alloys.

2.3.1.1 Power Law Relationship

The power law equation (Equation 3) is used to describe the steady-state creep rate [84];

$$\dot{\epsilon}_s = A\sigma^n \exp\left(-\frac{Q_c}{RT}\right) \quad \text{Equation 3}$$

where A is dependent on the microstructure, σ is the applied stress, n is the stress exponent, Q_c is the activation energy, R is the universal gas constant and T is the absolute

temperature. Depending on the stress and temperature regimes, values for Q_c and n can vary. Typically at low and moderate stresses, the steady state creep rate is related to the applied stress in a linear fashion. At very high stresses, this relationship can break down and the steady state creep rate is then related to the stress in an exponential manner. This is known as the power law breakdown regime. Changes in either n or Q_c occur in different stress and temperature regimes which signifies a change in the creep mechanism [84], which are discussed in the following sections.

2.3.1.2 Diffusional Creep

For diffusional creep to occur there must be sufficient energy to allow one atom to jump into an adjacent lattice site in addition to that lattice site being vacant. Increasing temperature increases the density of vacancies and also provides energy to the atoms to allow them to jump into adjacent, empty, lattice sites [84]. Diffusional creep, therefore, requires high temperatures and can take place at low stresses [56]. An expression is used to determine the diffusion coefficient of a metal given in Equation 4;

$$D = D_0 \exp - \left(\frac{Q}{RT} \right) \quad \text{Equation 4}$$

where D_0 is a constant and Q is the activation energy for diffusion which is comprised of the energy needed to move an atom as well as the energy required to form a vacancy. For self diffusion to occur, the activation energy, Q_{SD} must be overcome. During creep at high temperatures, Q_c is approximately equal to Q_{SD} . At lower temperatures, $0.4 - 0.6 T_m$, Q_c can be significantly less than Q_{SD} . This can be possible because dislocations and grain

boundaries offer easy diffusion paths [84]. Atoms within the crystal lattice have more bonds than those at surfaces and therefore require more energy to shift positions. Diffusional creep processes are broken down into two mechanisms, Nabarro-Herring and Coble creep.

Nabarro-Herring Creep

Nabarro-Herring Creep is a form of diffusional creep in which vacancies are generated at grain boundaries in tension and migrate to grain boundaries in compression through the body of the grain [56, 84]. This action is termed stress directed vacancy flow. The grain boundaries act as perfect vacancy sources and sinks and over time, cause a change in the dimensions of the grain. In addition to this, $\dot{\epsilon}_s$ is linearly related to the applied stress, so $n \approx 1$. Typically, tests carried out at high temperature and low stress produce values of $n \approx 1$ and $Q_c \approx Q_{SD}$.

Coble Creep

Coble creep is similar to Nabarro-Herring creep in that it deals with diffusion of vacancies through the crystal lattice from areas of tension to areas in compression. It is, however, also possible for vacancies to diffuse along the easier grain boundary path. Coble creep incorporates this by introducing a new activation energy termed Q_{GB} for the energy required for grain boundary diffusion. When the power law creep equation is used and a stress exponent of roughly 1 is found and $Q_C < Q_{SD}$ (because $Q_C \approx Q_{GB}$), then Coble creep is likely the dominant creep process [84].

2.3.1.3 Dislocation Creep

For dislocation creep theories, $Q_c \approx Q_{SD}$ at high temperatures while at low temperatures, $Q_c \approx \frac{1}{2}Q_{SD}$. The stress exponent, n , is approximately 4 and above [84]. According to Evans and Wilshire, grain size does not have a large impact on $\dot{\epsilon}_s$ when creep occurs through diffusion-controlled generation and motion of dislocations [84]. Dislocation creep theories are based on the fact that the rate of work hardening is balanced by the rate of recovery as described below [84].

Work hardening is defined as an “Increase in the true stress with increasing true strain and strain rate” [56]. Recovery during hot deformation (creep deformation) includes “the disappearance of deformation-induced point defects and annihilation and rearrangement of dislocations (both by glide and climb), as well as subgrain formation and growth” [56]. Dislocation glide occurs as a dislocation moves down a favourable slip plane under the influence of a local shear stress. Once the dislocation runs into an obstacle, it stops and more dislocations emitted from the same dislocation source begin to pile up at the obstacle. The first dislocation will eventually climb into different slip planes as additional dislocations pile up at the obstacle. When this climbing dislocation moves into adjacent planes it can either be annihilated by another dislocation of the opposite sense, or after climbing through enough slip planes, it may be free of the obstruction and continue to glide. The glide and climb process are seen as recovery processes since they allow additional dislocations to be emitted from the source and the pile up at the obstacle is seen as a hardening mechanism since higher shear stresses are required to emit further

dislocations. These mechanisms occur simultaneously during creep testing at high temperatures and the relative rates of each mechanism cause the variation in $\dot{\epsilon}$ [84].

The different creep modes discussed above can be summarized graphically as shown in Figure 23 [84]. The plot is generated from pure metals once they have achieved a steady state $\dot{\epsilon}$ and shows what creep modes are dominant at different stresses and temperatures. The stresses and temperatures are both normalized.

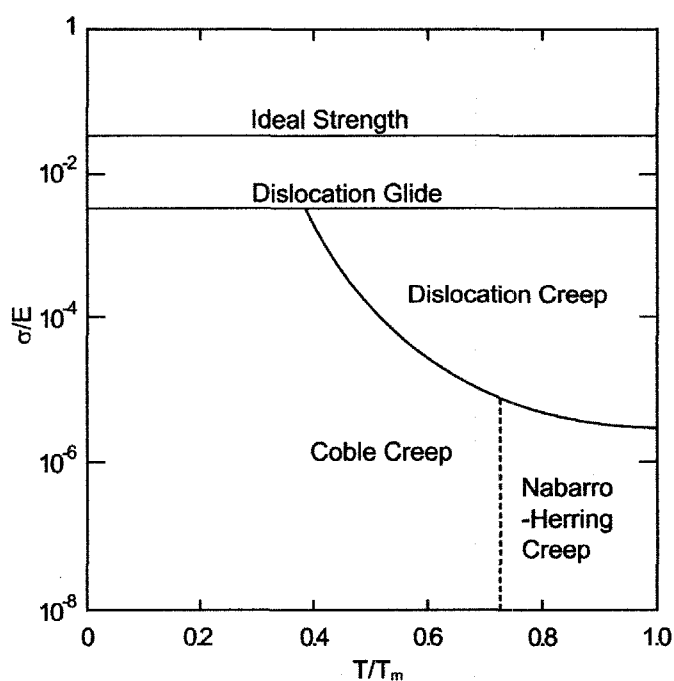


Figure 23 - Creep deformation map [84]

2.3.1.4 Creep in TiAl

The rate controlling mechanisms for TiAl seems to be controversial. Specific mechanisms are not easily determined because when an analysis is performed using Power Law Creep equation (Equation 3), the stress exponent values are seen to steadily increase from roughly 1 up to 10 and even up to 20 in some extreme cases [83].

Additionally, there is no definite steady state strain rate as well as a very strong dependence of creep properties on the microstructural features, particularly, lamellar thickness [83]. Work from Beddoes et al. [41] shows that the stress exponent increases with the applied stress, ranging from 1 at low stresses to 10 at high stresses. The cause for the fluctuating n value is due to a change in the rate controlling mechanism [20, 84]. It has been postulated that at lower stresses with $n \approx 1$, diffusional controlled creep is dominant and as stresses increase and n approaches 10, dislocation climb or dislocation glide processes become the rate controlling mechanism [20, 26, 41]. Zhao et al. [26] has suggested that the reason for the high strain rates at high stresses is due to dislocation glide being the rate controlling mechanism. Other work also supports the theory that creep is limited by dislocation climb [39, 47]. Beddoes also speculated that thinner lamellar spacing improves creep properties by increasing the internal stress required to initiate glide controlled creep [41].

During primary creep, the high creep rate is thought to be due to dislocation emission from lamellar interfaces [1, 20]. Coherency strains are believed to be the cause of the dislocation emissions [45]. Decreasing lamellar spacing does, however, improve primary creep. The improvement is believed to be a result of higher internal stresses required to cause dislocation glide [41]. Beddoes has suggested the difference in time to 0.4% strain between two similar microstructures with different lamellar spacing is due to alterations of dislocation motion within the lamellae or differing dislocation generation rates [41].

Once the primary creep stage has completed, TiAl alloys usually transition quickly into the tertiary creep regime. In this stage, creep rates accelerate until failure occurs. Beddoes has stated this is usually associated with the formation and coalescence of voids and cracks or microstructural instabilities [20]. In addition, he has also suggested that the lamellar grain size can have large effect on the amount of tertiary creep experienced by a sample.”

An example creep curve is displayed in Figure 24 which also illustrates the benefits of W additions. W forms precipitates at the lamellar interfaces and grain boundaries after aging as discussed previously. The reduced primary creep seen in Figure 24 was attributed to the precipitates which formed at the lamellar interfaces. The reduced creep life and rupture ductility was attributed to the precipitates at the grain boundaries.

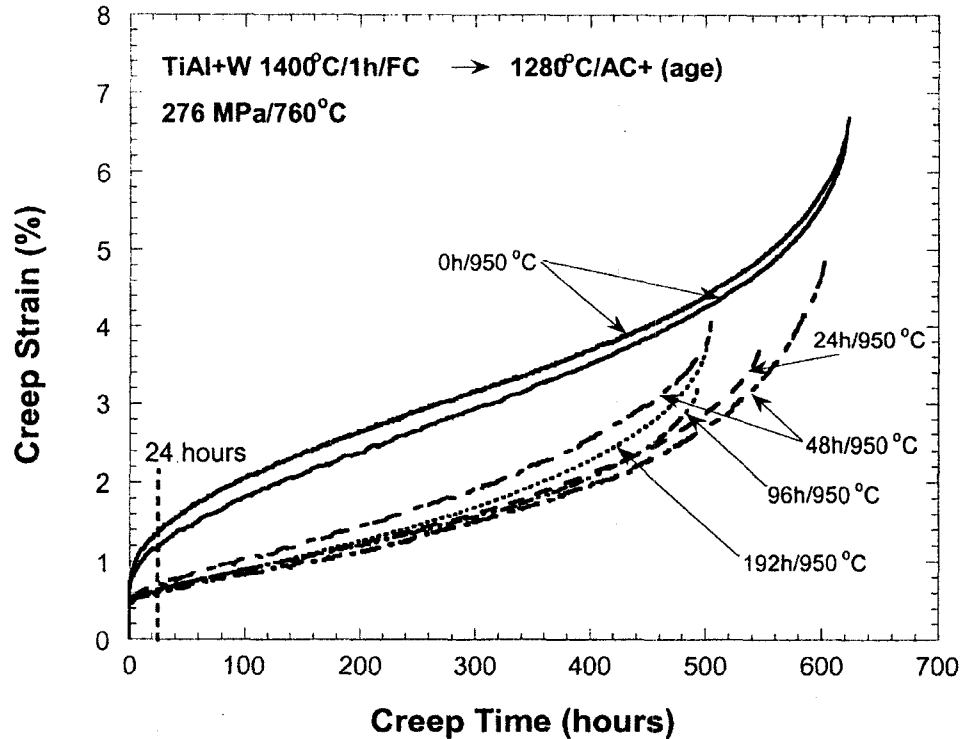


Figure 24 - Creep curves of a Ti-48Al-2W alloy in the unaged (0hrs) condition as well as multiple aging times (24, 48, 96 and 192 hrs) [18]

2.3.2 Tensile

Tensile deformation at room temperature is made difficult by the crystal structure of each phase. Easy dislocation motion is not possible due to the ordered structures of the two phases. The HCP unit cell is limited to slip on the close packed or basal planes. Slip within the HCP unit cell occurs through the following two burgers vectors, $1/6\langle 1210 \rangle$ and $1/6\langle 1216 \rangle$ [85].

Slip within the FCT unit cell at lower temperatures occurs primarily along the following three close packed burgers vectors arranged by increasing energy; $1/2 [110]$, $[101]$ and $1/2 [112]$ [2]. The latter two dislocations are superdislocations which require

additional energy. This is caused from the ordering along the (002) planes normal to the c axis. At higher temperatures, slip systems along non-close packed planes could become active such as $\langle 100 \rangle \{110\}$ [2].

2.4 Summary

Duplex microstructures offer improved room temperature ductility and strength but poor fracture toughness and creep resistance. Their limited creep resistance is due to the presence of equiaxed γ grains intermixed with the FL grains. The γ grains offer easy dislocation motion during creep but at the same time, they offer increased room temperature ductility over the FL grains.

If all the γ grains are removed from the duplex microstructure, a FL microstructure is produced with improved high temperature properties and fracture toughness. The ductility is reduced; however, some ductility can be regained by reducing the grain size to roughly 100 μm with only a minimal effect to creep resistance. Also, since creep occurs primarily through dislocation glide and climb within the γ lamellae, a thin average lamellar spacing with precipitates located at lamellar interfaces produces a microstructure with improved creep properties. In addition, interlocking GB's extend the tertiary creep phase, improving creep life, by promoting increased deformation within the individual grains as opposed to inter-granular cracking.

Chapter 3: Thesis Objectives and Scope

The objectives of this thesis is to examine the effects of W additions to the powder metallurgy Ti-48Al-2Cr-2Nb (at.%) alloy (base alloy) with respect to the microstructure and mechanical properties. The objectives are as follows;

- 1) Determine the effect of W on the base alloy
- 2) Develop ideal solution and aging treatments to stabilize the microstructure and form precipitates at lamellar interfaces.
- 3) Improve creep and tensile properties of the base alloy through W additions and heat treatments

It is expected that the W additions have the potential to improve the creep properties and microstructure of the base alloy by forming precipitates at the lamellar interfaces in the fully lamellar microstructure. In addition, the precipitates could stabilize the microstructure during aging and minimize microstructural degradation during creep. To examine this theory, three different powder materials were used to test the effectiveness of the W additions; the base alloy Ti-48Al-2Cr-2Nb (0%W) as well as two W containing alloys Ti-48Al-2Cr-2Nb-0.5W (0.5%W) and Ti-48Al-2Cr-2Nb-1W (1%W). The following tasks were identified;

- 1) Consolidate pre-alloyed powders by hot isostatic pressing (HIP'ing)

- 2) Develop an optimum solution heat treatment to produce a fully lamellar microstructure without detrimental phases.
- 3) Examine different aging conditions
- 4) Perform creep and tensile tests on select samples based on the results from micro-hardness testing and microstructural characterization.

The following chapter describes in detail the experimental methods employed to complete this study. Chapter 5 presents the results and elucidates the effect of W on the microstructure and mechanical properties. A brief summary with conclusions and a few interesting ideas for future work follow in Chapter 6.

Chapter 4: Experimental Details

To elucidate the effects of W on the microstructure and mechanical properties of powder metallurgy (PM) Ti-48Al-2Cr-2Nb, W was added to create two different alloys, Ti-48Al-2Cr-2Nb-0.5W and Ti-48Al-2Cr-2Nb-1W. The three alloys were supplied as pre-alloyed powders from Crucible Research Corp. and were hot isostatically pressed (HIP'ed) to produce >99.9% consolidated bars [86]. This was followed by an optimized thermal processing route which included two heat treatments to develop useful microstructure and mechanical properties. The initial heat treatment employed is termed a step cooled heat treatment (SCHT) and was used to homogenize the microstructure and develop a fully lamellar microstructure. Following the SCHAT, aging was performed to form precipitates as well as to stabilize the microstructure. Different aging times were examined and the effects on creep and tensile properties were determined through mechanical testing. The following sections detail the procedures of the experiments.

4.1 Sample Production

4.1.1 Powder Materials

The alloys examined had nominal compositions of Ti-48Al-2Cr-2Nb, Ti-48Al-2Cr-2Nb-0.5W and Ti-48Al-2Cr-2Nb-1W (at.%) referred to as 0%W, 0.5%W and 1%W, respectively. Each alloy was pre-alloyed and gas atomized to a -35 US STD mesh size at Crucible Research Corporation. The powders were stored under an argon hood to minimize contamination, mainly oxidation. Compositions of the powder materials for this study are shown in Table 2.

Table 2 - Compositional analysis provided by Crucible Research on the powders used for this study

W Content	Atomic %								
	Ti	Al	Cr	Nb	W	Fe	C	O	N
0.0%	47.96	47.74	1.97	2.03	--	0.0625	0.0582	0.1601	0.0194
0.5%	48.10	47.54	1.86	1.82	0.45	0.0282	0.0262	0.1698	0.0056
1.0%	47.20	47.80	1.98	1.87	0.91	0.0286	0.0299	0.1724	0.0114

4.1.2 HIP Processes

A Hot Isostatic Press (HIP) was used to consolidate the powder material. To allow for HIP'ing, the powder material was first vacuum encapsulated in either 304 or 316 low carbon stainless steel tubing with a wall thickness of 0.049" or 0.035" and an outer diameter of 5/8". The tubes were cut to roughly 18" in length, crimped and tungsten inert gas (TIG) welded at one end, then filled with approximately 7" of powder. Filling the tubes with powder took place while inside a glove box filled with an argon atmosphere to reduce any oxidation that may occur. The glove box can be seen in Figure 25 and a tube

filled with powder in Figure 26. Once the tubes were filled, a latex cover was placed over the open end of the tube and held in place with an elastic. The cover was used to minimize any oxygen contamination during transport from the glove box to the vacuum. The transfer between the two took place as quickly as possible and was typically less than 5 min.

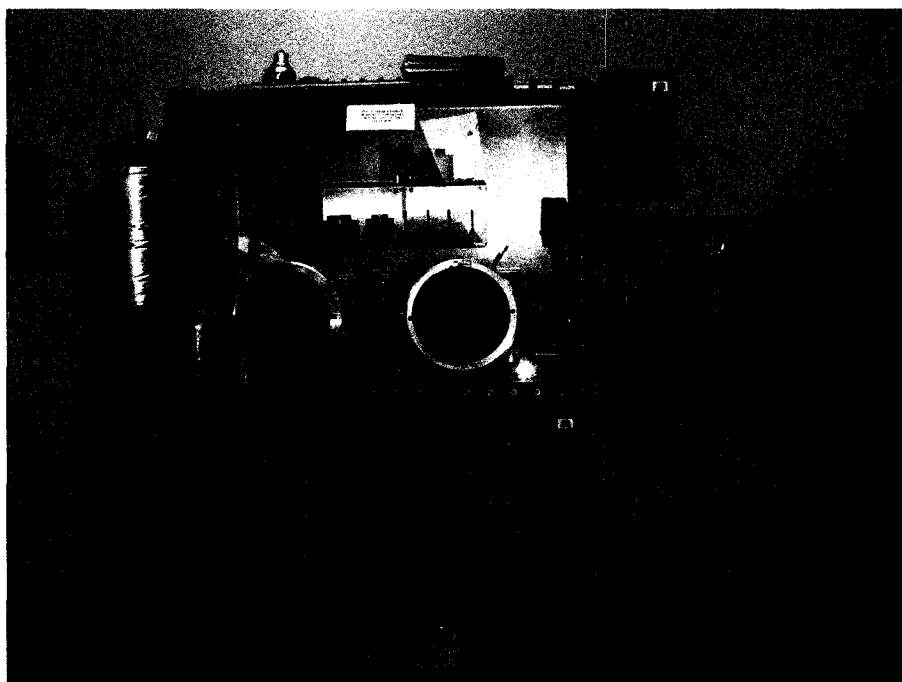


Figure 25 - Glove box with an argon atmosphere where the powder metal was stored



Figure 26 - Stainless steel tube sealed at one end, filled with TiAl powder and closed at the other end with a section of rubber glove to minimize oxygen contamination during transport from the glove box to the vacuum

Before connecting to the vacuum, the latex cover was removed and a small ball of fibreglass was inserted in the end to minimize any powder loss during the vacuum process. The tubes were left under vacuum for a minimum of 4 days at 350 °C and a maximum pressure of 2.5×10^{-5} torr to minimize oxygen contamination as shown in Figure 27. The tubes were then sealed by crimping and TIG welding the remaining end. The tubes were left on the vacuum during the crimping process and once completely crimped, disconnected from the vacuum before cutting and TIG welding. Figure 28 shows the sealed tubes prior to HIP'ing.

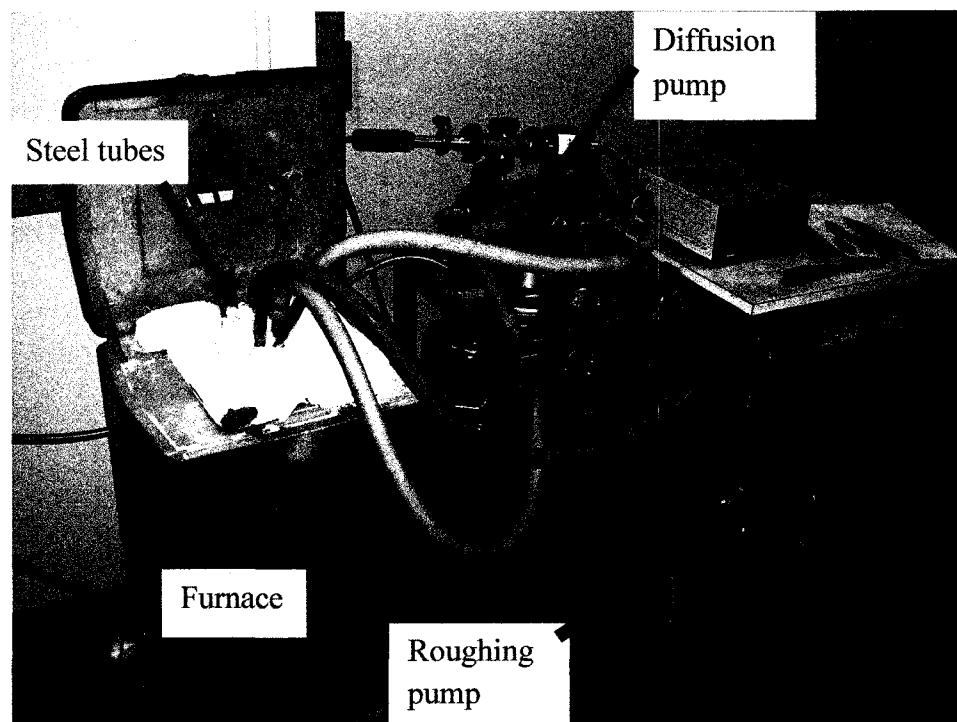


Figure 27 - Steel tubes connected to the vacuum being degassed at 350 °C

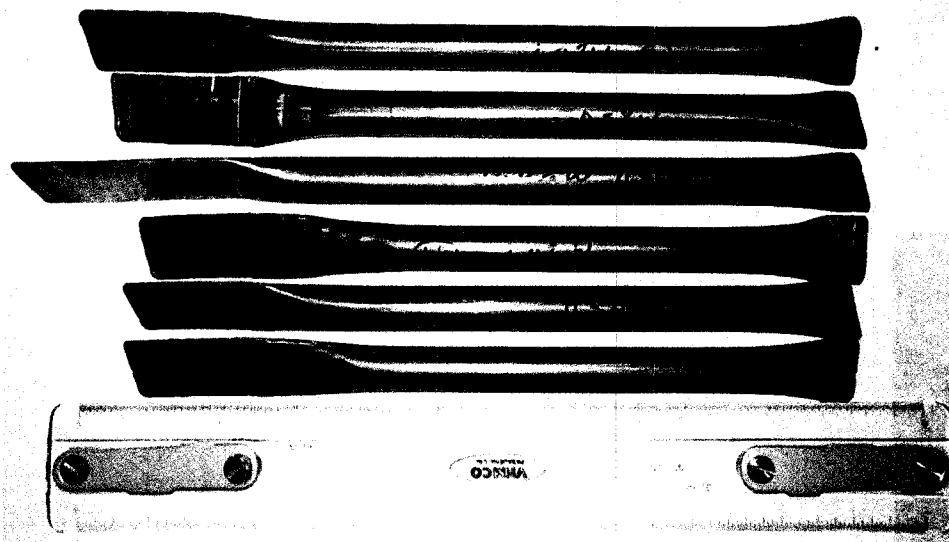


Figure 28 - Stainless steel tubes with TiAl powder sealed inside under a vacuum prior to HIP'ing

The powders were consolidated by HIP'ing at 1200 °C, 200 MPa in an Ar atmosphere for 2 hrs. Once HIP'ing was completed, an abrasive saw was used to remove the crimped ends and section the tubes into two lengths, each approximately 3" long. The 3" bars were then decanned at Carleton University's machine shop using a lathe. To decan the bars, one end was placed in a collet and mounted in the spindle. The free end of the bar had a small hole drilled in it using a 3/16" tungsten carbide centre drill while at a speed ~2500 rpm. A live center was then used to support the free end of the bar during the decanning process. A tungsten carbide tipped tool was used to remove material at a rate of 0.010 – 0.015" per pass at a speed of 500 – 600 rpm. A tool feed rate setting of 20 – 25 was used. Figure 29 shows a tube which has had the ends removed and has been cut into two lengths with one half de-canned.

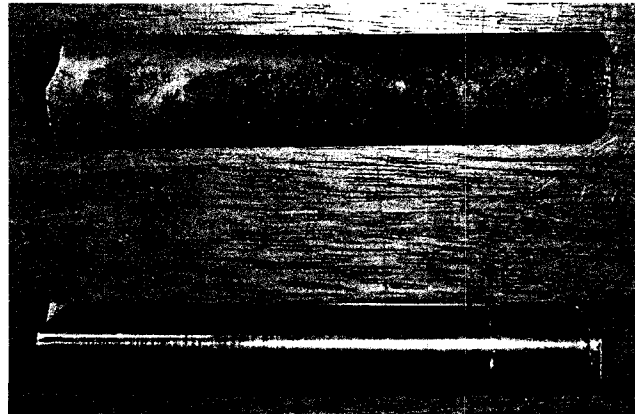


Figure 29 - TiAl after HIP'ing, the sample on top is still clad in the stainless steel tube while the sample on the bottom has been de-canned

4.1.3 Heat Treatments

The heat treatments were broken up into two different categories. Initially a step cooled heat treatment (SCHT) was applied to homogenize the HIP'ed samples and produce the fully lamellar microstructure while avoiding any massively transformed γ . Following the SCHT, an aging heat treatment was applied to stabilize the microstructure and produce precipitates.

4.1.3.1 Step Cooled Heat Treatment (SCHT)

Two separate investigations were undertaken to develop an optimum SCHT. Initially the ideal transition temperature ($T_{F/A}$) was examined. For this study, small 1.5 – 2 cm pieces cut from the 3" bars shown in Figure 29 were not encased in quartz tubes. Initial solution heat treatments were carried out using a Lindburg/Blue M box furnace (model #: BF51333C). The heat treatment path was determined from DSC (differential scanning calorimetry) data generated by J. Overton [87]. Samples were heated in air to 1400 °C

(above the α -transus), then held for 20 min and then furnace cooled to a transition temperature ($T_{F/A}$) followed by air cooling to room temperature. The two step cooling sequence illustrated in Figure 30 has been termed stepped cooling. If the samples are air cooled to room temperature directly from the holding temperature, massively transformed gamma (γ_m), which has poor creep resistance and is not stable at higher temperatures, is expected to form. However, if a slower cooling rate, such as furnace cooling is used, then the β phase is likely to form and the lamellar structure is likely to coarsen. Lamellar thickness has been shown to have a large impact on the creep resistance with thin lamellae showing improved creep resistance [20, 46, 88]. To alleviate both problems, the stepped cooling sequence was developed and applied. Advantages of the stepped cooling are that the massive transformation and early precipitation of the β -phase can be avoided as well as producing interlocked grain boundaries and relatively thin lamellae.

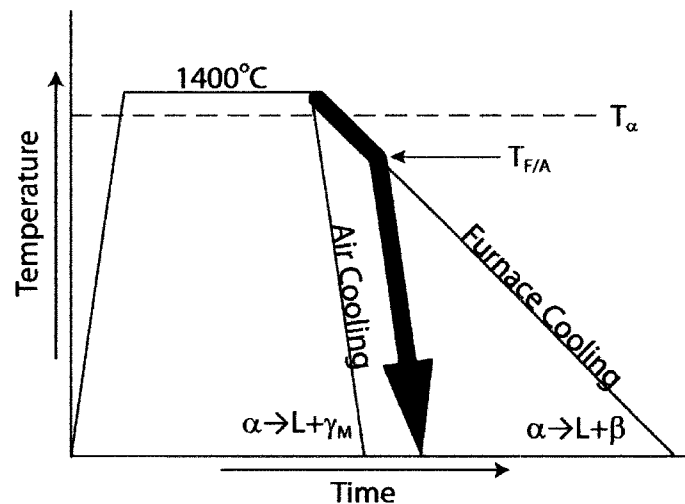


Figure 30 - Illustration of the stepped cooling process during the Step Cooled Heat Treatment (SCHT)

In order to identify the proper $T_{F/A}$, three temperatures were chosen 1290 °C, 1280 °C and 1270 °C. The results showed that 1270 °C was the ideal transition temperature, however, samples held at 1400 °C for 20 min and step cooled to 1270 °C showed bright inclusions (Discussed in further detail in section 5.1.2.1) indicative of incomplete homogenisation. In an effort to completely homogenise the material, a set of samples underwent the SCHAT with a longer hold time of 40 min. $T_{F/A}$ remained constant at 1270 °C. After metallographic analysis (both optical and electron microscopy techniques), the ideal SCHAT was determined to be at 1400 °C for 40 min with $T_{F/A}$ of 1270 °C. Table 3 is a summary of the SCHATs performed.

Table 3 - Thermal processing summary for samples not encased in quartz tubes

Temperature / Duration	Transition Temperature ($T_{F/A}$)(°C)		
1400 °C / 20 min	1290	1280	1270
1400 °C / 40 min			1270

Once the optimal SCHAT was developed, a set of samples encased in quartz tubes were heat treated at 1400 °C for 40 min with $T_{F/A}$ of 1270 °C to see if the absence of quartz tubes had any adverse effects on the microstructure. The quartz tubes used were high purity silica which were back filled with argon and vacuumed five times before being sealed with a final pressure of 200 mmHg argon inside. The samples were each wrapped in Ta foil which is a strong “getter” to react with any oxygen that may diffuse into the tubes at the heat treatment temperature. Ta foil also acted as a diffusion barrier between the samples and the quartz tubes. Upon completing the SCHAT, samples were removed from the furnace and left in the quartz tubes to air cool.

4.1.3.2 Aging

Before aging, HIP'ed samples underwent the optimized SCHT (40 min hold time above T_{α} with $T_{F/A}$ equal to 1270 °C) encased in quartz tubes. After the SCHT, samples were left in the quartz tubes for aging. There were two different types of aging used, isothermal and a stepped aging process. Isothermal aging consisted of heating the samples to 950 °C for times ranging from 8 hrs up to 432 hrs (actual aging times are summarized in Table 4). The samples were then air cooled until they reached room temperature and were then removed from the quartz tubes. The stepped aging consisted of increasing the heat treatment temperature in steps while holding for a length of time at each step (illustrated in Figure 31). The final step was 950 °C with a hold time of 8 hrs and a total heat treatment time of approximately 50 hrs.

Table 4 - Thermal processing summary for samples encased in quartz tubes

SCHT	Aging (hrs) [950 °C]					
1400 °C / 40 min / $T_{F/A} = 1270$ °C	0	8	72	144	432	Stepped

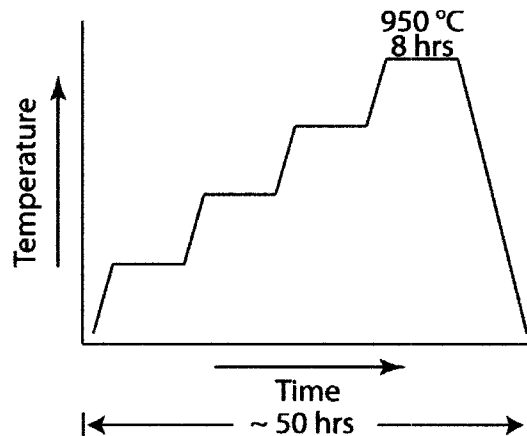


Figure 31 - Illustration of the stepped aging process

4.2 Metallography

4.2.1 Sample Preparation

Following the heat treatments, samples were prepared for OM, scanning electron microscope (SEM) and transmission electron microscope (TEM) analysis. The small 1.5 – 2.0 cm samples for the initial SCHT and aging investigations were sectioned perpendicular to the axis of the sample using a Buehler IsoMet 2000 with a diamond wafering blade as shown in Figure 32. Cuts were made to produce two 3 mm thick pieces for each sample which were used for OM and SEM analysis.



Figure 32 - Buehler IsoMet 2000 with a diamond wafering blade

To prepare samples for OM, they were first mounted in Bakelite. The samples were mechanically polished from 240 to 1200 grit using a polishing wheel in Figure 33. Iron oxide followed by a colloidal silica solution was then used to produce a mirror finish. The TiAl etchant described in Table 5 was used to reveal the grain structure for OM analysis.

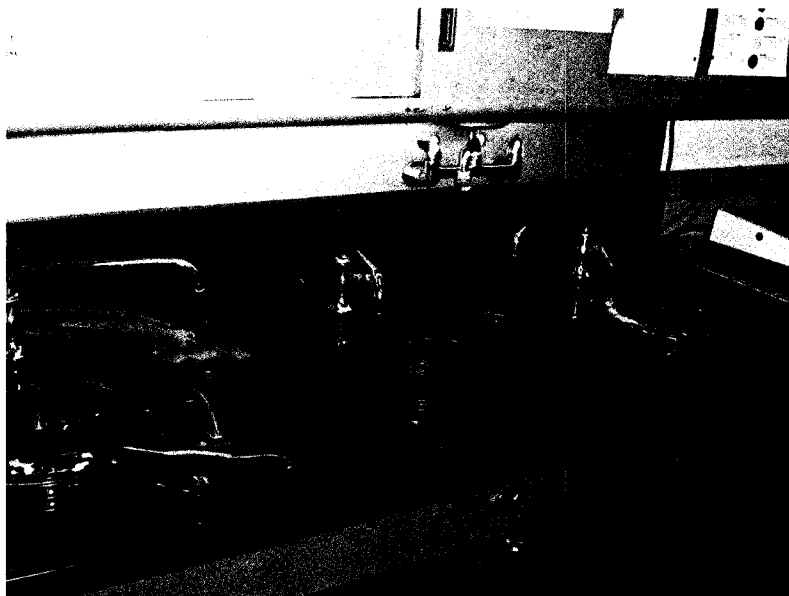
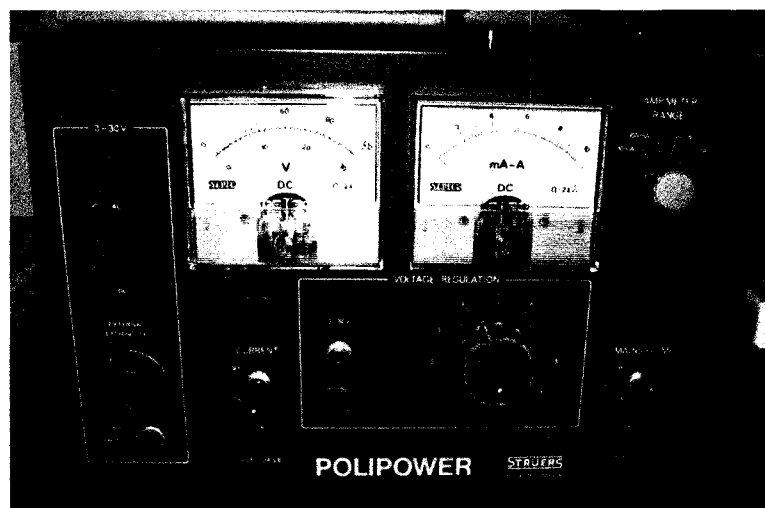


Figure 33 - Polishing wheels for metallographic samples

Table 5 - TiAl etchant composition

Volume (mL)	Chemical
25	Glucose
1	Hydrofluoric Acid
12	Nitric Acid
12	Water

Samples for SEM analysis were prepared by mechanically polishing to 600 grit and then electro-polishing for 3 min in the solution described in Table 6 using a Struers Polipower (Figure 34). Electro-polishing was performed with a voltage of 30 V when the solution was at -30 °C. A picture of the complete setup for electro-polishing can be seen in Figure 35.

**Figure 34 - Struers Polipower, used to electro-polish SEM samples**

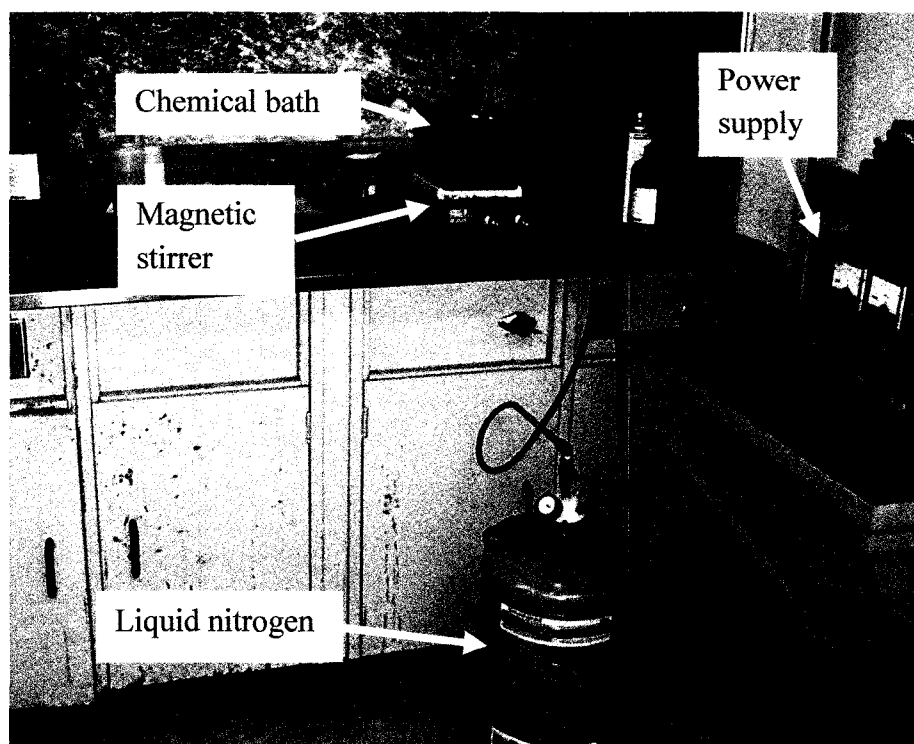


Figure 35 - Electro-polishing setup

Table 6 - Electro-polishing solution

Volume (%)	Chemical
31	Butanol
64	Methanol
5	Perchloric Acid (70 – 75%)

An additional cut was made on each sample to produce a ~0.5 mm thick wafer to make TEM foils. The wafers were glued to a glass block to aid in polishing and were ground to roughly half the initial thickness using 400 grit then 600 grit sand paper. Acetone and a razor blade were used to carefully remove the wafer from the glass block without bending it. The wafer was then glued to the glass block again with the unpolished side exposed. The wafer was polished down to 600 grit and made as thin as

possible. Acetone and a razor blade were used again to carefully remove the wafer from the block. A punch was then used to cut out small foils 3 mm in diameter from the larger wafer. Each wafer was able to yield 8 – 10 of the 3 mm foils. The TEM foils were prepared using a twin-jet polisher (Struers Tenupol – 3) with a solution. Detailed information on the polishing solution and operating parameters are shown in Table 6 and Table 7.

Table 7 - Twin-jet polishing parameters

Parameter	Value
Voltage (V)	13-15
Current (mA)	20-30
Flow Rate Setting	5.5
Photo Sensitivity Setting	0.5
Temperature (°C)	-45

Following creep testing, samples underwent the following preparations before metallographic analysis was possible. One of the two fractured pieces of the as crept sample was cut along its axis to produce two halves of roughly equal size, Figure 36. The Buehler IsoMet 2000 with a diamond wafering blade, Figure 32, was used to make these cuts. One half was prepared for SEM analysis and the other for OM analysis. Each half underwent similar processes as already detailed above for their respective analysis route. In the majority of cases, the samples after fracture were too long for the diamond wafering blade to cut through the samples along their axis in one pass. To remedy this, a transverse cut was made once the wafering blade had reached its maximum cut depth within the sample. The transverse cut was made typically around the notch used to anchor the extensometer during creep testing. Once the two halves of the gauge section were cut

from the original fracture half, axial cutting was resumed and proceeded into the grip section. Once the maximum blade depth was again reached, a final transverse cut was made which produced two grip section samples for metallographic analysis. The same effect was achieved in this manner as a single cut along the sample axis except that instead of one long piece, there were now two short pieces, Figure 37. This also allowed the pieces to be mounted in Bakelite for OM preparations since the press required to solidify the Bakelite has a limited diameter. In each case, care was taken to preserve the fracture surface.

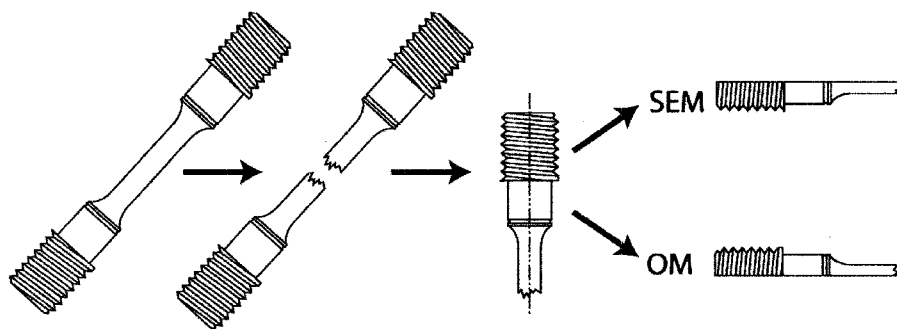


Figure 36 - Illustration showing the cut to produce SEM and OM samples

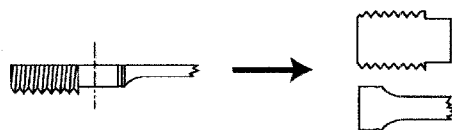


Figure 37 - Illustration showing the product of the axial and transverse cuts described above

TEM samples were made from the remaining untouched half of the fractured sample. A number of transverse cuts were made producing wafers approximately 0.5 – 1 mm thick. The wafers were polished as was described above for the TEM foil production.

4.2.2 Microstructural Analysis Techniques

4.2.2.1 OM, SEM and TEM Analysis

An Olympus PMG-3 optical microscope (Figure 38) equipped with a CCD camera and Quartz PCI software for image acquisition was employed to produce all of the optical micrographs.



Figure 38 – Olympus PMG-3 optical microscope

A Philips XL30S FEG (Field Emission Gun) equipped with an EDAX Phoenix system (Figure 39) was used to conduct SEM analysis. Secondary electron (SE), back scattered electron (BSE) and energy dispersive spectroscopy (EDS) techniques were utilized to analyze the microstructure in detail. The accelerating voltage used was 20 kV.

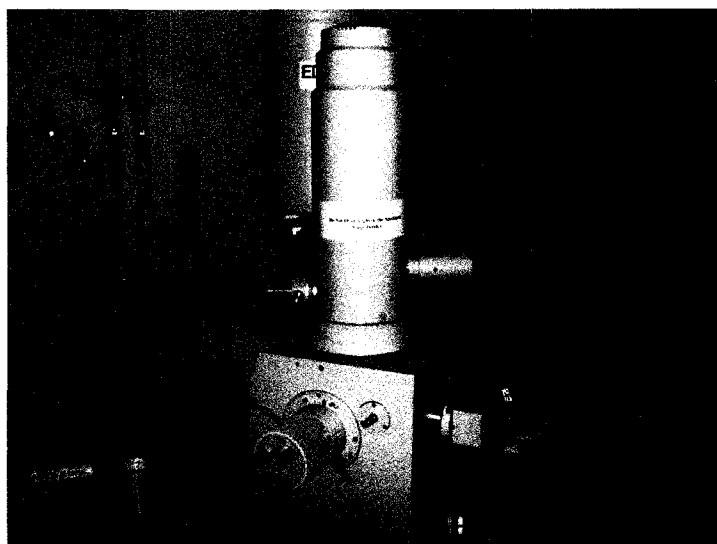


Figure 39 – Philips XL30S FEG equipped with an EDAX from Phoenix Systems

A Philips EM430 (Figure 40) equipped with a dual axis goniometer was used to allow tilt on both the x and y axes to locate the required zone axis. Selected area diffraction (SAD) and dark field (DF) techniques were also used to analyze the microstructure. Tilt angles of up to 35° were achievable using the Philips TEM. To analyze the lamellar structure and precipitates in detail, bright field and angular dark field techniques were utilized using a Jeol JEM-2100F scanning transmission electron microscope (STEM), Figure 41. In particular, EDS analysis under STEM mode was conducted to examine composition of precipitates and their surrounding area.

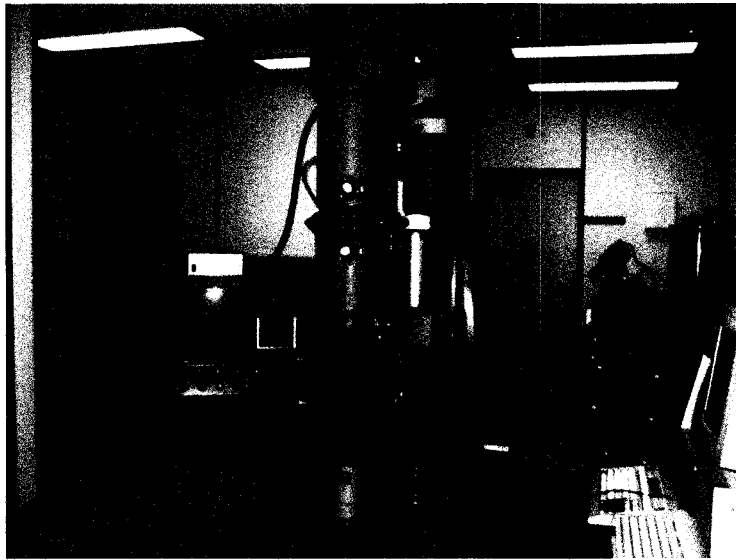


Figure 40 - Philips EM430 STEM

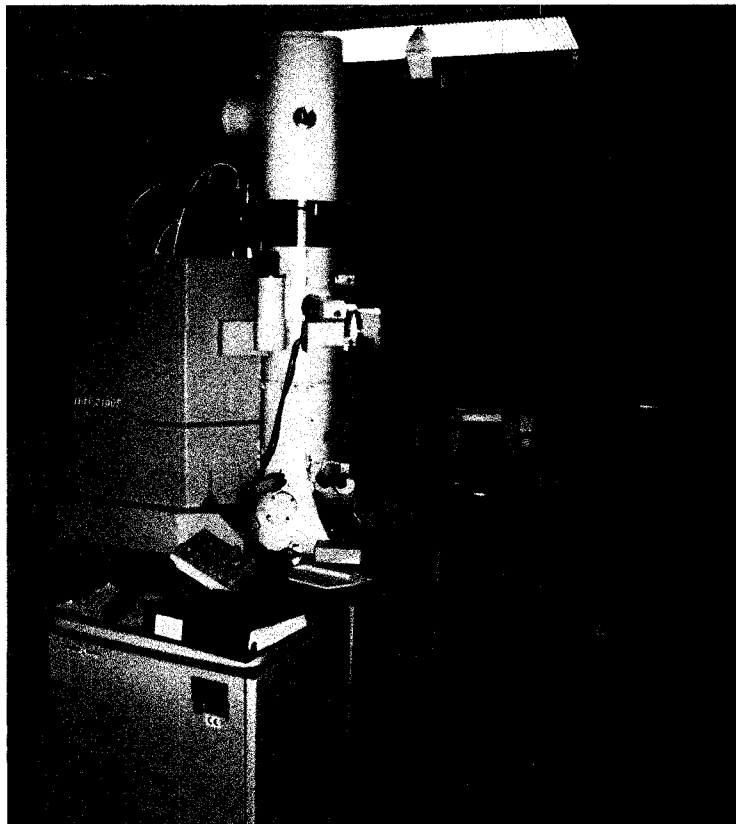


Figure 41 - Jeol JEM-2100F field emission electron microscope

4.2.2.2 Equiaxed γ Measurements

A transparency was placed on a printed copy of the optical micrograph to be measured. The areas containing equiaxed γ were coloured in with a black marker and the edges of the micrograph were marked on the transparency. The transparency was then scanned and converted to a black and white image using Scion Image from the Scion Corporation. A histogram was used to find the total number of both black and white pixels in the picture compared to the total number of black pixels which represents the amount of equiaxed γ contained within the micrograph. Two optical micrographs were used for each condition. This method was chosen over computer analysis since analysis software typically uses different shades to differentiate between microstructural features. The problem with using different shades is that in the case of the samples being studied, the equiaxed γ , along with the FL grains, share similar shades of grey. Therefore, it was necessary to visually determine which features were equiaxed γ and which were part of the FL grain or γ_m .

4.2.2.3 γ_m Measurements

Measurements of γ_m were completed in a similar manner to the equiaxed γ measurements. Two optical micrographs for each condition had a transparency placed on top of them and all the areas containing γ_m were coloured in. The transparency was then scanned into the computer and the image converted to a black and white picture. The number of black pixels over the total number of pixels in the scanned image gave the fraction of γ_m present in the micrograph.

4.2.2.4 Grain Size Measurements

Grain size ranges were examined by utilizing a manual OpMark no. AR-6-15cm linear distance indicator manufactured in Korea. Measurements were taken from a number of grains across two optical micrographs in each heat treatment condition.

4.3 Mechanical Testing Procedures

Hardness, tensile and creep tests were carried out to evaluate the mechanical properties of the PM titanium aluminide alloys. Details are listed in the following sections.

4.3.1 Sample Preparation

Samples for the hardness testing underwent similar preparation procedures as the samples for the OM analysis. The samples were mounted in Bakelite and polished until a mirror finish was obtained. In some instances a very light etch was used to make grains slightly visible so the hardness indentations could be placed within the grain.

For tensile and creep testing, deviations from the smaller sample preparation paths were made. Powder consolidation and HIP'ing procedures were identical, however, following decanning, the bars were left in 3" lengths as opposed to be sectioned into smaller 1.5 – 2 cm lengths for the SCHAT and aging analysis. The bars were wrapped in Ta foil and encapsulated in quartz tubes with ~200 mmHg Ar atmosphere. They were then heat treated by the SCHAT of 1400 °C for 40 min with a $T_{F/A}$ of 1270 °C. The bars were further aged for times varying from 8 to 144 hrs as well as one set of samples (0, 0.5 and 1%W) which underwent the stepped aging treatment. Once the heat treatments were

completed, the Ta foil and quartz tubes were removed and the 3" bars sent to MetCut (3980 Rosslyn Drive, Cincinnati Ohio, 45209-1110) for machining. A low stress grinding technique was used to minimize stresses that may influence the mechanical properties. The machined samples had a straight gauge length of 0.791" and a diameter of 0.158". Samples for tensile and creep testing have the same dimensions. Detailed dimensions are shown in Figure 42 and a machined sample is shown in Figure 43.

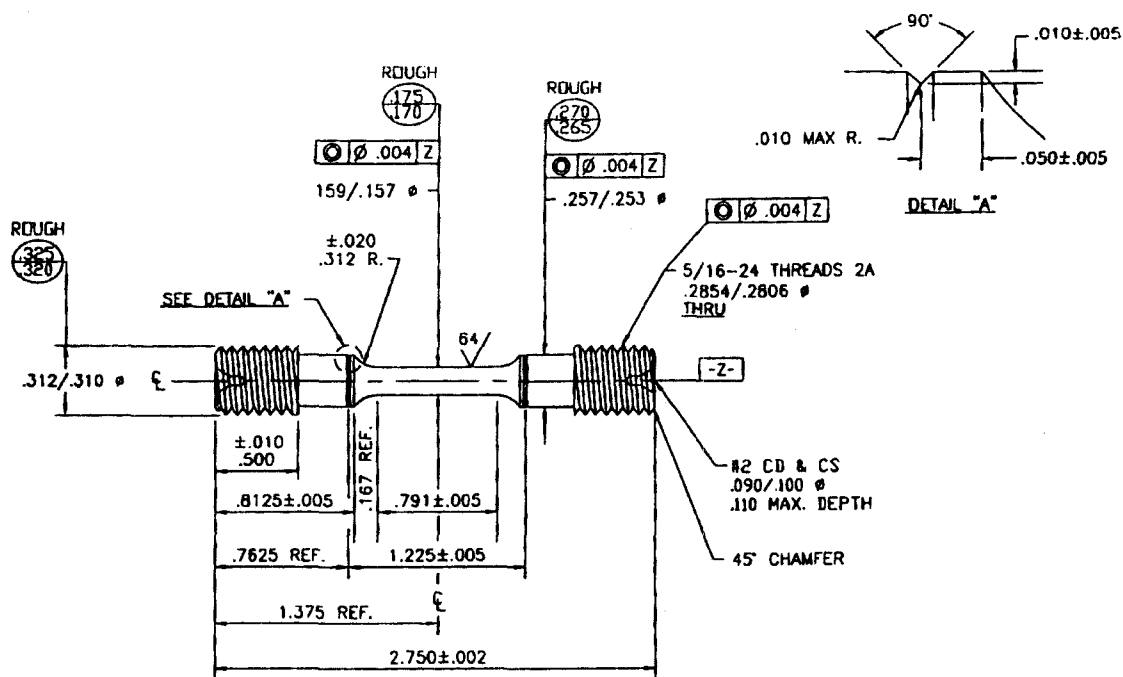


Figure 42 - Detailed creep and tensile sample dimensions

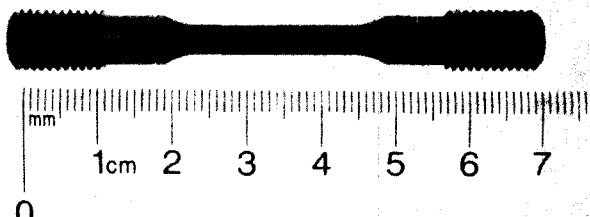


Figure 43 - Machined tensile / creep specimen

4.3.2 Hardness

A LECO LM-247AT micro-hardness tester (Figure 44) was used to conduct Vickers micro-hardness tests for each heat treatment condition. A load of 100 g and a dwell time of 8 sec was used to produce 1 indentation within 10 different lamellar grains in each sample. The values reported are the averaged result of the 8 readings after the high and low values were excluded.

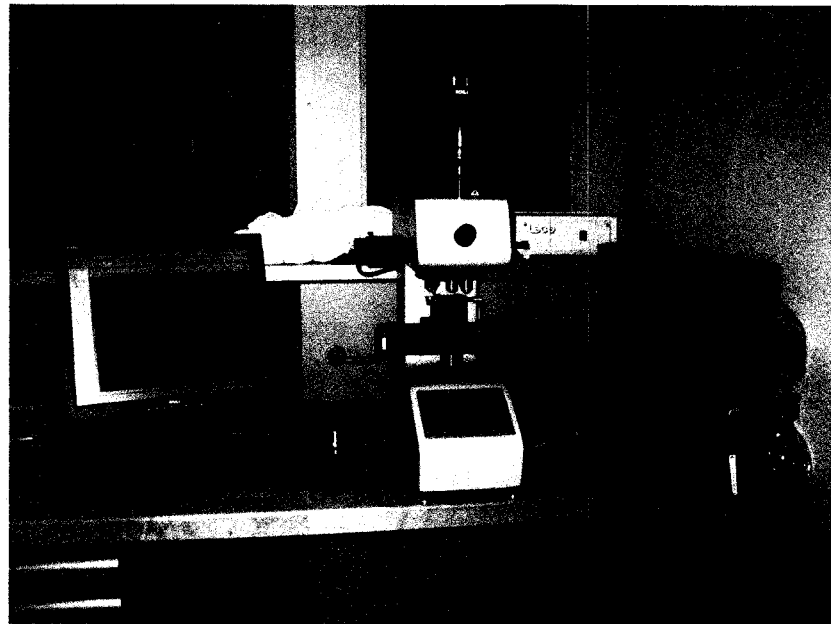


Figure 44 - Leco microhardness tester (LM-247AT)

4.3.3 Tensile

Tensile testing was performed in air at room temperature on a MTS load frame (model 31810) at the Institute for Aerospace Research, National Research Council Canada. Tests were strain controlled with a constant strain rate of 0.004 min^{-1} and ran until fracture.

Strain readings were recorded with an MTS strain gauge (model 632.13M) at a rate of 4 data points/second. One sample was tested for each condition.

4.3.4 Creep

Creep tests were performed on Satec M3 constant load creep rupture frames at Carleton University (Figure 45). ASTM standard E139-06 was used as a guide during testing [89]. The creep samples (shown in Figure 43) were mounted in the load train after all threaded connections were secured and coated in boron nitride. One of two types of extensometers (Satec RT-214 or DA-214) (shown in Figure 46) were connected to grooves in the specimen shoulders to measure the elongation of the samples during testing. Attached to the extensometers was either one or two Solartron Metrology Linear Variable Displacement Transducers (LVDT) (AX/1.5/S – 20119) with an OD5 conditioning unit. Two Omega type K thermocouples were connected to each end of the sample (shown in Figure 47) to ensure a uniform sample temperature in the gauge section throughout testing. The temperatures were displayed on an Omega DP462 digital panel thermometer. The three zone Applied Test System's furnace (Model #: 2961) was controlled using a Leeds and Northrup controller which could vary the temperature in each zone independently.

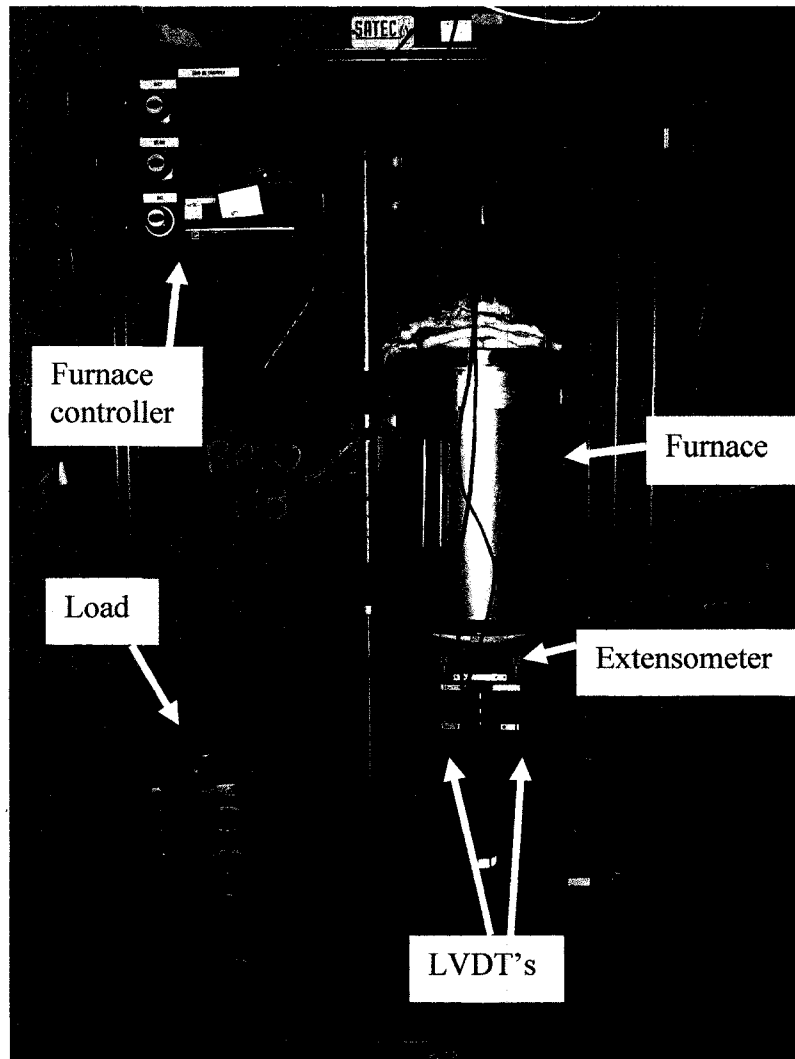


Figure 45 - Constant load creep frame

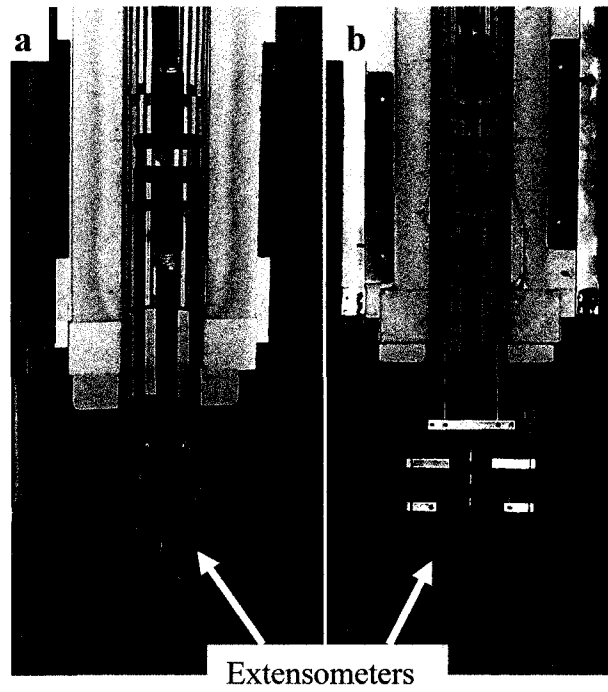


Figure 46 - Satec extensometers; a) single LVDT extensometer (RT-214) and b) dual LVDT extensometer (DA-214)

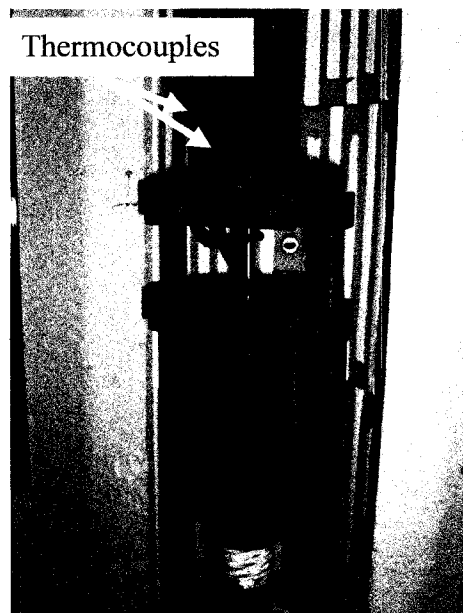


Figure 47 - Creep specimen with two thermocouples attached

Before testing commenced, the sample was mounted in the load train without any load applied. The weights were propped up so that no stress was applied to the sample before testing began. With the furnace closed, the top and bottom sections were insulated with ceramic insulation. The samples were then heated to around 745 – 750 °C and the three furnace zones were adjusted to ensure the top and bottom thermocouples read similar temperatures. Once the difference between the two thermocouples was less than 1 °C and the temperature was stabilized near 750 °C, the temperature was increased to the test temperature of 760 °C. The time it took to reach and balance the temperatures at 750 °C was about 5 hrs. Care was taken during the heating process to ensure the temperature did not overshoot 760 °C at any time. Once the test temperature of 760 °C was reached, the data acquisition system (DAQ) was started and the weights had the supports removed so as to apply a total stress of 276 MPa onto the sample. During testing, the temperature difference between the two thermocouples was maintained below 1 °C and was typically less than 0.5 °C. Once fracture occurred, the furnace was shut off and allowed to cool to room temperature before the sample was removed. Data was recorded at 1 point/sec from 0 – 6 min, then 1 point/min from 6 min – 1 hr and then 1 point/30 min until fracture. One sample was tested in each aging condition and alloy composition.

Chapter 5: Results and Discussion

This section contains the results and a discussion of the work completed throughout the life of this project. The data will be presented as each stage was completed. Initially, work was carried out to develop and optimise the microstructure of the material so HIP'ing results will first be presented, followed by the SHT and aging results. Once the microstructural analysis was completed on all the samples, work then proceeded to validate the microstructures through mechanical testing. Initially hardness tests were conducted to determine selected heat treatment conditions for mechanical testing, tensile and creep evaluation. Due to the large number of micrographs and EDS results generated throughout the microstructural analysis, only a selection of the data will be presented in this chapter.

5.1 Microstructural Analysis

5.1.1 As HIP'ed Condition

Figure 48 and 49 are SEM-BSE and optical micrographs of a 1%W sample in the as HIP'ed condition. The grain size was in the range of 5 – 40 μm and this microstructure served as a basis for comparison with all further heat treatments.

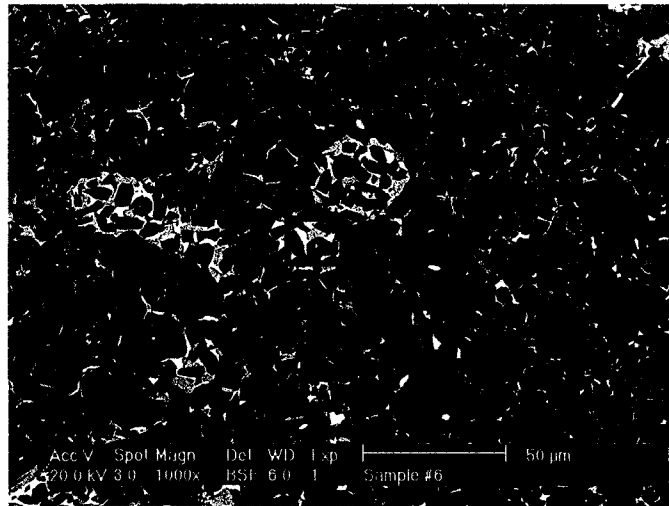


Figure 48 - SEM-BSE micrograph of the 1%W sample HIP'ed for 2 hrs at 1200 °C and 200 MPa (SEM-EDS results from area (a) found in Figure 50)

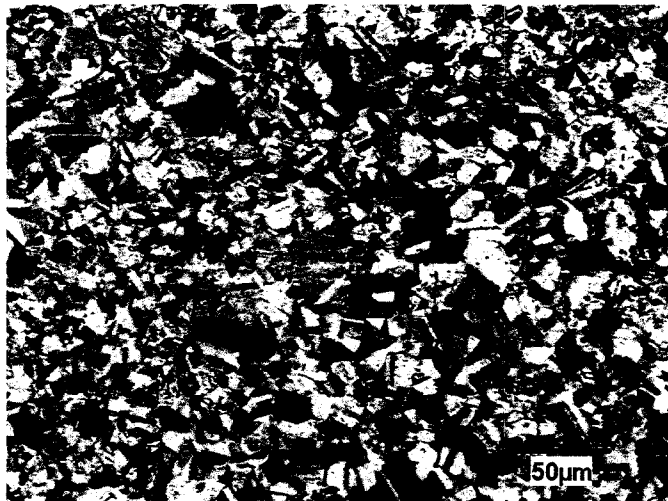
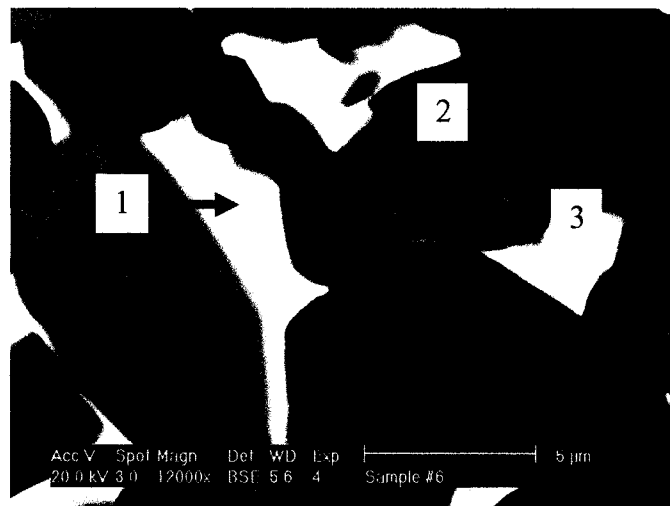


Figure 49 - Optical micrograph of the 1%W sample HIP'ed for 2 hrs at 1200 °C and 200 MPa

SEM-EDS point analysis were conducted to determine the composition of each of the visible phases. Results from the samples containing 1% W show that after HIP'ing, the bright areas from SEM images at the grain boundaries are rich in both W and Cr and lean in Al. (See table in Figure 50) The Nb concentration remains relatively uniform across

the three different phases, which agrees with the partitioning coefficient ($K_{\alpha_2/\gamma} = 1.00$) found in literature [90]. The light grey and dark grey areas (spots 2 and 3 from Figure 50, respectively) seem to be α_2 and γ respectively based on their composition. The 0.5% W sample shows similar features. The 0% W sample shows the light grey and dark grey features but due to the absence of W, it does not show the bright white features.



Element	Spot		
	1	2	3
Ti	46.2	51.5	44.0
Al	38.1	41.5	50.9
Cr	6.8	2.6	1.6
Nb	2.4	2.5	2.4
W	6.5	1.9	1.1

Figure 50 - SEM-EDS results from the 1%W sample (in at. %) after HIP'ing (Taken from area (a) in Figure 48)

5.1.2 Step Cooled Heat Treatment (SCHT)

After holding at 1400 °C, the samples must undergo a specific type of cooling to avoid detrimental microstructural features such as Widmanstätten and massively transformed γ ,

γ_m , which may form during cooling. Rapid cooling rates develop γ_m while slow cooling rates form thick lamellae. It is important to avoid both features so the SCHAT was used which initially cools slowly followed by a more rapid air cooling once $T_{F/A}$ is reached. The advantages of this type of stepped cooling are that the massive transformation and early precipitation of the β -phase is avoided. In addition, furnace cooling also promotes interlocked grain boundaries [37] which have been suggested to improve creep resistance [40].

5.1.2.1 Effect of Hold Time above the α -Transus

Initially, a 20 min hold time at 1400 °C was examined and the resulting microstructures can be seen in the SEM-BSE micrographs in Figure 51. The bright white sites are rich in W and Cr, and lean in Al, Figure 52. These segregation sites formed at lamellar grain boundaries and within the grains. Since W diffuses very slowly relative to the other elements [20, 49], the SCHAT time was doubled in an attempt to minimize segregation. The size and number of the bright areas decreased, Figure 53. However, the grain size showed a slight increase as discussed in section 2.1.3.1. For example, Figure 54 is a comparison between samples heat treated to examine the effect of increasing the hold time on grain size. The fully lamellar grain size increased from the range of 225 – 555 μm for the samples heat treated for 20 min to the range of 280 – 595 μm for those heat treated for 40 min. Although larger grains will influence the ductility, creep resistance and strength of the alloys, the small increase in size is not expected to have an overly large influence on material properties [21]. If grain size is minimized though, room

temperature ductility can be improved. Reducing the grain size below 100 μm can, however, reduce creep resistance [3]. This means a small grain size can be used to improve room temperature tensile properties without having a large impact on the high temperature properties. However, to fully homogenize the microstructure, longer times in the single phase α region are required, which is why SHT times were increased to 40 min. The hold time of 40 min was chosen as acceptable since it was able to minimize W and Cr segregation while not having a significant impact on grain size.

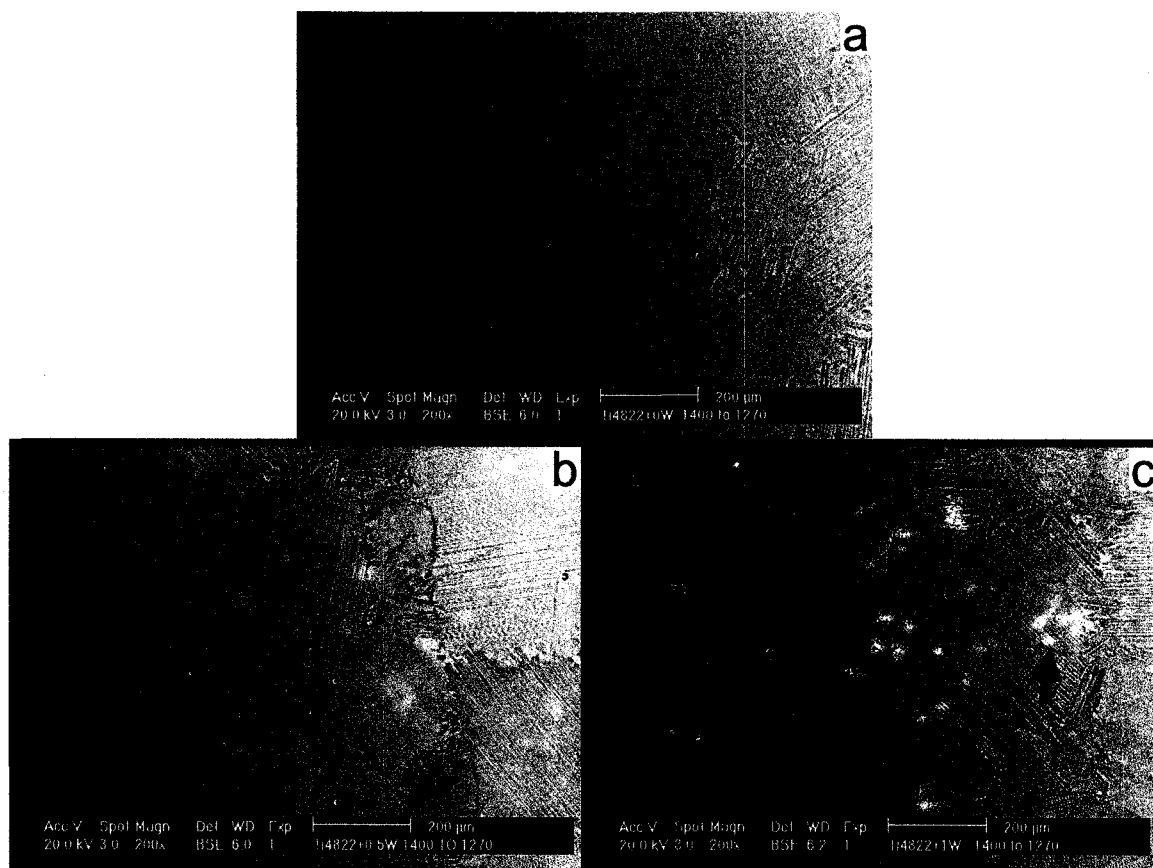
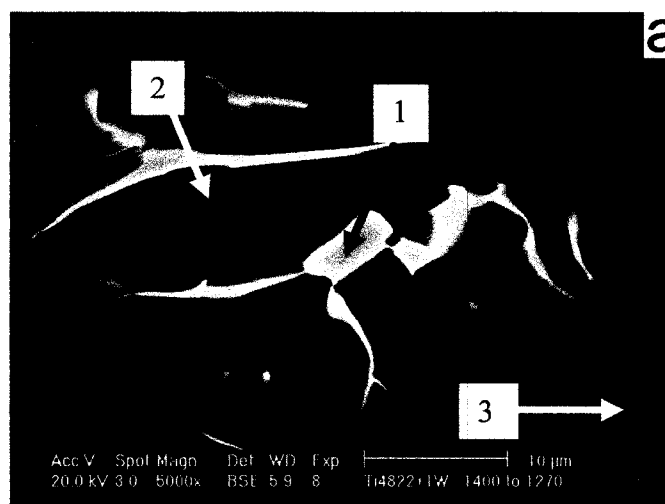
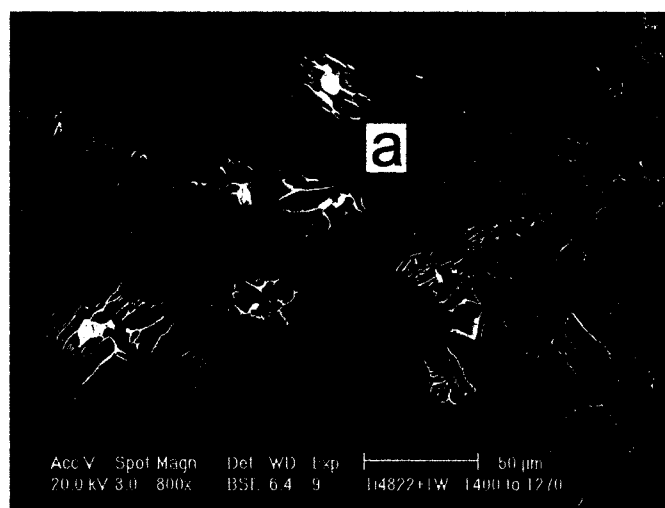


Figure 51 - SEM-BSE micrographs of a) 0%W, b) 0.5%W, and c) 1%W taken after 1400 °C for 20 min with $T_{F/A} = 1270$ °C. Bright spots (arrows) are W and Cr rich areas.



Element	Spot		
	1	2	3
Ti	47.52	42.66	44.32
Al	40.97	52.29	50.41
Cr	5.15	1.38	1.86
Nb	2.58	2.40	2.38
W	3.78	1.26	1.04

Figure 52 - SEM-EDS results from the 1%W samples (in at.%) after 1400 °C for 20 min with $T_{FA} = 1270$ °C.

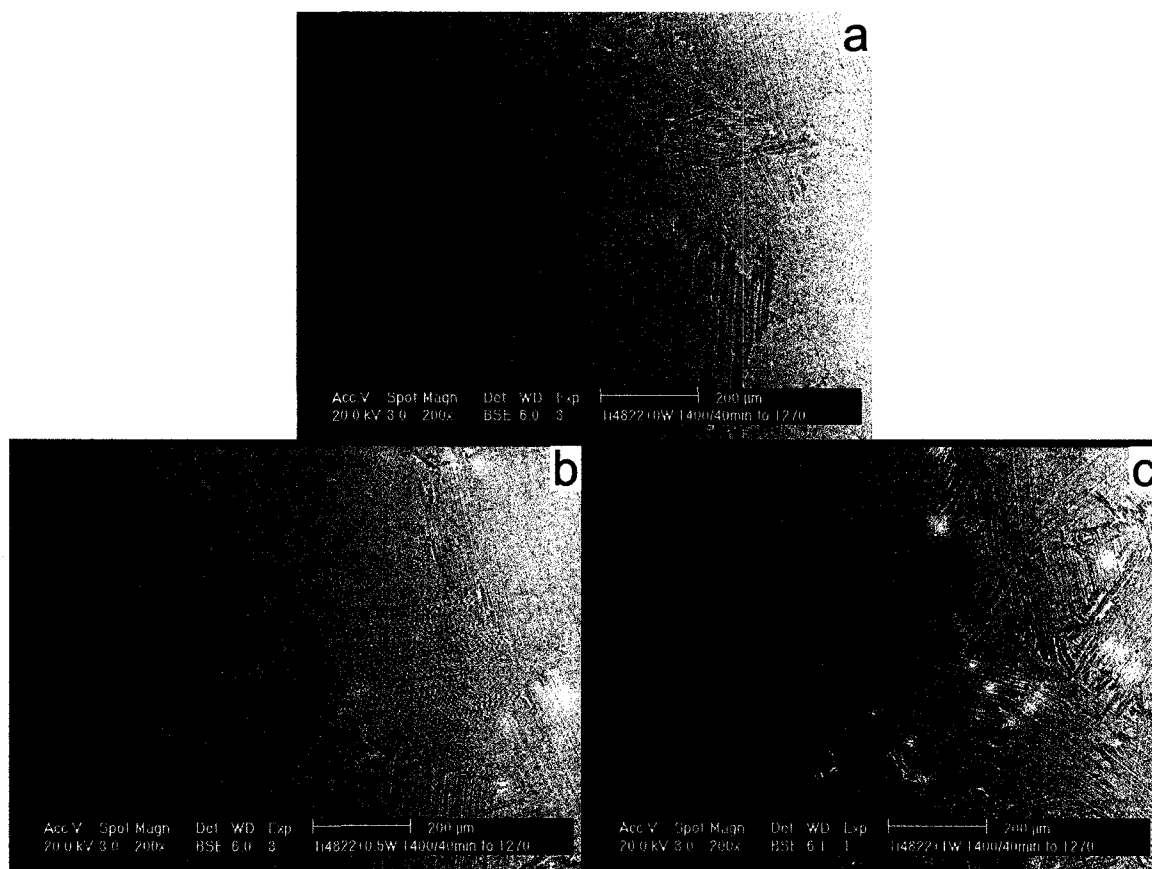


Figure 53 - SEM-BSE micrographs of a) 0%W, b) 0.5%W, and c) 1%W taken after 1400 °C for 40 min with TF/A = 1270 °C. Bright spots (arrows) are W and Cr rich areas.

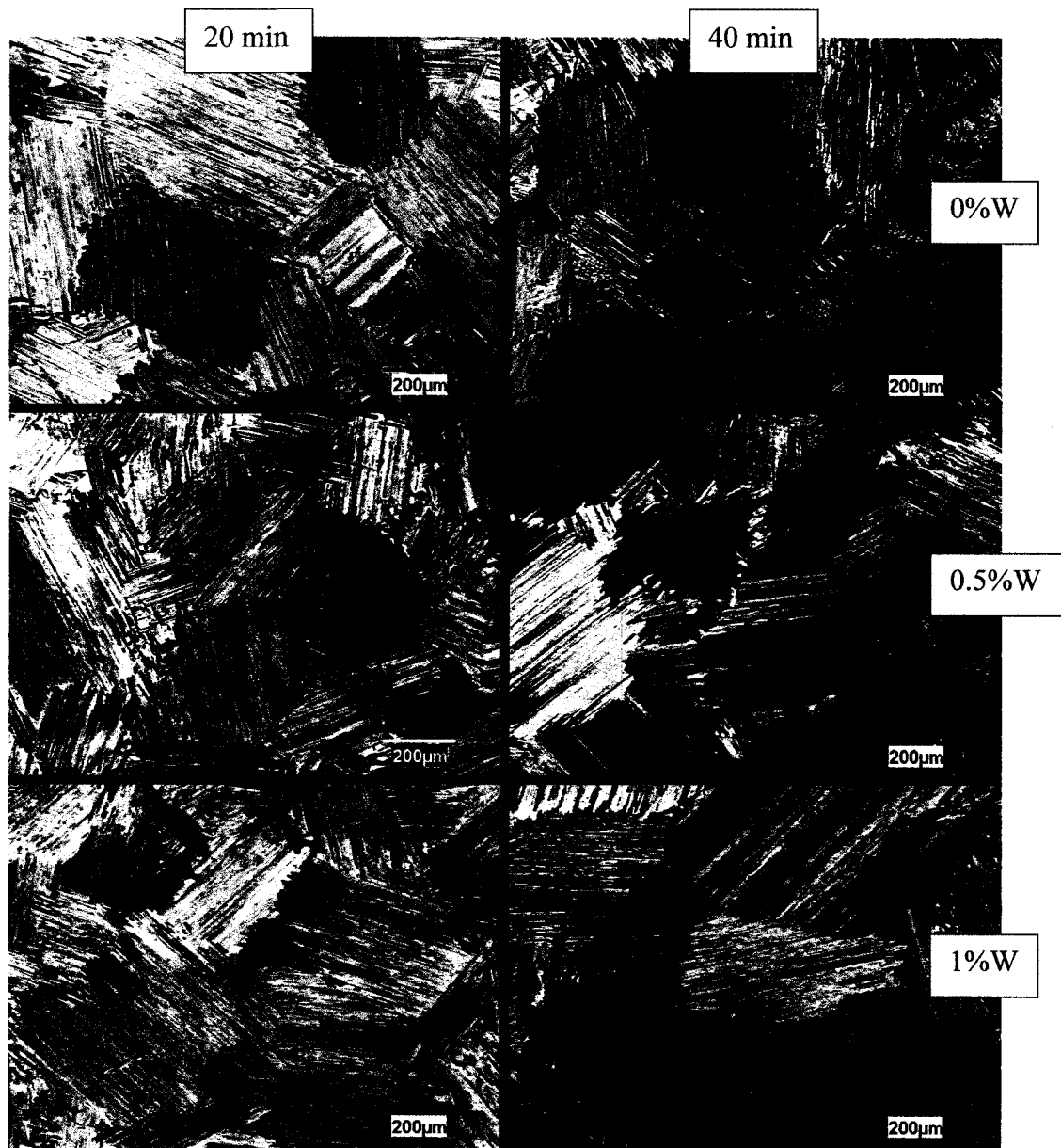


Figure 54 - Comparison of optical micrographs in the SCHAT condition with hold times of 20 and 40 min

5.1.2.2 Effect of Transition Temperature ($T_{F/A}$)

As shown in Figure 55, a set of micrographs for each composition has been compiled to illustrate the effects of W content and transition temperature ($T_{F/A}$) on the microstructure.

By altering W content and $T_{F/A}$, the amount of γ_m (see arrows in Figure 55) produced during cooling was affected. It was found that increasing the W level in the samples had mixed effects on the amount of γ_m depending on $T_{F/A}$. In addition, reducing $T_{F/A}$ drastically reduced the amount of γ_m as shown in Figure 56.



Figure 55 - Optical micrographs illustrating the effects of varying transition temperature and composition. Arrows indicate γ_m .

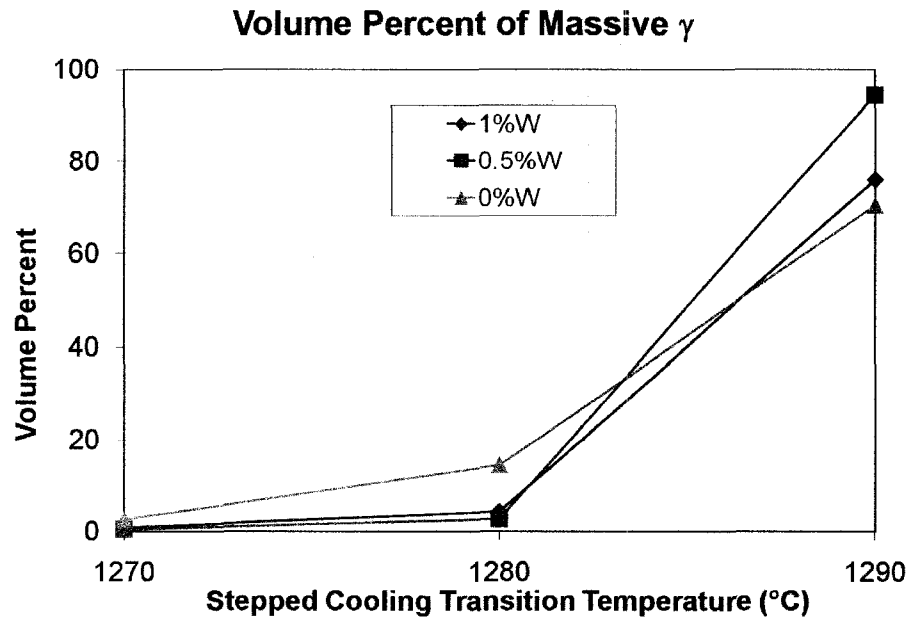


Figure 56 - Volume percent of massive gamma produced during cooling while varying the transition temperature

The most noticeable change in γ_m content was the result of varying $T_{F/A}$. As $T_{F/A}$ is reduced from 1290 °C to 1270 °C, the amount of γ_m produced is reduced substantially from over 60% in each case to almost 0%. (See Figure 56) By lowering the transition temperature, the slower furnace cooling rate (~ 12 °C/min) is prolonged or extended to lower temperatures. This gives the alloy more time to form the FL microstructure and avoid the large undercooling required to cause the $\alpha \rightarrow \gamma_m$ transformation. If the γ_m start temperature is reached before the FL transformation has completed, γ_m will form in the sample. Once the FL transformation has completed, the lamellae will begin to thicken so the transition from furnace cooling to air cooling is made in an attempt to minimize this effect.

The second factor affecting the amount of γ_m is W content. Figure 56 shows that the effect from W on the fraction of γ_m is dependent on $T_{F/A}$. When $T_{F/A}$ is 1290 °C, the addition of W has a negative impact, forming additional γ_m . However, if $T_{F/A}$ is reduced to 1280 °C, the W additions are beneficial and reduce the amount of γ_m . When $T_{F/A}$ is further reduced to 1270 °C, W content no longer has an impact on the volume fraction of γ_m formed. The results seen at 1290 °C are analogous to previous work from Prasad and Chaturvedi [58]. Prasad found that if the rate of diffusion within a ternary TiAl alloy is decreased, less undercooling will be required to cause the γ_m transformation. A ternary alloy with Nb additions was examined and it was postulated that since Nb is a high melting alloying element, the diffusivity of the system would decrease. The reduction in diffusivity would make it easier to form γ_m since the long range diffusion required for the FL transformation was depressed. So it would seem reasonable to assume that if Nb increases the susceptibility of a γ_m transformation, W would likely do the same. W diffuses slowly throughout the TiAl alloy [20, 49], and is a high melting point alloying element. Therefore, it is speculated that W additions will likely reduce the diffusion rates within the TiAl system under investigation which in turn will make it easier for the γ_m transformation to occur.

As $T_{F/A}$ is reduced to 1280 °C, the slower furnace cooling extends to a lower temperature. By allowing this to happen, diffusion has more time to proceed and the system remains closer to its equilibrium composition, reducing free energy. The impact of reduced diffusivity in the system due to W additions would be lessened since there is

additional time to allow the long range diffusion to proceed before transitioning to air cooling. Once air cooling begins after 1280 °C, there is no longer sufficient free energy remaining to successfully nucleate and grow γ_m .

One other competing mechanism is a shift in the phase diagram due to W which moves the two phase $\alpha + \gamma$ region to the right [90]. By shifting the phase diagram, the T_0 line (which is associated with the γ_m start temperature, see section 2.1.3.4 – Massive Transformation) will also shift causing a reduction in the available driving force to form γ_m for an otherwise identical composition (Illustrated in Figure 57).

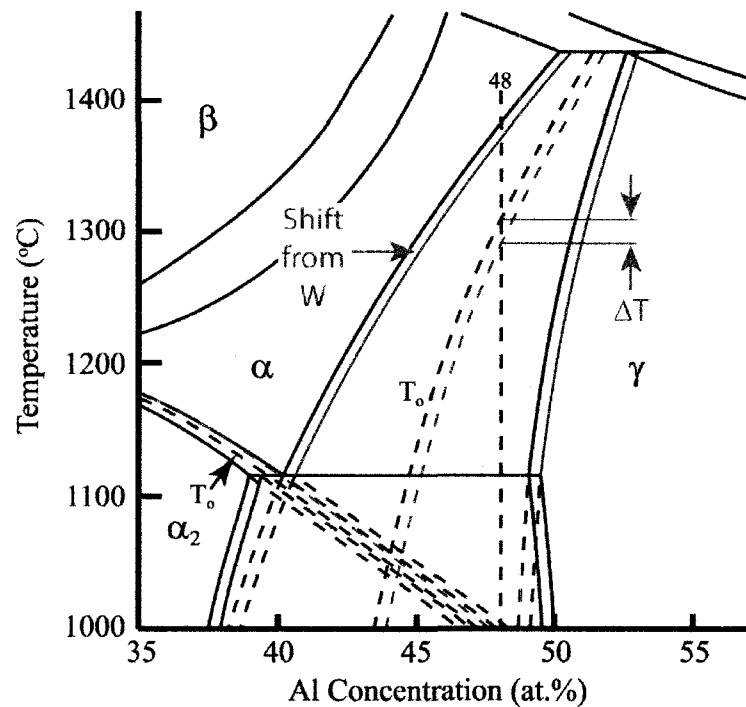


Figure 57 - Possible phase diagram shift due to W additions. ΔT indicates the temperature reduction caused by the shift in the T_0 line. Modified from [57]

Wang had suggested that the available driving force was the distance between the T_0 line in the $\alpha + \gamma$ region and the T_0 line in the $\alpha_2 + \alpha$ region. If the phase diagram is shifted

slightly to the right due to W additions, then the distance between the two T_0 lines will shrink thereby reducing the available driving force as well. The material must, therefore, undergo a higher cooling rate to nucleate and grow γ_m .

This shift could be enough so that the T_0 line will not be crossed during cooling or at least the FL and $\alpha \rightarrow \alpha_2$ transformations will be completed before it does. Further reducing $T_{F/A}$ to 1270 °C eliminates almost all of the γ_m .

1270 °C was selected as the ideal $T_{F/A}$ since it avoided any γ_m formation in the three compositions and produced relatively fine lamellae. The results found in section 5.1.2 show the optimum SCHAT to have a hold time of 40 min and a $T_{F/A}$ of 1270 °C. This generates a microstructure free of any deleterious phases while maintaining a reasonably homogenous FL microstructure with a minimized grain size.

The composition of five areas at low magnification on each of the three conditions (0%W, 0.5%W and 1%W) were examined using the SEM-EDS standardless techniques. The results were averaged to determine the composition of the alloys and compared to the composition measured by Crucible Research. The results are shown in Table 8. The variation between compositions in Table 8 (difference between SEM-EDS and Crucible Research results) is observed due to the limitation of this standardless method. However it is reasonable to use the compositional data provided by the EDS for comparison within these alloys.

Table 8 – Semi-quantitative SEM-EDS results after the optimized solution heat treatment, average of 5 large area scans for each composition (40 min hold time, $T_{F/A}$ of 1270 °C)

	Condition					
	0%W		0.5%W		1%W	
	SEM-EDS	Crucible Research	SEM-EDS	Crucible Research	SEM-EDS	Crucible Research
Ti (at.%)	45.8	47.96	45.3	48.10	45.6	47.20
Al (at.%)	50.0	47.74	50.0	47.54	48.8	47.80
Cr (at.%)	2.0	1.97	1.9	1.86	2.0	1.98
Nb (at.%)	2.3	2.03	2.1	1.82	2.3	1.87
W (at.%)	--	--	0.7	0.45	1.3	0.91

5.1.3 Aging

During the SCHT, the air cooling from 1270 °C to room temperature created a metastable lamellar microstructure of a larger volume fraction of the α_2 phase than would be formed under equilibrium conditions. Aging reduced the amount of α_2 and stabilized the microstructure. In addition, aging was used to form precipitates at the lamellar interfaces and grain boundaries in W containing samples. Two different types of aging were examined: isothermal and stepped aging. The following sections elucidate the effects of aging in terms of equiaxed γ formation, lamellar coarsening mechanisms and precipitate formation.

5.1.3.1 Equiaxed γ and Discontinuous Coarsening

Figure 58 shows a comparison of microstructures in the different aging conditions. Measurable changes are apparent. The first is discontinuous coarsening which causes the ends of the γ lamellae to thicken and join together while growing into adjacent grains. The second is the formation of equiaxed γ at the grain boundaries. The driving force

causing γ to form is the reduction in interfacial and chemical free energies [35]. It appears that the addition of W retards the formation of equiaxed γ and discontinuous coarsening as aging proceeds. Stepped aging also appears to minimize the formation of equiaxed γ and discontinuous coarsening. This is reinforced by the data in Figure 59 which plots the volume fraction of equiaxed γ as a function of aging time. It can be seen that the volume fraction of equiaxed γ increases with aging time, however, in the alloys containing W, equiaxed γ gradually increases to only 7% even after 432 hrs aging. In particular, stepped aging does not show any evidence of the formation of equiaxed γ following the heat treatment. Aging at 950 °C for up to 432 hrs stabilized the metastable FL microstructure by reducing the volume fraction of α_2 in part through the formation of equiaxed γ and discontinuous coarsening.

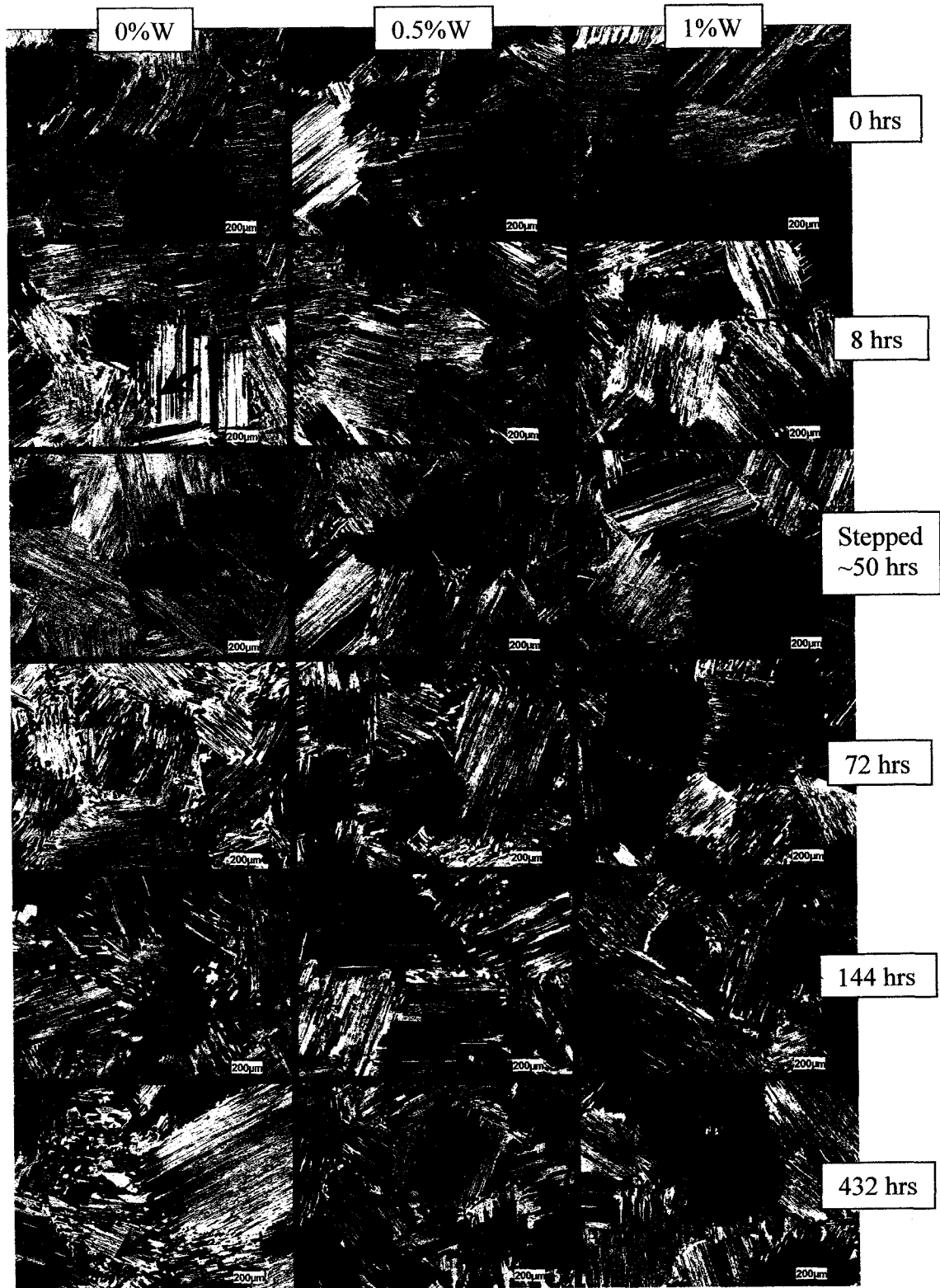


Figure 58 - Optical micrographs showing a comparison of the different aging times. Arrows indicate equiaxed γ formation.

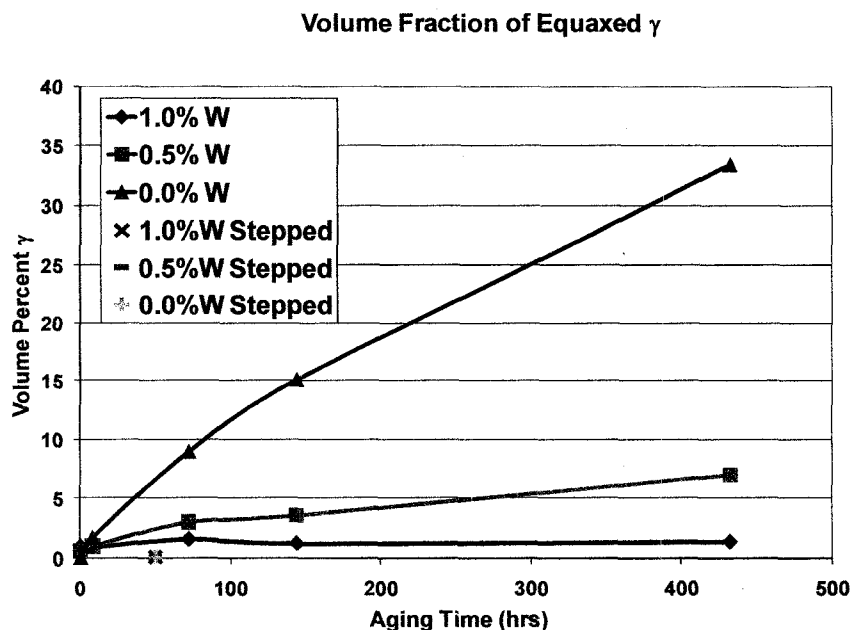


Figure 59 - Volume fraction of equiaxed γ in each of the aging conditions

W additions could retard nucleation and growth of γ grains through the following mechanisms. Firstly, W could stabilize the α_2 lamellae as was previously discussed in section 2.2.1.3. Larson et al. had discussed how W could stabilize the α_2 lamellae against the coarsening of the γ lamellae [80]. Larson has suggested that the sluggish diffusion of W will slow the growth of the γ lamellae because as the γ lamellae thicken, redistribution of W will have to occur. It is possible that a similar mechanism will occur during equiaxed γ growth at the grain boundaries. For the equiaxed γ grains to grow into adjacent FL grains, dissolution of the α_2 lamellae must occur starting first at the FL grain boundary and moving further into the FL grain as the equiaxed γ grain grows. Similar to what Larson has described, a high concentration of W is expected to form at the boundary between the FL and equiaxed γ grain that will be forced to repartition to the remaining α_2

lamellae as growth of the equiaxed γ grain proceeds. Additionally, it is possible the high concentration of W will stabilize the β phase and cause precipitates to form ahead of the equiaxed γ grain, further slowing its growth.

Secondly, W forms precipitates during aging since it is a strong β phase stabilizer. The formation of precipitates at the grain boundaries is expected to reduce the Gibbs free energy of the system and thereby reduce the driving force causing equiaxed γ nucleation and growth.

Stepped aging appears to reduce the amount of equiaxed γ through different mechanisms. Stepped aging appears to increase the γ volume fraction by a reduction in the α_2 lamellar thickness as opposed to the nucleation of new γ grains at the grain boundaries. This can be seen in Figure 59 by the lack of any equiaxed γ forming. It is believed that the activation energy required to nucleate and grow new γ grains is much higher than that required to cause the dissolution of the α_2 lamellae. Since the stepped aging begins at a lower temperature, the slower dissolution of the α_2 phase is given more time to progress. It is not until higher temperatures such as those provided in isothermal aging, is there enough energy to nucleate and grow equiaxed γ grains. By performing holds at increasing temperature steps during stepped aging, ample time is provided to allow the α_2 lamellae to thin and the γ lamellae to thicken thereby reducing the free energy in the system without the formation of equiaxed γ grains at the grain boundaries.

As mentioned previously, discontinuous coarsening occurs when the γ lamellae thicken and join together near the grain boundaries. γ lamellae from one grain will also

grow into adjacent grains if the adjacent grain has thinner lamellae [35]. Discontinuous coarsening occurs for similar reasons as the formation of equiaxed γ , the reduction of interfacial and chemical free energies [35]. As shown in Figure 58, the duration of aging impacts the degree of discontinuous coarsening. Longer aging times increase the amount of discontinuous coarsening. The W additions seem to block or slow discontinuous coarsening by forming precipitates at the grain boundaries and possibly by reducing the diffusion rates across the α_2/γ interfaces. It is also possible that they reduce the chemical free energy by removing W and Cr from the α_2 phase.

The degree of discontinuous coarsening increases with Al concentration [35]. Different alloying additions also affect the degree of discontinuous coarsening. Work from Sreenivasulu et al. [91] shows that in a ternary system, Nb reduces the amount of discontinuous coarsening while Mo increases the amount of coarsening. When both are combined in a quaternary system, the amount of discontinuous coarsening is much higher than in either of the ternary systems [91]. This makes it difficult to predict how alloying elements will interact with each other when basing assumptions on results generated from different ternary compositions.

5.1.3.2 Continuous Coarsening and Lamellar Thickness

Figure 60 is a comparison of SEM-BSE micrographs of the alloys under investigation with different compositions and aging times. Lamellar breakup is easily visible in the 0%W alloy in as short an aging time as 8 hrs and becoming more severe as aging times lengthen as shown in Figure 60. As W is added to the samples, there is less severe

lamellar breakup as aging time increases. Figure 61 shows TEM micrographs from the 0%W and 1%W both aged for 8 and 144 hrs. The TEM micrographs show precipitates at lamellar interfaces in the 1%W alloy as well as less severe breakup compared to the 0%W alloy. In locations where the α_2 phase has broken up, the precipitates remain and maintain a lamellar type interface.

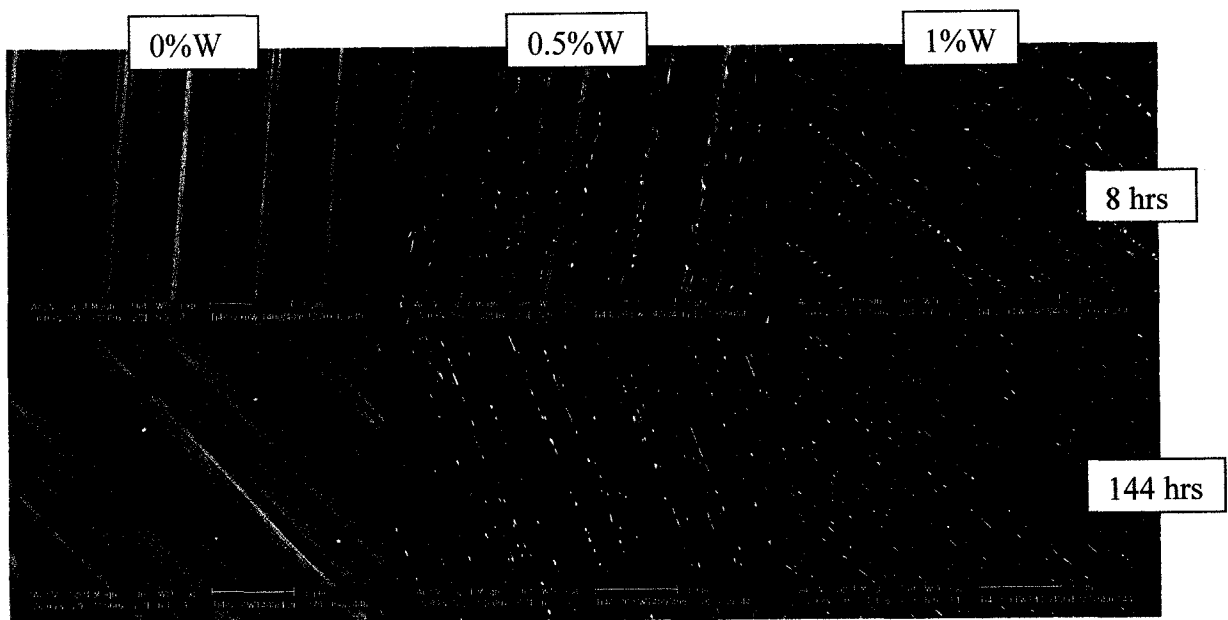


Figure 60 - SEM images comparing 8 and 144 hr aging times. Arrows show break up of lamellae

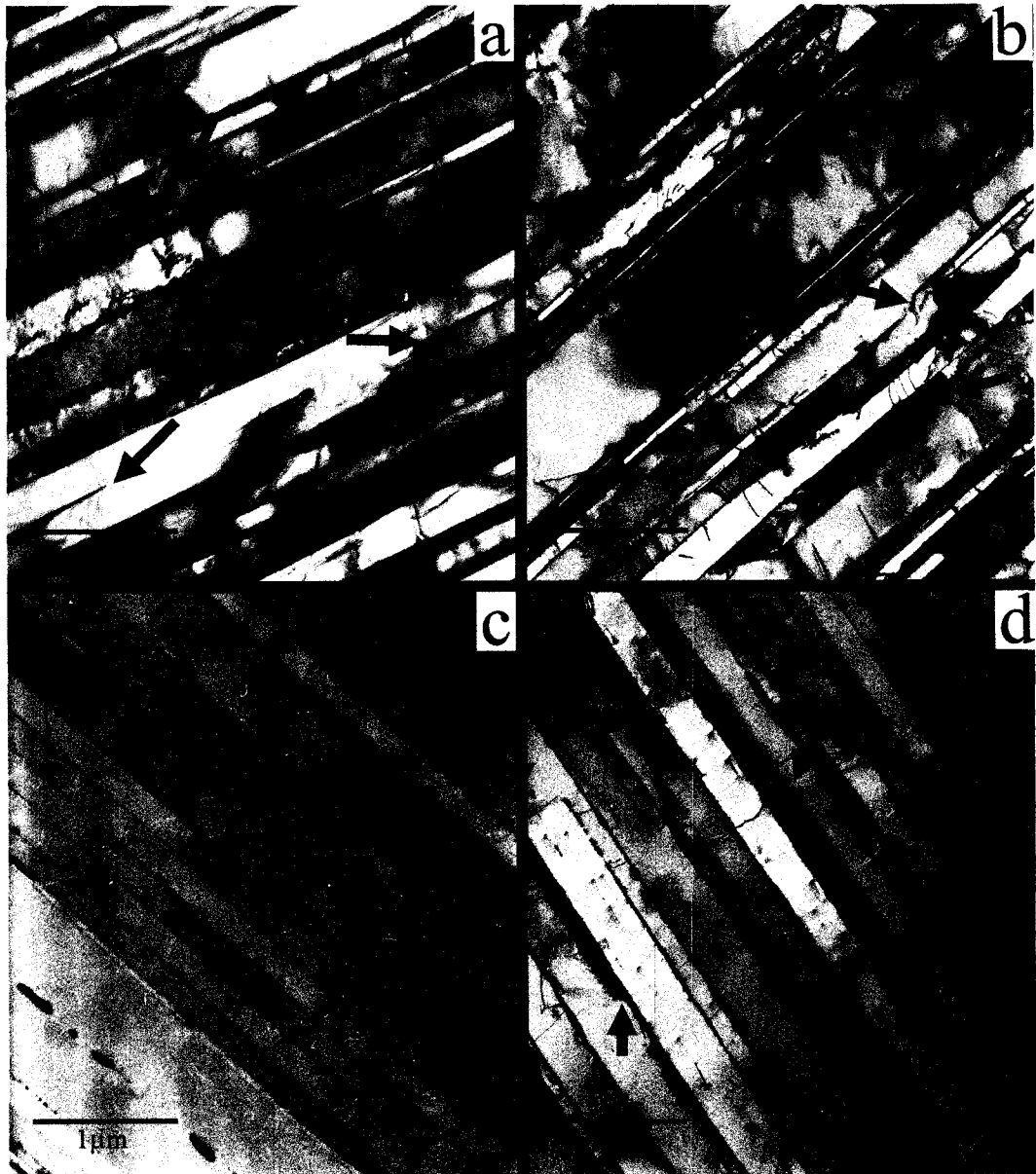


Figure 61 - TEM micrographs with arrows indicating coarsening a) 0%W aged for 8 hrs, b) 0%W aged for 144 hrs, c) 1%W aged for 8 hrs, d) 1%W aged for 144 hrs

Continuous coarsening is a process where the γ lamellae thicken to reduce the total α_2 volume fraction. The process is driven by a reduction in the excess of α_2 which is obtained as a result of the rapid cooling following the SHT. The metastable α_2 lamellae

within the lamellar colonies begin to thin and increase the fraction of γ thereby reducing the fraction of α_2 . Depending on the composition and the aging time, this can result in severe breakup of the α_2 lamellae as shown in Figure 61 and Figure 62. SEM-EDS results in Figure 63 show compositional data suggesting that the white phase (point 1) is the Ti_3Al phase (α_2) while the grey and dark areas (points 2 and 3) closely resemble the TiAl phase (γ). Therefore, the results in Figure 62 and Figure 63 and work from Maziasz et al. [92] suggest that the white phases are the remainder of the α_2 lamellae after severe breakup caused by aging.

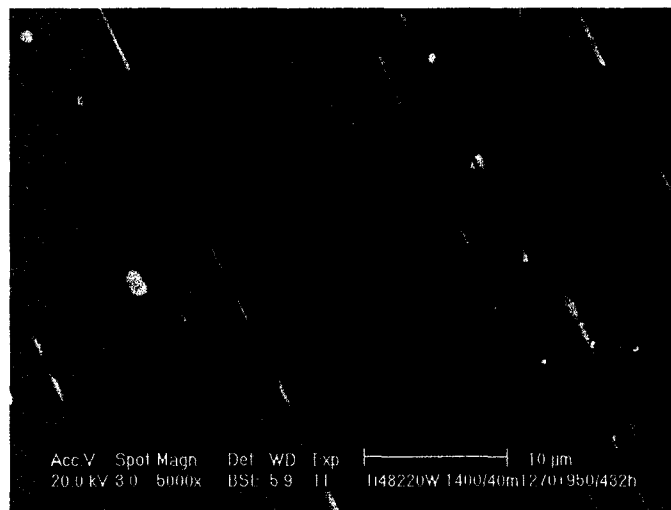
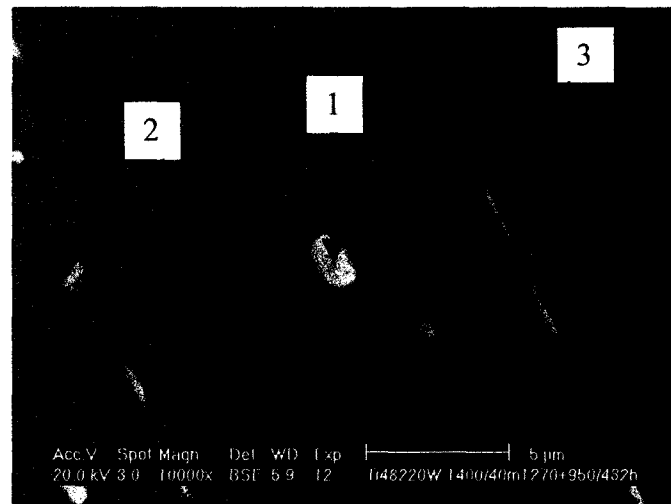


Figure 62 - SEM-BSE micrograph showing the spheroidized α_2 lamellae (arrows) in the 0%W sample after aging for 432 hrs.



Element	Spot		
	1 (α_2)	2 (γ)	3 (γ)
Ti	55.02	45.74	46.18
Al	41.39	49.97	49.57
Cr	1.87	1.99	1.99
Nb	1.72	2.30	2.26

Figure 63 - SEM-EDS results from the 0%W sample after aging for 432 hrs showing the spheroidized α_2 lamellae

Two trends are observed if a comparison is made between the micrographs for the different isothermal aging times in Figure 60 and Figure 61; as the aging time increases, so does the amount of continuous coarsening but as the W content is increased, the amount of continuous coarsening is decreased. In particular, in the case of stepped aging, the microstructures appear to show less coarsening than those isothermally aged for similar times, Figure 64, which seems to agree with work from Zhu et al. [35].

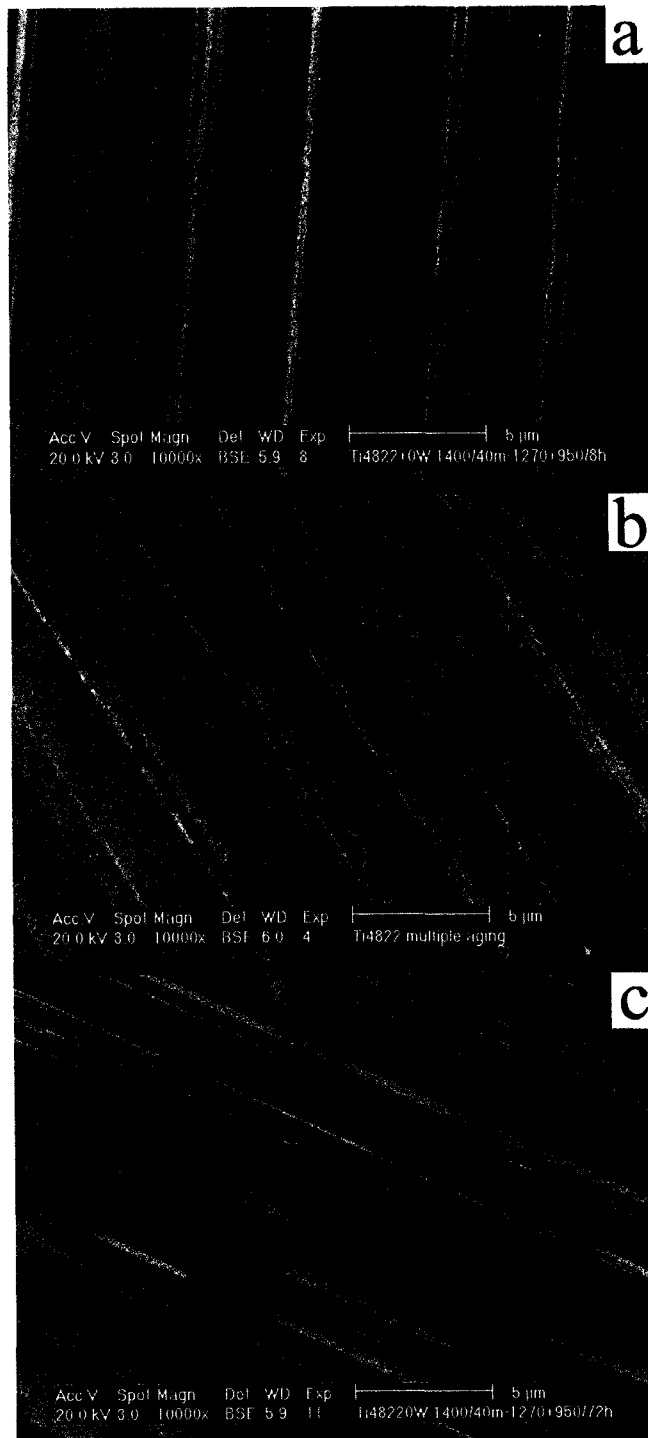


Figure 64 - SEM micrographs of the 0%W alloy after a) isothermal 8 hrs aging, b) stepped aging (~50 hrs) and c) isothermal 72 hrs aging.

Zhu et al. [35] suggested that there are two main modes for dissolution of the α_2 phase, illustrated in Figure 65. The first is longitudinal dissolution which occurs through the motion of a ledge of Shockley partial dislocations along the α_2/γ interface. The second is lateral dissolution which occurs by diffusion across the α_2/γ interface. Longitudinal diffusion is thought to be beneficial since it causes thinning of the α_2 lamellae without causing the lamellae to break up as in lateral dissolution. This means that there are still α_2/γ interfaces inhibiting dislocation motion during deformation.

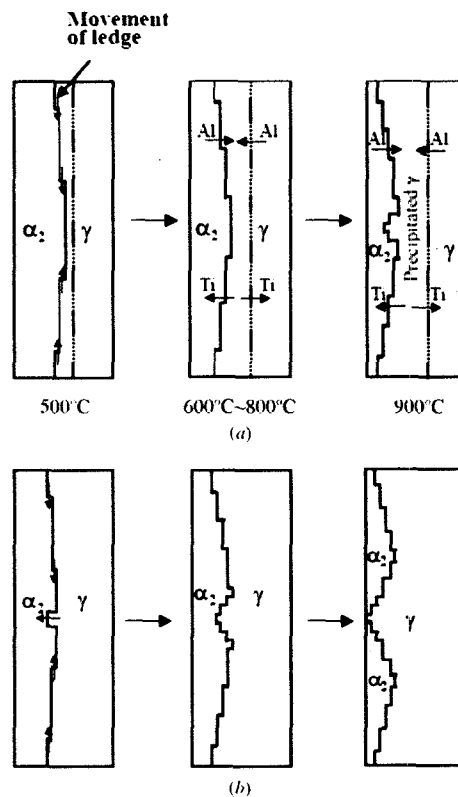


Figure 65 - Illustration of two coarsening modes for γ lamellae under different aging conditions; (a) Longitudinal dissolution (movement of ledges) at lower temperatures changing to lateral dissolution (diffusion across α_2/γ interfaces) at higher temperatures (resembles stepped aging), (b) Lateral dissolution [35]

In addition to the stepped aging minimizing breakup of the α_2 phase, W may also reduced the amount of continuous coarsening. Work from Maziasz et al. [92] has suggested that before dissolution of the α_2 phase can occur, the α_2 lamellae must return to a more stoichiometric composition. However, according to the partitioning coefficients for W, ($k_{\alpha/\gamma} = 1.5$, $k_{\beta/\gamma} = 8$, $k_{\beta/\alpha} = 4$ [53], $k_{\beta/\alpha_2} = 8.82$ [90] in which $k_{\alpha/\gamma} = 1.5$ means there will be 1.5 times as much W in the α phase compared to the γ phase) W will preferentially locate itself in the α_2 phase. Since W diffuses slowly, diffusion across the α_2/γ interface would be slow as well. This would slow the lateral dissolution processes which would increase the length of time required to cause breakup and dissolution of the α_2 phase. In addition to this, by slowing the lateral dissolution processes, more time is given to the longitudinal dissolution process which will not cause the α_2 lamellae to break up.

β precipitates formed at α_2/γ interfaces during aging with the addition of W. Seo et al. has shown that the precipitates grow primarily through diffusion of W from the α_2 lamellae [18]. W also preferentially locates itself within the precipitates as evident by the partitioning coefficients; $k_{\beta/\alpha} = 4$ and $k_{\beta/\alpha_2} = 8.82$ [90], After performing TEM-EDS line scans in the area near precipitates, Figure 66 and Figure 67, the α_2 lamellae was found to be depleted in W and converted to a composition similar to the γ phase.

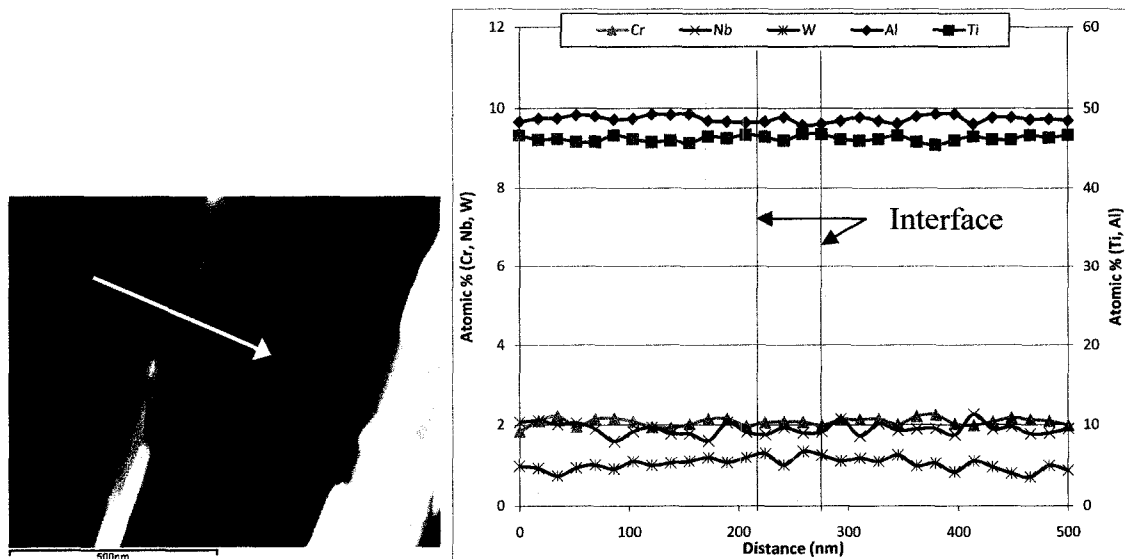


Figure 66 - Line scan across a prior α_2 lamellae in the 1%W alloy after 8 hrs aging

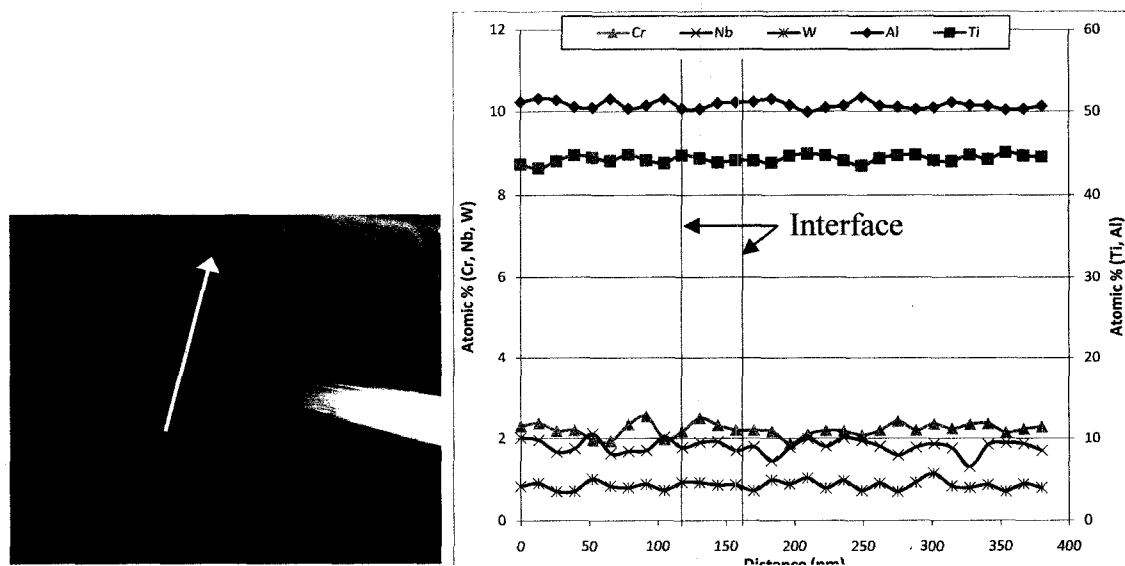


Figure 67 - Line scan across a prior α_2 lamellae in the 1%W alloy after 144 hrs aging

The composition of the lamellae surrounding the precipitates seems to indicate that a transformation from α_2 to γ has likely taken place. This may indicate that the precipitates near the lamellar interfaces could promote α_2 dissolution. However, excessive dissolution

was not observed in the precipitate forming alloys. It is possible that even though W would preferentially locate itself in the β phase, the slow diffusion rate of W at the aging temperatures will not allow easy long range diffusion out of the α_2 lamellae. The precipitates seemed to help pin the γ lamellae and slow the coarsening of γ . As the α_2 lamellae begin to dissolve, the precipitates at the interfaces prohibit easy thickening of the γ lamellae. If complete dissolution of the α_2 phase does occur, however, the precipitates remain at the new γ/γ interface and still interfere with easy dislocation motion.

The stepped aging process seems to promote longitudinal dissolution as well [35]. The diffusion process that governs lateral dissolution is a thermally activated process and therefore requires higher temperatures to occur. The motion of the Shockly partial dislocations will occur at lower temperatures. So as the temperature in the stepped aging process is slowly increased, the Shockly partials begin to move and reduce the free energy in the system. Without a large amount of free energy available to drive the lateral dissolution, the α_2 lamellae are thinned more uniformly and do not show the severe break up found in the isothermally aged samples, Figure 64.

Table 9 and Figure 68 show the average lamellar spacing measured from TEM micrographs with an edge on orientation where the electron beam was parallel to the lamellar interfaces. Two trends are observed if a comparison is made between the different isothermal aging times. Firstly, as the aging time increases so does the amount of continuous coarsening. Secondly as the W content increases, the rate of continuous

coarsening appears to decrease. This is apparent in Figure 68 by the reduced slope of the 1%W line compared to the 0.5%W line. Supposing W helps slow coarsening, then it would seem reasonable to speculate that the 0%W sample would undergo a higher rate of coarsening than the two W containing alloys. SEM micrographs shown in Figure 60 seem to support this by showing α_2 dissolution which results in the coarsening of the lamellar structure in the 0%W alloy. Work from Maziasz et al. [92] on a Ti-47Al-2Cr-2Nb alloy with a FL microstructure appears to be in agreement as well. Maziasz found that aging a FL microstructure with an interlamellar spacing of 100 nm for 4 hrs at 980 °C, increased the spacing to 180 nm. Without W present to help stabilize the 0%W microstructure through reduced diffusion rates and by pinning the lamellae through precipitation at lamellar interfaces, more severe coarsening is expected. Therefore, it is speculated that in the unaged condition, the 0%W alloy is likely to have the thinnest average lamellar thickness compared to the W containing alloys.

Table 9 - Average Lamellar Spacing (nm)

		Aging Time (hrs)		
		8	72	144
Composition	0.0%W	--	164	--
	0.5%W	213	225	347
	1.0%W	187	223	274

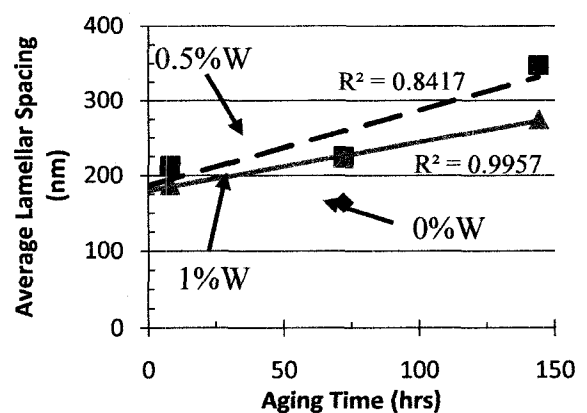


Figure 68 - Relationship between average lamellar spacing and aging time

5.1.3.3 Precipitates

Precipitates formed only in W containing alloys during the aging process. Their size and number increased with both aging time and W content. For example, Figure 69 is a comparison of SEM-BSE micrographs showing that even after 72 hrs aging time, the 0.5%W sample still has fewer precipitates than the 1%W sample after only 8 hrs aging. Therefore, increasing aging time does increase the number of precipitates but the addition of W has a more profound effect. Features resembling precipitates did show up in the 0%W samples after aging for 432 hrs, shown in Figure 62 and Figure 63. As described previously, it is expected they are not a new precipitated phase but are instead spheroidized α_2 . TEM micrographs were also taken within the grains focusing on the lamellar interface areas and precipitates in the W containing alloys, Figure 70.

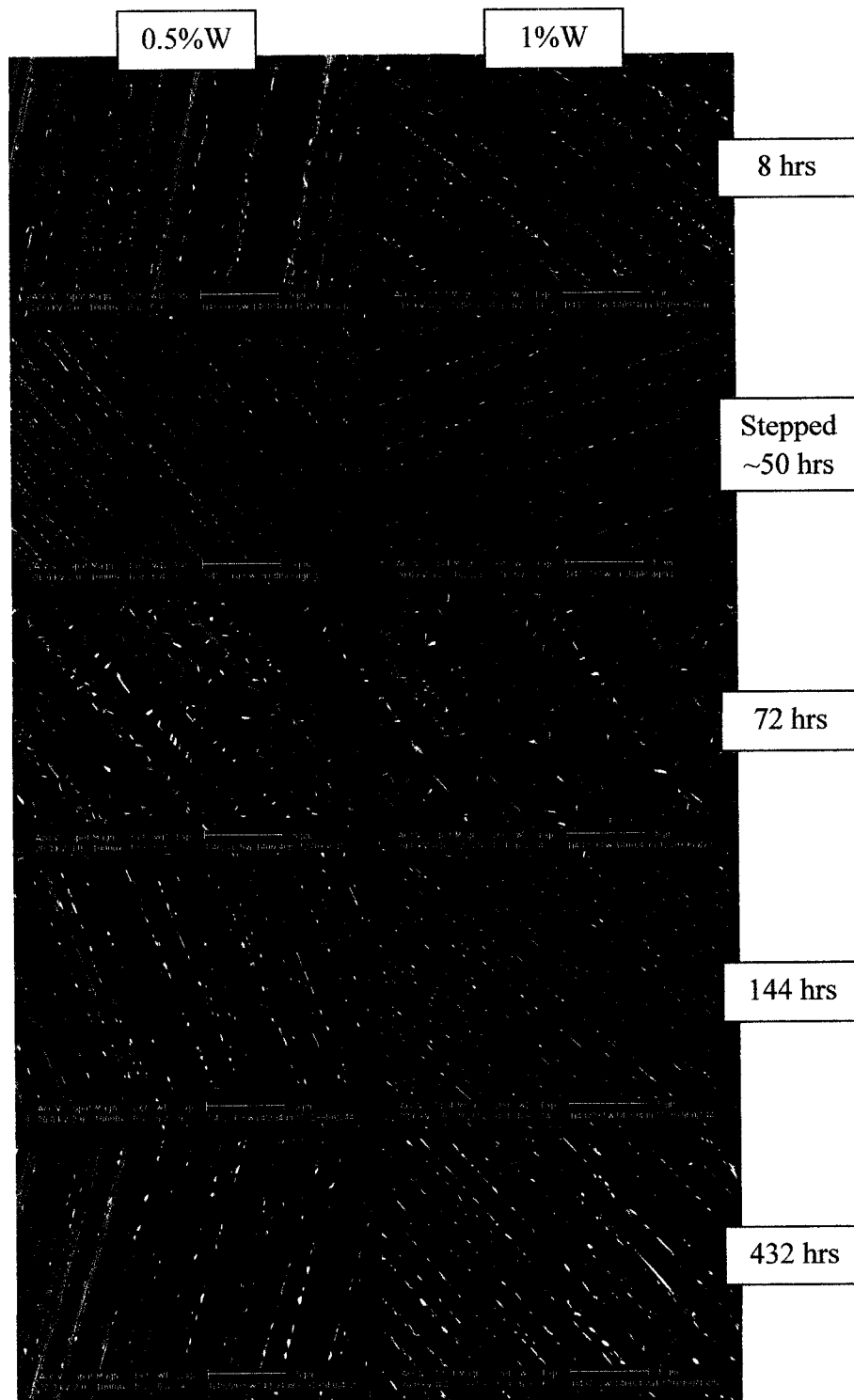


Figure 69 - SEM-BSE micrographs showing precipitate density after aging (All micrographs at the same magnification).

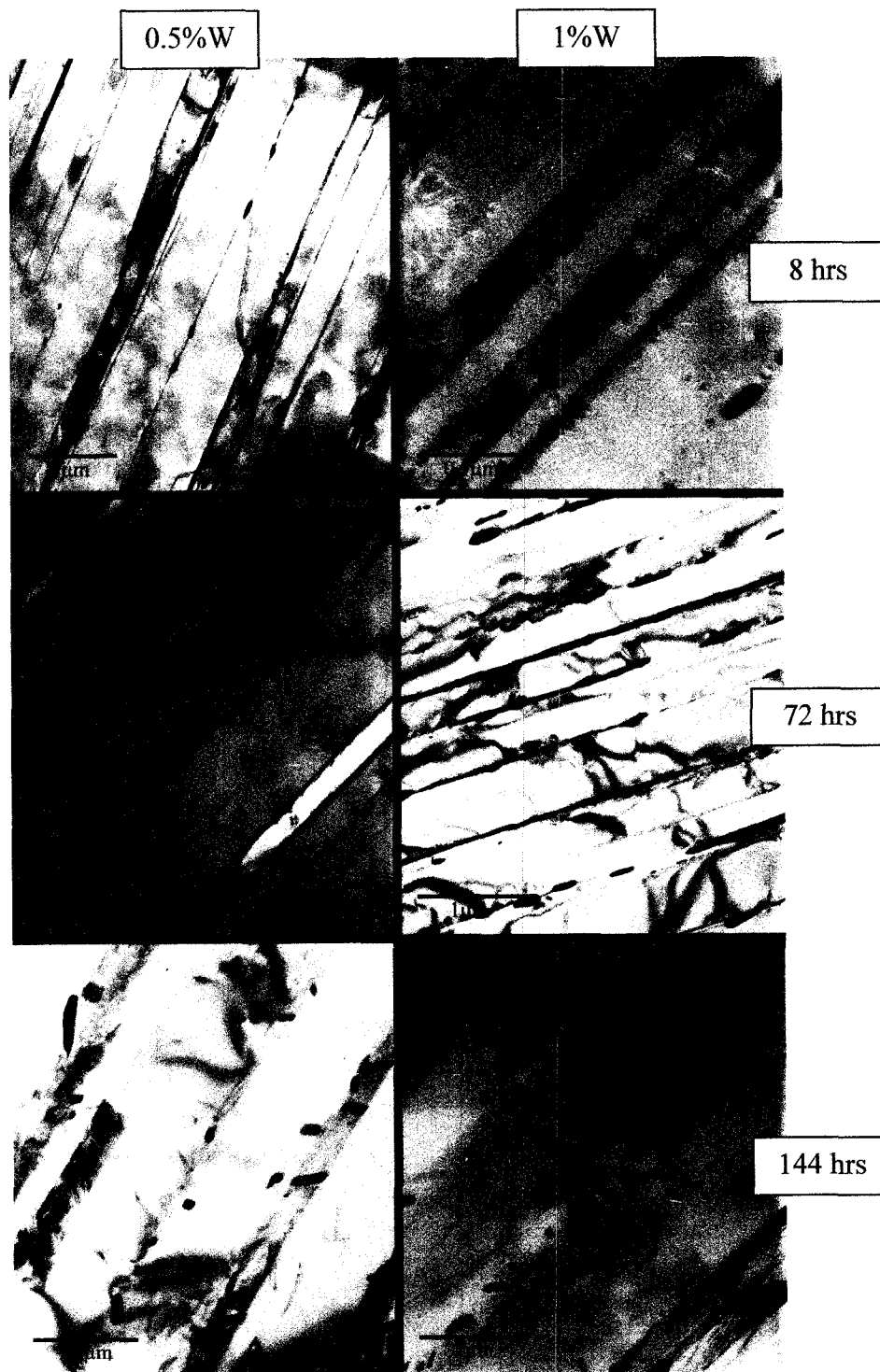


Figure 70 - TEM micrographs from lamellar interfaces showing precipitate formation (Please note the 0.5%W samples aged for 8 and 72 hrs are much closer to an edge on orientation than the others)

TEM analysis indicates that the precipitates found in the W containing alloys nucleated at α_2/γ interfaces and grew at the expense of the α_2 phase (Figure 71) but did not appear to nucleate within the γ lamellae, Figure 70 and Figure 71. Precipitates were often observed at γ/γ interfaces, however, it is believed they did not nucleate at the γ/γ interface but were instead formed at a prior α_2/γ interface. As aging progressed, the α_2 lamellae was dissolved and the surrounding γ lamellae thickened and joined together creating a γ/γ interface in which precipitates were now present. The precipitates were long and needle like in shape when found at γ/γ or α_2/γ interfaces and much larger and more circular when they formed at the grain boundaries, Figure 72.



Figure 71 - Dark field TEM micrograph from the 1%W sample aged for 72 hrs showing precipitates

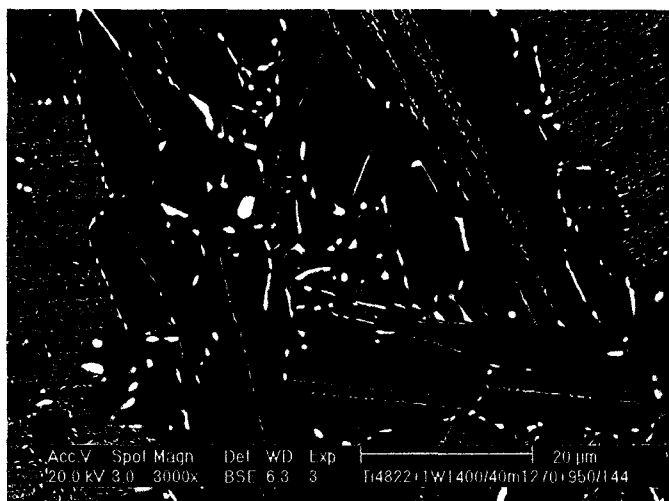


Figure 72 - SEM-BSE micrograph showing the precipitates at the grain boundary (arrows) and lamellar interfaces in a 1%W sample aged for 144 hrs

Smaller precipitates were often found in the 1%W alloy in each of the aging conditions in addition to the larger precipitates, Figure 73 and Figure 74. After long aging times, >144 hrs, smaller precipitates may be found in the 0.5%W alloy as well. It is not obvious in the TEM micrographs if these small precipitates in the 0.5%W alloy are indeed a different morphology. The small precipitates in the 1%W alloy were found only at lamellar interfaces. They had a similar needle like morphology to the large precipitates but were smaller in size. Using the selected area diffraction technique (SAD), it was not possible to obtain a strong enough signal to determine if they were the β phase as well. More detailed research is required to ascertain nucleation and growth mechanisms as well as determining if these precipitates are the β phase.

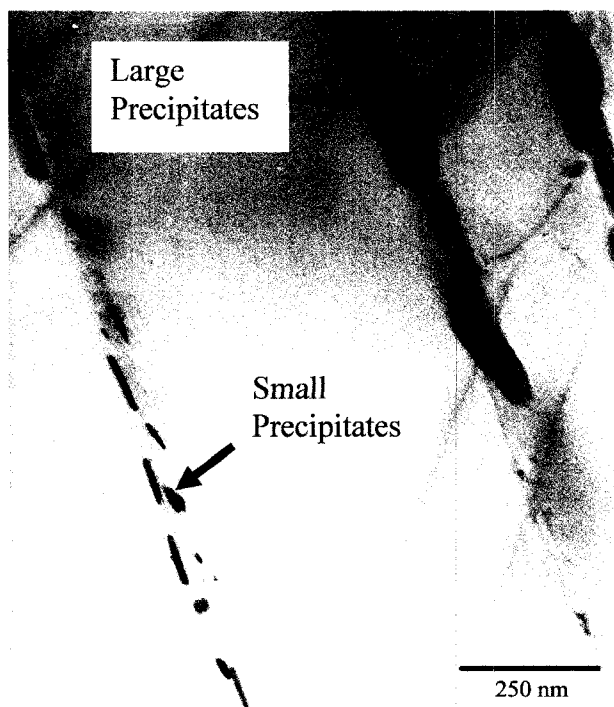


Figure 73 – TEM-BF image showing both the large and small precipitates in the 1%W sample after 72 hrs aging

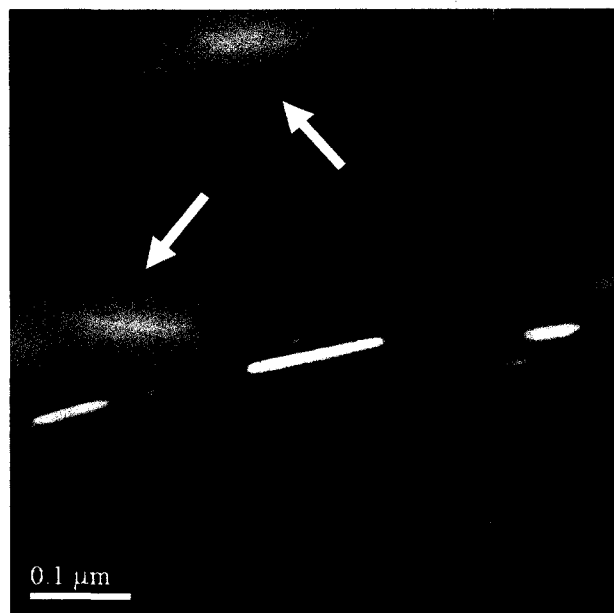


Figure 74 - Angular dark field (ADF) TEM image from the 1%W alloy aged for 72 hrs showing large (arrows) and small precipitates

To examine the effects of precipitate formation on local composition at α_2/γ interfaces, TEM-EDS line scans were conducted at different aging times. The results of the TEM-EDS line scans show an increased concentration of W and Cr near the edges of the γ lamellae compared to the center of the γ lamellae as shown in Figure 75. This likely occurs as a result of the γ formation process. At 1400 °C after ample time has passed to allow complete dissolution of the γ phase (less than 10 min [37]), only the α phase remains. Given enough time, there should not be any local segregation sites for the alloying elements, each grain should have a homogeneous composition. During cooling, when the temperature proceeds below T_{α} , the γ lamellae begin to nucleate and grow into the α grain. During this process, the γ lamellae grow very quickly in the longitudinal direction through the motion of a ledge comprised of a Shockly Partial dislocation. Only limited short range diffusion can take place across this ledge as atoms transfer into the kinks of this ledge [35, 93] and so there is not a large compositional difference immediately following transformation from $\alpha \rightarrow \gamma$. Given time, longer range diffusion across the α/γ interfaces brings the γ phase closer to an equilibrium concentration. As the γ phase thickens and expels alloying elements across the α/γ interface, the concentration in the α phase begins to rise. This makes it more difficult for the γ phase to eject the alloying elements and so a concentration gradient builds up approaching the interface in both the γ and α phases. Since this is occurring during cooling, diffusion becomes more difficult as the temperature continues to decrease. Once at room temperature, the edges of

the γ lamellae (near the α_2/γ interfaces) are further away from the equilibrium composition than the center.

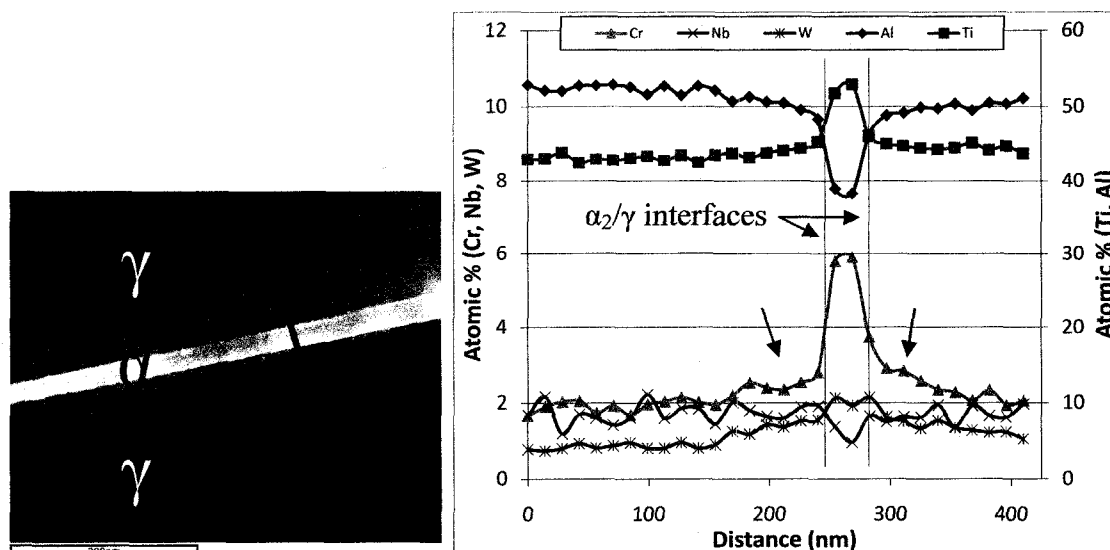


Figure 75 - TEM-EDS line scan results from the 1%W alloy after the SCHT. Arrows indicate increased W and Cr concentrations near the α_2/γ interfaces.

Subsequent aging allows the thermally activated diffusion process to resume. The edges of the γ lamellae are able to reject the excess alloying elements to form precipitates at the α_2/γ interfaces. The precipitates have a much higher partitioning coefficient ($k_{\beta/\alpha_2} = 8.82$ and $k_{\beta/\gamma} = 12.85$ for W and $k_{\beta/\alpha_2} = 3.09$ and $k_{\beta/\gamma} = 4.48$ for Cr [90]) and readily absorb alloying elements from the surrounding area, both from α_2 and γ phases. Figure 76 shows that the area of the γ phase near the γ/β interface is no longer rich in W or Cr compared to the center of the lamellae due to the formation of the β precipitate. Further aging allows for additional diffusion and shows that a small deficit of W and Cr is now present in the γ lamellae near the γ/β interface as the precipitates grow, Figure 77.

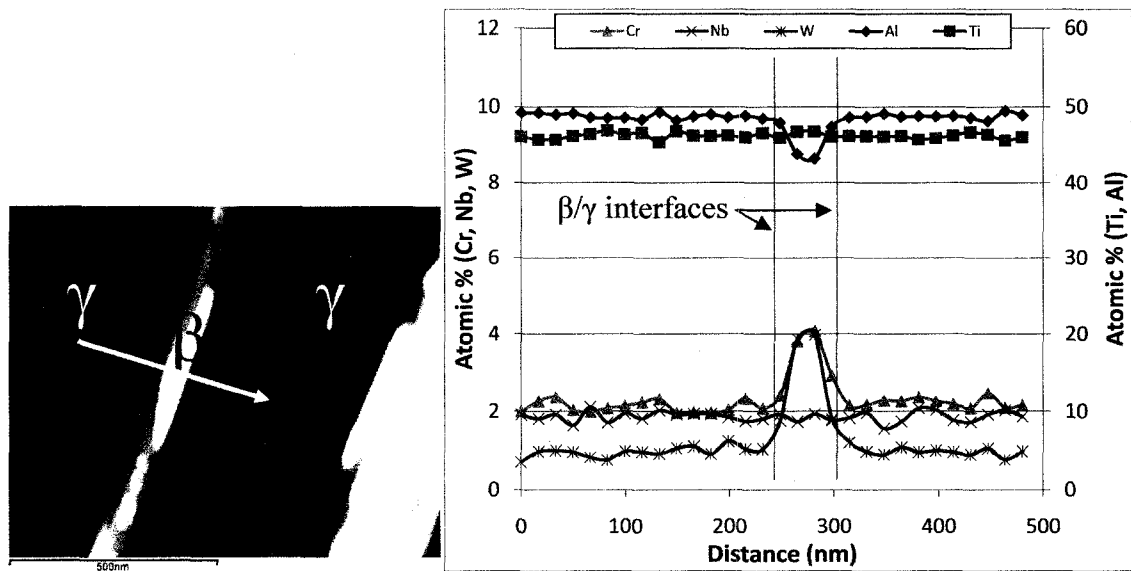


Figure 76 - TEM-EDS line scan results of the 1%W sample following the SCHT + 8 hrs aging. Line scan is across a precipitate.

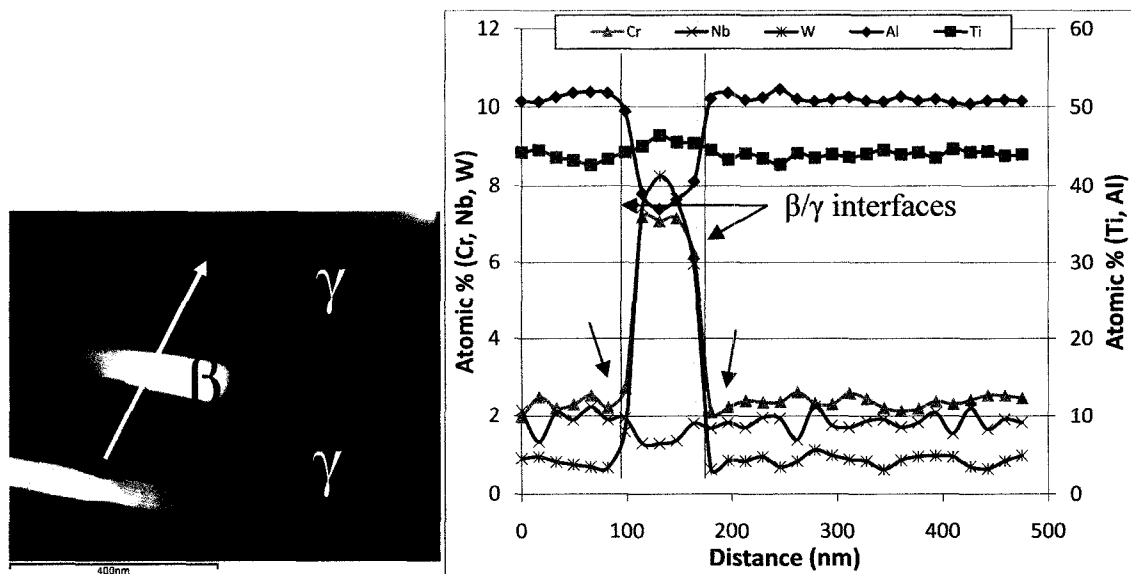


Figure 77 - TEM-EDS line scan results of the 1%W sample following the SCHT + 144 hrs aging. Line scan is across a precipitate. Arrows indicate a small deficit in W and Cr near the β/γ interfaces

The composition of the large and small precipitates in the 1%W alloy and the precipitates in the 0.5%W alloy were examined using both SEM and TEM-EDS techniques. It is noted that TEM-EDS gives better resolution in term of quantitative analysis due to the smaller activation volume from the surrounding area caused by the electron beam and sample interaction. The results from both EDS analysis are shown in Tables 10 - 13.

Table 10 - TEM-EDS results from point scans on small precipitates at the lamellar interfaces on the 1%W alloy

Element (at.%)	Aging Time (hrs)			
	0	8	72	144
Ti	--	45.4	41.7	--
Al	--	45.2	40.2	--
Cr	--	2.9	3.4	--
Nb	--	1.9	1.9	--
W	--	4.7	12.8	--

Table 11 - TEM-EDS results from point scans on large precipitates at the lamellar interfaces on the 1%W alloy

Element (at.%)	Aging Time (hrs)			
	0	8	72	144
Ti	--	46.7	45.9	45.7
Al	--	43.4	38.3	36.6
Cr	--	4.0	6.6	7.4
Nb	--	1.7	1.2	1.4
W	--	4.2	7.5	9.0

Table 12 - SEM-EDS results from point scans on large precipitates at the lamellar interfaces on the 1%W alloy

Element (at.%)	Aging Time (hrs)				
	0	8	72	144	432
Ti	--	46.6	43.6	44.1	45.0
Al	--	46.7	49.3	50.0	48.0
Cr	--	3.1	2.5	2.1	2.6
Nb	--	1.6	2.3	2.3	2.2
W	--	1.9	2.2	1.6	2.2

Table 13 - SEM-EDS results from point scans on large precipitates at the lamellar interfaces on the 0.5%W alloy

Element (at.%)	Aging Time (hrs)		
	0	144	432
Ti	--	45.5	44.5
Al	--	47.7	49.3
Cr	--	2.9	2.8
Nb	--	1.9	2.0
W	--	2.0	1.4

A comparison between the two methods, TEM-EDS in Table 11 and SEM-EDS in Table 12, for determination of the large precipitate composition reveals that the SEM and TEM results differ. This is due to the size of the area each method receives X-rays from. The SEM generates a larger spot size on the sample and as such, a larger area is excited (Figure 78) and produces X-rays which the EDS uses to generate compositional data. TEM-EDS excites a much smaller area within the sample. It seems likely that due to the precipitate size, the SEM-EDS results are including X-rays generated from the surrounding matrix. The TEM-EDS results are expected to more accurately reflect the

real composition of the precipitates because less of the surrounding matrix will be excited.

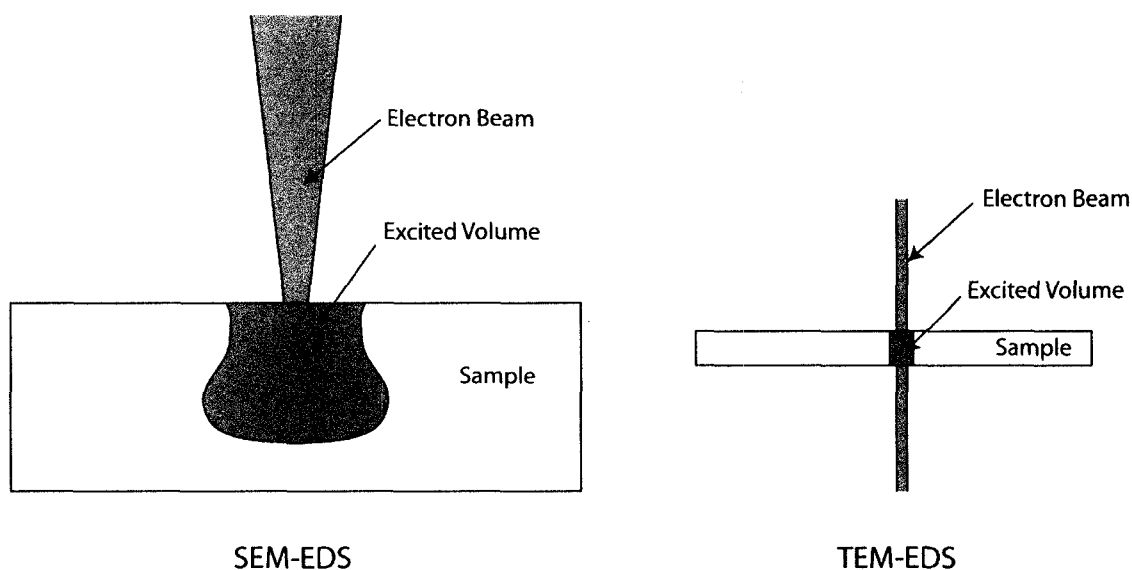


Figure 78 - Excited volumes from SEM and TEM-EDS analysis

TEM-EDS results for the large precipitates (Table 11) indicate that with aging time, the precipitates continue to increase in W and Cr. Correlating this with the TEM-EDS line scans across the lamellar interfaces, it seems likely that the precipitates are the destination of the excess W and Cr near the lamellar interfaces in the SCHAT condition. If the data from Table 11 are plotted with aging time using a logarithmic scale in Figure 79, it shows that the diffusion of W and Cr into the precipitates follows closely a logarithmic increase in concentrations with aging time (typical of diffusion controlled processes). The two equations presented on the plot in Figure 79 predict W and Cr concentrations over the given aging times.

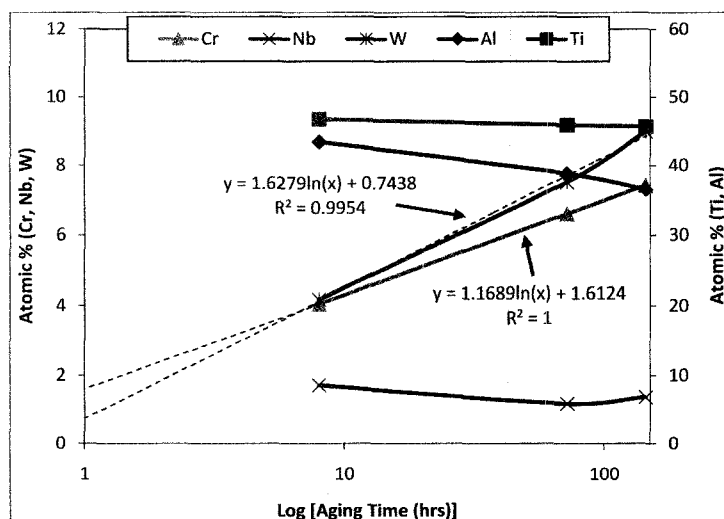


Figure 79 - Logarithmic plot of data presented in Table 11

Comparing the composition of the large and small precipitates found in the 1%W alloy (Table 11 and Table 10, respectively) to the surrounding matrix, some observations stand out. Aging for 8 hrs shows the small precipitate has a composition which is also high in W and Cr with less Al than the surrounding γ lamellae which is similar to the larger precipitates. Ti and Nb remain fairly constant. However, aging for 72 hrs causes the Ti and Al content of the smaller precipitates to drop and the W content to increase dramatically as shown in Table 10. Cr shows a comparatively small increase and Nb continues to remain unchanged.

To contrast with the large precipitates, the smaller precipitates seem to increase in W at a much faster rate during aging. The smaller precipitates have substantially more W after aging for 72 hrs. However, the Cr content in the smaller precipitates is less compared to the large precipitate after 72 hrs aging and does not increase as rapidly as in the larger precipitates. Nb content appears to be similar in each of the precipitate types

but the Al content is higher in the smaller precipitates although it is still less than the surrounding matrix. Ti is also much lower in the smaller precipitates, likely as a way to accommodate the increased W content.

Precipitate size and density is typically governed by the aging temperature and duration [50, 94]. For example, at lower aging temperatures, the critical nucleation radius is smaller and nucleation rates are increased [94] so smaller and more numerous precipitates are formed at lower aging temperatures with longer aging times. Conversely, higher aging temperatures increase diffusion rates as well as the critical nucleation radius so large precipitates form at increased intervals compared to lower aging temperatures. In this study, each of the isothermal aging treatments was performed at 950 °C. The stepped aging did start at lower temperatures and progress to 950 °C as a final temperature (identical to the isothermal aging temperature). Therefore, it might seem that the stepped aged samples should show more of the smaller precipitates. The SEM micrographs shown in Figure 80 appear to support this.



Figure 80 - Comparison of 1%W samples. Top - Stepped aging. Bottom - Aged 72 hrs

It is odd that the small precipitates were found only in the 1%W alloys and not in the 0.5%W. This makes it seem that the smaller precipitate morphology is influenced by W content. If this line of thought is extended, then it would seem logical to assume that additional W (i.e. Increasing W from 1% to 2%) should increase the amount of small precipitates. This, however, is not the case. There are numerous studies on a Ti-48Al-2W ternary alloy which also has a FL microstructure with β phase precipitates at the lamellar interfaces [17]. Isothermal aging times and temperature are also identical to those used in this study. None of the smaller precipitates were observed at the lamellar interfaces

though, making it seem as though simply adding W will not form the small precipitates. One important thing to note is that the alloys currently being investigated, contain two additional alloying elements, Cr and Nb. It is possible that there is some interaction between Cr and W which cause the smaller precipitates to form.

Additionally, the smaller precipitates do not seem to form adjacent to larger precipitates. If an α_2/γ interface is already occupied with one type of precipitate, then any new precipitates which nucleate tend to be the same type as shown in Figure 81. In some instances (arrows in Figure 81) small precipitates were found on interfaces occupied by larger interfaces. The small precipitates did not form near the large precipitates but instead formed some distance down the interface away from the large precipitates. This likely occurs because once the large precipitates nucleate and begin to grow, they create a deficit of the alloying elements required to form the smaller precipitates. More research is required to accurately determine the nucleation mechanism as well as the morphology of these smaller precipitates.

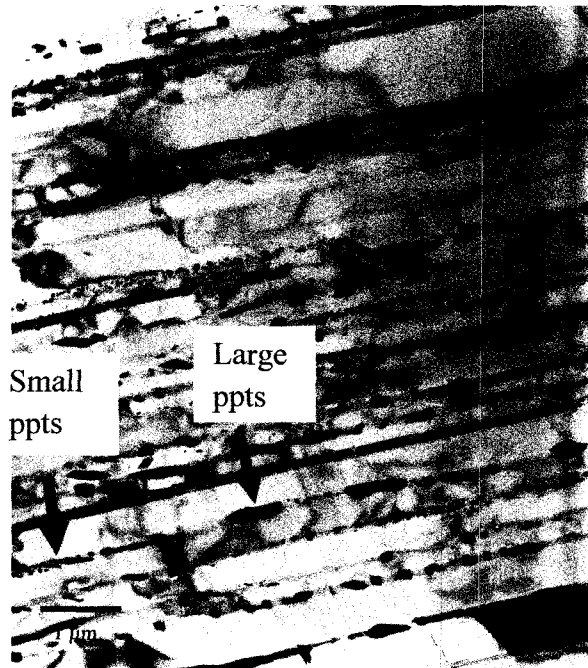


Figure 81 - TEM-BF micrograph showing the lamellar region of a 1%W alloy aged for 72 hrs which contains both large and small precipitates. Arrows indicate a rare instance of the small and large precipitates on the same lamellar interface.

5.2 Micro-Hardness Data

Micro-hardness tests were performed to evaluate mechanical properties of the alloys with respect to aging time and W content. Micro-hardness testing was carried out only within FL grains to avoid any GB effects. Creep and tensile tests for selected aging conditions were performed based on data determined from micro-hardness results and metallographic analysis.

The micro-hardness trend with respect to aging time for the three compositions closely resembles each other, Figure 82 and Figure 83. In the unaged conditions, the 0.0%W and 1.0%W samples have similar hardness while the 0.5%W sample is lower. After aging for 8 hrs, both the 0%W and 0.5%W samples softened but the 1%W sample

did not. The next aging interval from 8 hrs to 72 hrs shows that both samples containing W had a similar rate of softening while the 0%W sample softened considerably. Further aging to 144 hrs shows all three samples hardening at similar rates. Additional aging to 432 hrs resulted in the reduction of hardness in the samples containing W but a slight increase of hardness in the 0%W sample.

The stepped aged sample containing 1%W showed an increased micro-hardness when compared to the unaged sample with 1%W content. The opposite effect was observed in the 0.5%W and 0%W samples where stepped aging produced a reduction in micro-hardness values when compared to the unaged conditions. The 0%W alloy, however, showed a more drastic reduction in micro-hardness.

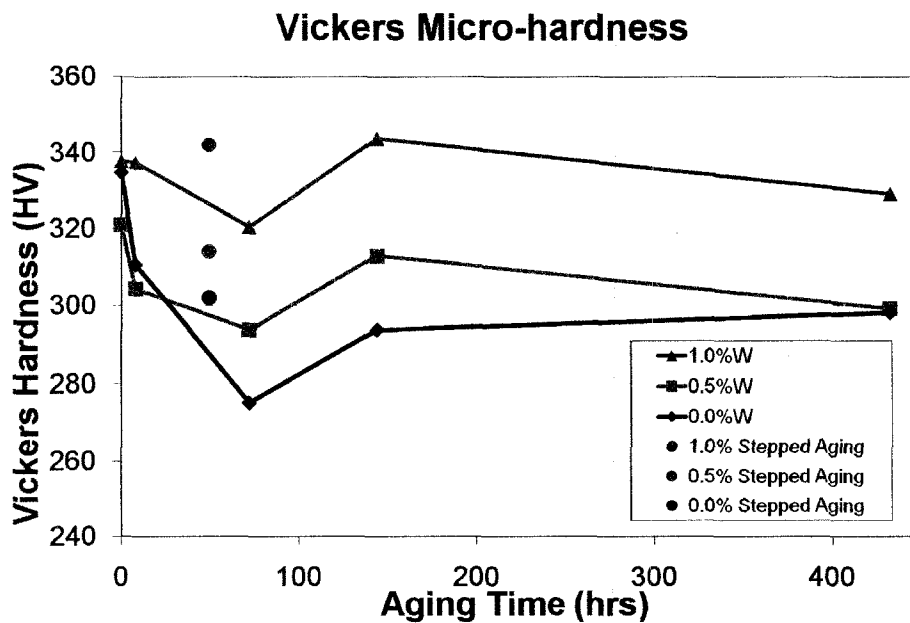


Figure 82 - Vickers micro-hardness test results against aging time

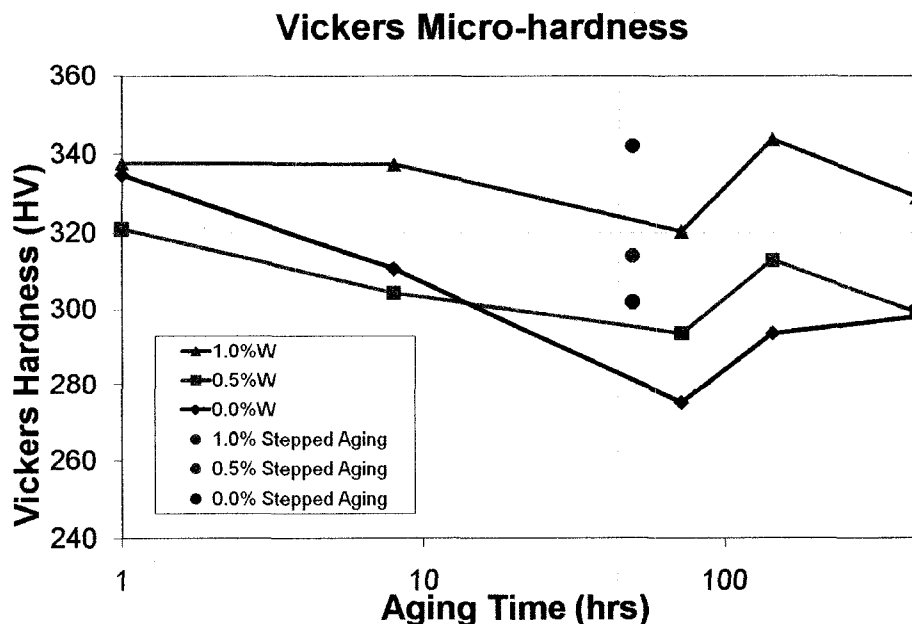


Figure 83 - Vickers micro-hardness test results against log aging time

In the unaged condition, it seems counter intuitive to find the 0%W and 1%W samples with similar hardness values while the 0.5%W sample is lower. Even though the benefits discussed earlier from W additions (precipitation, reduced coarsening, etc.) do not apply in the unaged condition, W strengthens the γ lamellae through a solid solution strengthening mechanism [21]. It would, therefore, seem more reasonable to see the 0%W, 0.5%W and 1%W samples with increasing hardness values in the order written. It is possible that this discrepancy is a result of differences in lamellar spacing as shown in Table 9 and Figure 68. Although measurements for lamellar spacing in the unaged condition were not made, it would be reasonable to speculate that the 0%W sample in the unaged condition would have the thinnest lamellar spacing compared to those of the 0.5%W and 1%W also in the unaged condition. The argument for this speculation has

already been presented in section 5.1.3.2. In addition, it is recalled the Hall-Petch type relationship between lamellar spacing and yield strength (Equation 2). Therefore, it is speculated that in the unaged condition, the hardness of the 0%W sample would be similar to the 1%W sample due to differences in lamellar spacing.

The initial drop in hardness of the 0%W and 0.5%W samples after 8 hrs aging is believed to be caused by the degradation of the lamellar microstructure (lamellar coarsening) which was discussed in Section 5.1.2.2. The 1%W addition seems to minimize the hardness drop by inhibiting the degradation of the lamellar microstructure and the formation of interfacial precipitates. However, increasing aging time to 72 hrs shows a further reduction in hardness in all three cases. The rate of the reduction is reduced in the samples containing W. The hardness is still reduced by aging to 72 hrs due to the continuing degradation of the lamellar structure. The rate of degradation in the 0%W alloy slows, however, because during the initial aging period, degradation proceeds rapidly since the α_2 volume fraction is far from equilibrium. As the γ lamellae thicken and slowly approach a more equilibrium volume fraction, the driving force behind the microstructural degradation processes decreases. The W containing samples undergo a similar process but the precipitates also multiply and grow, which could counteract the hardness loss. It is difficult to distinguish between the microstructural degradation and precipitate formation as they are both competing mechanisms which occur simultaneously during aging. Further aging to 144 hrs shows an increase in hardness values. This is speculated to be caused from precipitation strengthening in the samples

containing W. Precipitates are present in both the 8 hrs and 72 hr aged samples as well but it is believed that these shortened aging times do not produce precipitates which are large enough or numerous enough to overcome the softening caused by coarsening. Interestingly enough, the tensile and creep tests both seem to benefit from the shorter aging times as will be discussed in the following sections. In the 0%W sample, however, solid solution strengthening caused by Cr diffusing into the γ lamellae as the α_2 lamellae decompose may be the cause of the improved hardness. Partitioning coefficients for Cr measured at different temperatures show that once ordering of the α phase occurs, Cr is not as strongly attracted to the α phase [90]. At 1300 °C, $K_{\alpha/\gamma} = 2.00$ while at 1000 °C after ordering, $K_{\alpha_2/\gamma} = 1.45$. So it is possible that since the samples were air cooled from 1270 °C, that the α_2 phase is supersaturated with Cr. As aging progresses, the excess Cr is able to diffuse back into the γ phase. Cr has also been shown to strengthen the γ phase [5]. In addition to this, work from Maziasz et al. [92] has suggested that before the α_2 phase is able to transform into the γ phase, it must first progress to a more stoichiometric composition (i.e. it must reject any alloying elements to the surrounding area). This means that Cr will be rejected from the α_2 lamellae and forced into the surrounding γ lamellae. It is speculated that the solid solution strengthening from the Cr diffusing into the γ lamellae overcomes the loss in hardness due to the α_2 dissolution.

Further aging up to 432 hrs causes another small reduction in hardness in samples containing W while it shows a slight increase in hardness for the sample containing no W. The slight hardness increase in the 0%W sample is likely within the error range of the

micro-hardness tester and therefore negligible. It is possible that the hardness reduction in the W samples is caused by something similar to over aging as seen in an Al-Cu system in addition to the continued degradation of the FL microstructure. In the Al-Cu system, aging for long times causes the fine GP2 zones to dissolve and the θ' precipitates to grow in size creating a microstructure with larger more spaced out precipitates [50]. In the W containing alloys, there doesn't seem to be any dissolution of a second phase but it is possible the precipitates within those alloys grow beyond an ideal size and distribution to effectively block dislocation motion.

In the stepped aged condition, samples showed relatively high hardness compared to the isothermally aged samples for similar aging times as shown in Figure 82 and Figure 83. In the W containing samples, this can be attributed to the reduced amount of lamellar coarsening coupled with the precipitation of the β phase at the lamellar interfaces. As discussed in section 5.1.3.2, the stepped aging process is able to reduce the α_2 volume fraction while avoiding severe breakup of the lamellae. Longitudinal dissolution of the α_2 lamellae thins the lamellae while still maintaining α_2/γ interfaces. In the sample without W, no precipitates were formed so it is speculated that the increased hardness compared to the isothermally aged samples is due to the reduced amount of continuous coarsening observed, thereby maintaining the α_2/γ interfaces, Figure 64.

To summarize, the lamellar micro-hardness values in the W containing samples show a reduction in hardness to the minimum micro-hardness value after 72 hrs aging followed by the maximum at 144 hrs aging and then a subsequent reduction again. The change in

hardness values across the aging times are likely caused by two competing mechanisms occurring at different rates, lamellar coarsening and precipitate formation. The initial drop occurs as the lamellar microstructure begins to coarsen and W and Cr are diffusing out of lamellae into precipitates. Once the precipitate size and number increase enough to effectively block dislocation motion and emission (as discussed in section 2.1.3.3), hardness values increase again to their maximum at 144 hrs. Further aging likely causes an over aging effect where precipitate size may increase and precipitate number may decrease beyond ideal values causing hardness to decrease.

The 0%W sample shows a similar trend with hardness values, a minimum is obtained after 72 hrs aging, however, further aging continues to increase the hardness up to 432 hrs and possibly further at longer aging times. The initial drop as aging proceeds to 72 hrs is likely caused by the same mechanism found in the W containing samples, lamellar coarsening due to α_2 dissolution. Beyond 72 hrs, however, there is no precipitation so another strengthening mechanism must be present. It was proposed that as the α_2 lamellae decompose, the Cr which was partitioned in the α_2 lamellae is rejected back into the γ lamellae to strengthen it. So once a critical amount of α_2 has been decomposed, the Cr strengthened γ lamellae are more capable of restricting dislocation motion.

Stepped aging the samples produced hardness values similar to unaged conditions when W was present. This is likely a consequence of reduced coarsening as a result of the stepped aging process. In the case of the 0%W sample, hardness decreased compared to the unaged condition, however, it was still higher than the isothermal aged condition.

This is believed to be a result of the reduction of lamellar breakup in the stepped aged condition compared to the isothermal aged condition.

5.3 Mechanical Testing

5.3.1 Creep Testing

Creep tests were conducted on the three different compositions in four different aging conditions, unaged, stepped aged, 8 and 144 hrs isothermally aged. Aging times were selected based on favourable micro-hardness data or conditions that exhibited limited degradation of the microstructure. The unaged condition was chosen to serve as a baseline for the results and see what impact aging has on creep results. Stepped aging had very promising micro-hardness values and also showed limited microstructural degradation. The 8 hrs aged condition was selected due to its limited microstructural degradation as well as adequate micro-hardness results. 144 hrs isothermal aging produced a high hardness, however, it also showed more severe microstructural degradation. The results from the creep tests have been plotted in a number of figures (Figure 84 - 93). They are organised in such a way as to try and make the large number of curves and different material conditions manageable. Figure 84 - Figure 86 contain the entire collection of creep curves and illustrate the complete creep life, primary region and the instantaneous regions respectively. Figure 87 - Figure 93 then isolate the creep curves either by composition or by aging time.

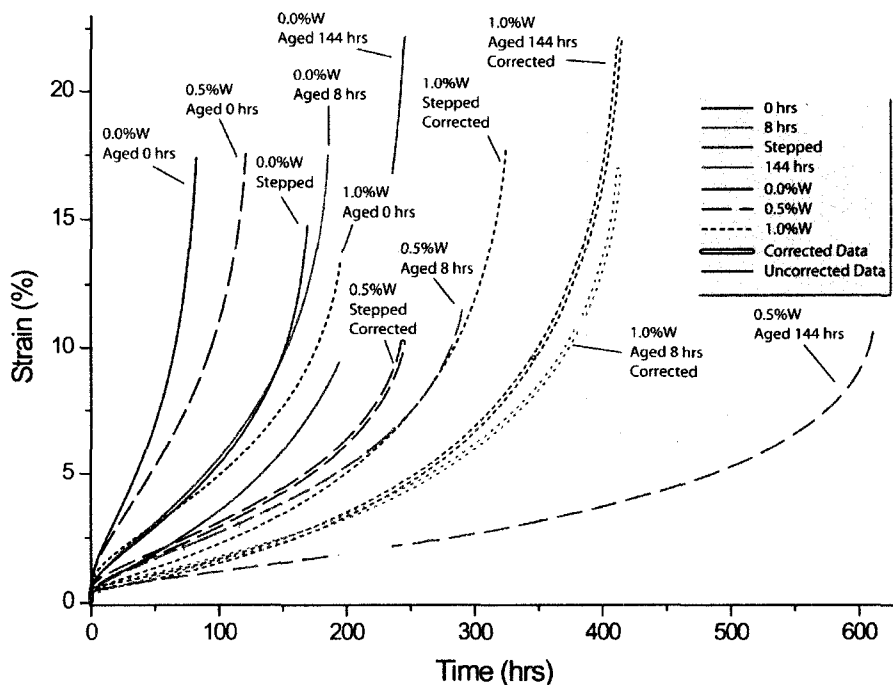


Figure 84 - Constant load creep curves generated by testing samples at 760 °C and 276 MPa

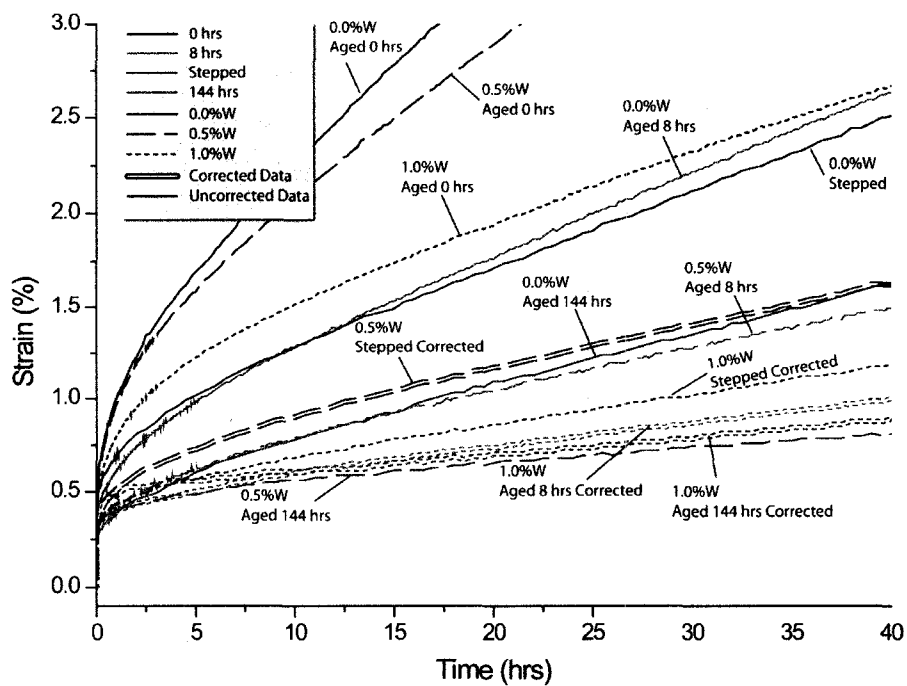


Figure 85 - Constant load creep curves generated by testing samples at 760 °C and 276 MPa (0 – 40 hrs)

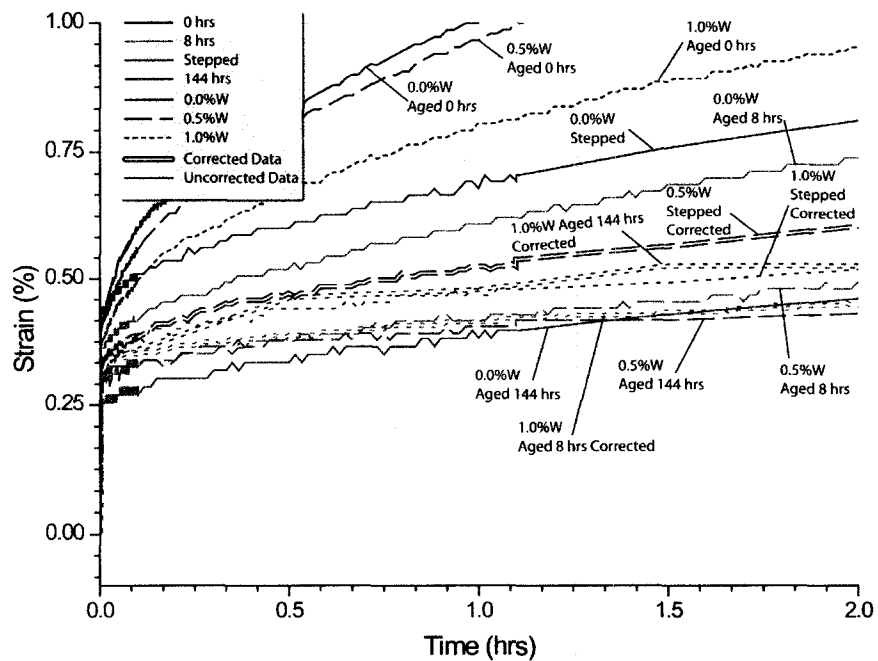


Figure 86 - Constant load creep curves generated by testing samples at 760 °C with a 276 MPa load (0 – 2 hrs)

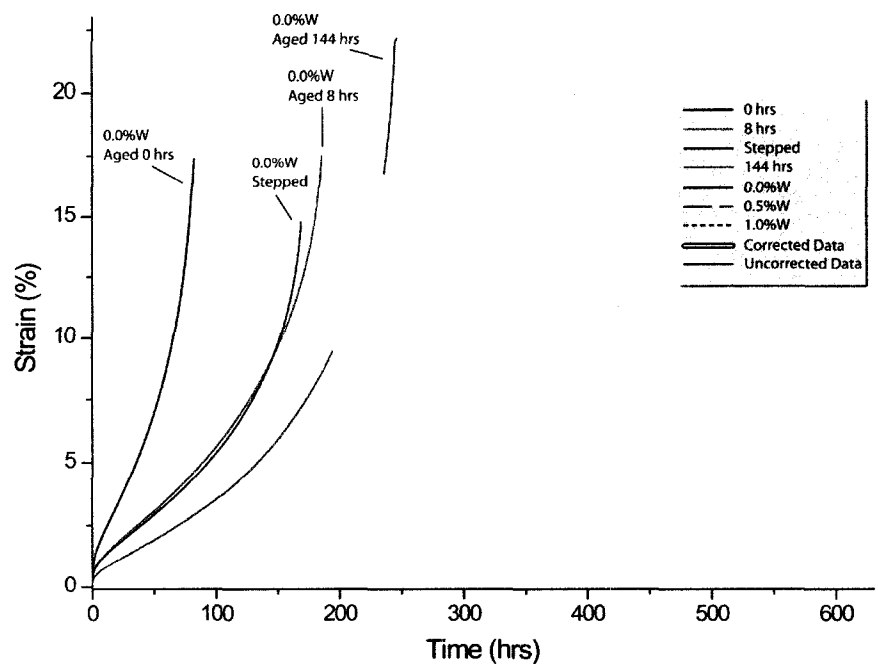


Figure 87 - Creep curves of 0%W alloys with different aging conditions (760 °C and 276 MPa load)

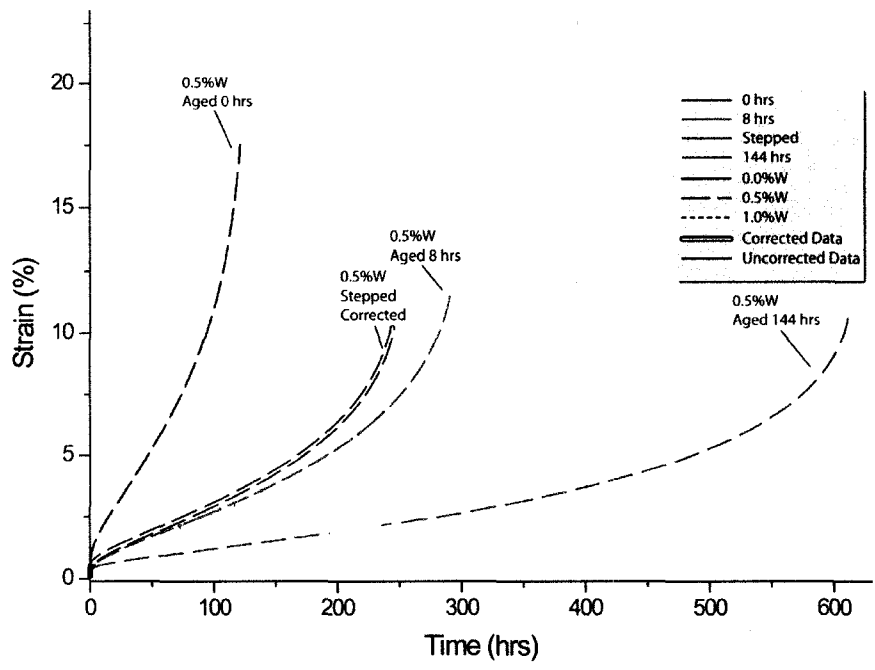


Figure 88 - Creep curves of 0.5%W alloys with different aging conditions (760 °C and 276 MPa load)

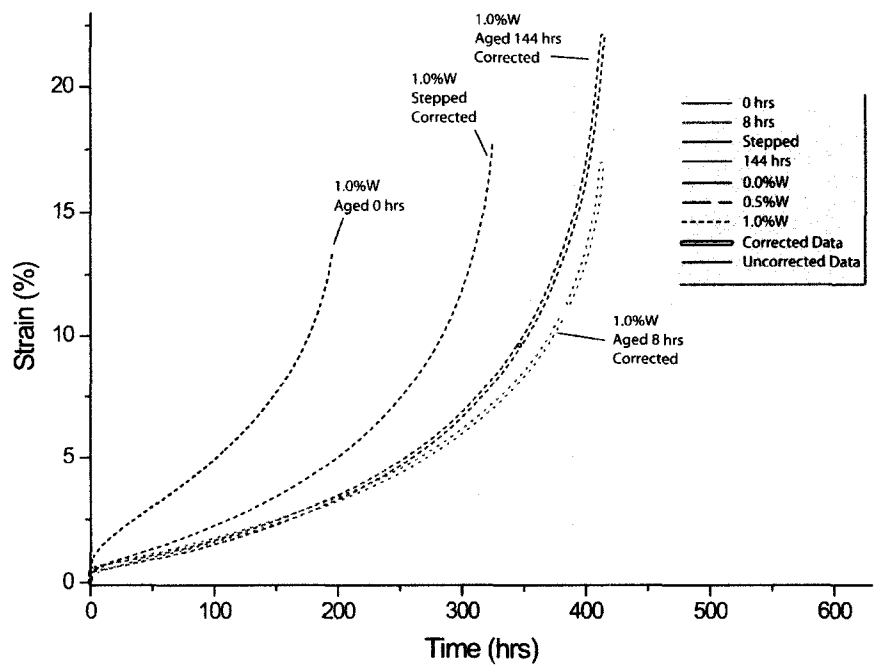


Figure 89 - Creep curves of 1%W alloys with different aging conditions (760 °C and 276 MPa load)

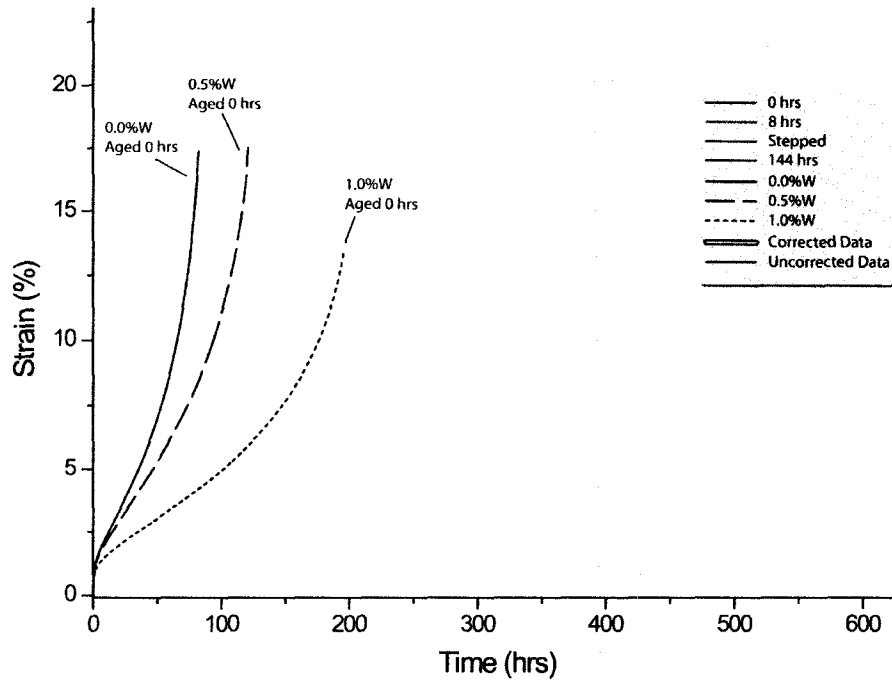


Figure 90 - Creep curves of the alloys in the unaged condition (760 °C and 276 MPa load)

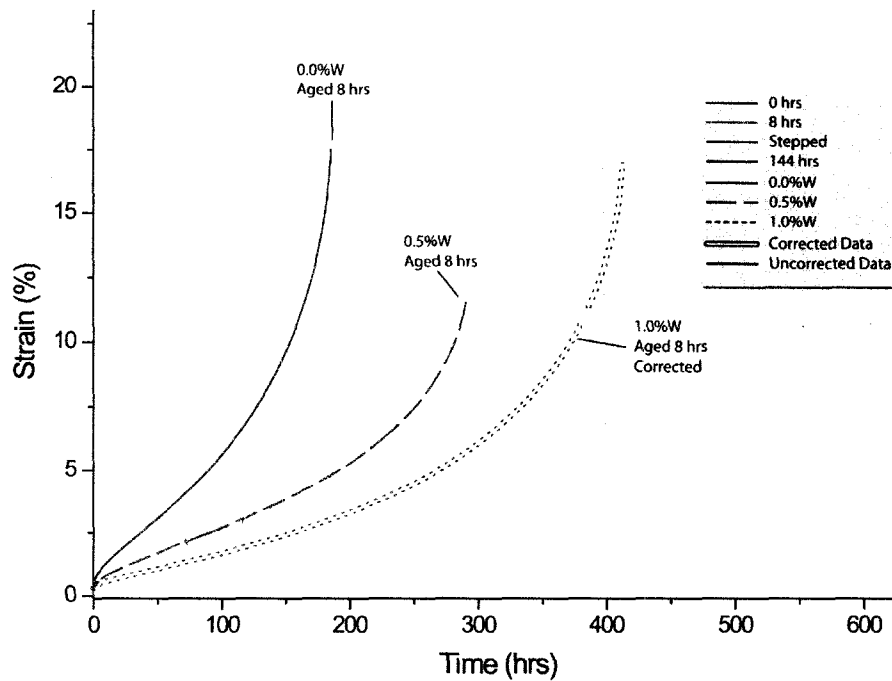


Figure 91 - Creep curves of the alloys after 8 hrs isothermal aging (760 °C and 276 MPa load)

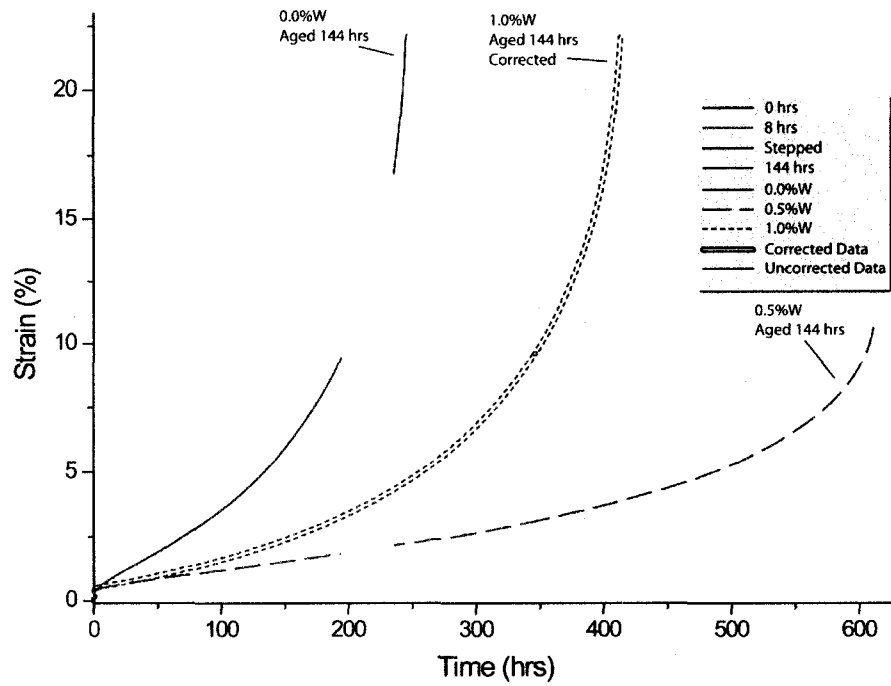


Figure 92 - Creep curves of the alloys after 144 hrs isothermal aging (760 °C and 276 MPa load)

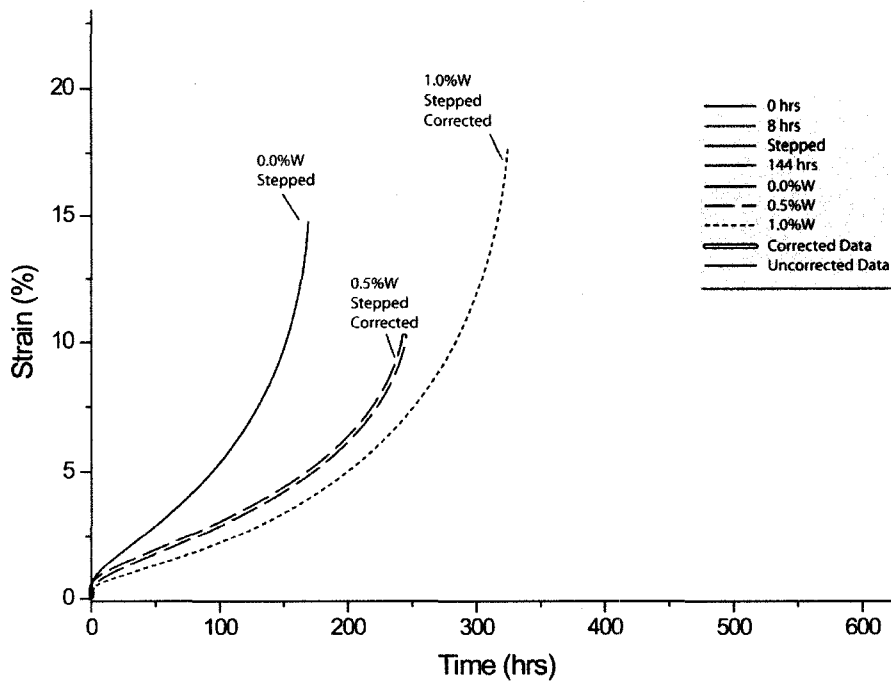


Figure 93 - Creep curves of the alloys after stepped aging (760 °C and 276 MPa load)

It is apparent in the 0.0%W aged for 144 hrs creep curve that some of the data is missing (Figure 92). The missing data was caused by a malfunction with the data acquisition system (DAQ). When the malfunction was discovered, the system was restarted and normal recording was resumed. During the malfunction with the DAQ, there was no interruption to either the load or the furnace temperature.

In addition to the inconvenience with the DAQ, a few other tests had difficulty with the extensometer or load train. The most obvious case was with the 1%W sample, aged for 144 hrs. It appears that the extensometer or the load train became wedged at the beginning of the tests. The strain rapidly increased to about 0.22% and then only slowly increased to 0.25% strain over 38 hrs. After 38 hrs, the strain rapidly increases again and starts to level out which bears resemblance to the primary strain regime of typical TiAl creep curves. The strain profile would suggest that the load train was jammed for some reason and no load was applied to the sample for roughly 38 hrs. If this is the case, then approximately 38 hrs should be removed from the creep curve for the 1.0%W sample aged for 144 hrs. On the other hand, if the extensometer was stuck and not the load train, then the specimen would still be creeping even though the extensometer was not properly recording the strain. The strain profile when the extensometer began recording normal strain rates again, resembles the primary creep regime. This suggests that the load train was jammed and therefore, no load was being applied; as opposed to if the extensometer freed itself. If the extensometer freed itself, and the load was still being applied, the creep curve should instantly increase to the current strain value as opposed to what actually

happened on the creep curve. For these reasons, it is likely that the load train jammed somehow and the extensometer was properly recording the strain data.

In addition to the 1.0%W sample aged for 144 hrs, corrections were also required for the 1.0%W alloys aged for 8 hrs and stepped aged as well as the 0.5%W stepped aged samples. At the onset of testing, it appears that the extensometers slipped. In the case of the 1.0%W sample, the strain readings started at 0% strain and then went into negative values before proceeding into the positive regime again. To correct this, Beddoes had stated that the instantaneous strain cannot be less than the elastic strain according to Hooke's law [20]. The tensile data presented in section 5.3.2 was referenced to find the strain produced with a 276 MPa stress and an additional 0.15% strain correction was applied to the room temperature tensile data to account for the higher temperatures during creep testing. The additional 0.15% strain was applied since it represented the average increase in strain at 276 MPa when comparing room temperature tensile data to high temperature (760 °C) tensile data of a similar TiAl alloy [22]. For the 1%W and 0.5%W stepped aged samples, the specimens began to creep but then the extensometer slipped and the strain readings returned to zero before starting to creep again. In these cases, room temperatures tensile data was not available. Instead, the same instantaneous strain used for the 1%W alloy aged 8 hrs was used. This is expected to be the lower boundary of the instantaneous strain.

Assuming the corrected curves more closely resemble how the tests actually preceded, the corrected creep results will be analyzed for the discussion. Table 14

summarizes the trends found upon examination of the creep data while Tables 15 - 17 summarize the creep properties.

Table 14 - Creep results comparing unaged and isothermally aged times only

Property	Aging	W addition
Instantaneous Strain	Instantaneous strain is reduced with aging time for the 0%W and 0.5%W samples. The 1%W samples decrease as well with aging time but the improvement is not as large as with the 0%W and 0.5%W alloys.	W improves the instantaneous strain in the unaged condition. Aging for both 8 and 144 hrs shows an improvement with 0.5%W but no improvement is realized with the 1%W addition.
Primary Creep	Aging causes a reduction in the time it takes to reach $\dot{\epsilon}_{min}$. In the samples containing W, aging has a much more profound effect.	W reduces the primary creep in each condition.
Minimum creep strain rate	Aging reduces the minimum strain rate for each of the three compositions.	W additions reduce the minimum creep strain rate in each of the aging conditions except for the 144 hr aging condition where the 0.5%W sample has a lower minimum strain rate than the 1%W sample.
Creep Life	Aging improves creep life in all three of the different compositions except in the 1%W sample where the 8 hrs aged sample has a similar creep life to the 144 hrs aged sample.	W improves creep life in each of the aging conditions except for the 144 hrs aged condition. Aging for 144 hrs found the 0.5%W alloy with the longest creep life followed by the 1%W alloy with the 0%W alloy having the shortest creep life.

Table 15 - Instantaneous Strain (%)

Aging Time (hrs)	W Content (at. %)		
	0	0.5	1
0	0.42	0.41	0.37
8	0.36	0.31	0.34 ¹
Stepped	0.44	0.34 ¹	0.34 ¹
144	0.26	0.31	0.34

Table 16 – Minimum Creep Strain Rate (%/sec)

Aging Time (hrs)	W Content (at. %)		
	0	0.5	1
0	2.85E-05	2.15E-05	9.73E-06
8	1.20E-05	5.39E-06	3.26E-06
Stepped	1.12E-05	6.00E-06	4.40E-06
144	7.47E-06	1.73E-06	2.47E-06

Table 17 - Total Creep Life (hrs)

Aging Time (hrs)	W Content (at. %)		
	0	0.5	1
0	82.17	121.00	195.33
8	185.33	290.40	412.40
Stepped	169.00	244.00	324.50
144	246.14	611.34	413.50

Optical micrographs taken for the ruptured samples are shown in Figure 94, Figure 95 and Figure 96. The micrographs show creep fracture that appears mixed mode (inter and intra-granular). Voids nucleate at grain boundaries perpendicular to the load and at triple

¹ Extensometer slipped during initial loading (Adjustments were made using tensile data from the 1%W aged for 8 hrs condition)

points. With time, the voids coalesced to form larger cracks eventually leading to failure. Cracks seemed to primarily follow grain boundaries except when the crack tip found a grain with lamellae oriented parallel to the crack growth direction. When this occurred, the crack proceeded into the grain and progressed along the lamellar interface.

The optical micrographs also show creep testing causes a number of the lamellae to become bent and wavy as shown in Figure 97. Zhu et al. [95] has suggested that the bent lamellae are the result of the microstructure resisting grain boundary sliding. It was said that a build-up of stress was caused by the interlocked grain boundaries resisting movement of the adjacent grains. The lamellae then bend as a way to relieve this stress. The bent and wavy lamellae are an indication the microstructure has undergone heavy local deformation. In addition to this, more severe necking, void formation and cracking along the length of the test specimen was apparent with increased creep rupture ductility.



Figure 94 - OM micrographs showing cracking in the 0%W sample after creep testing in the a) unaged, b) aged for 8 hrs, c) stepped aging, and d) aged for 144 hrs conditions. Loading was in the vertical direction on the page.

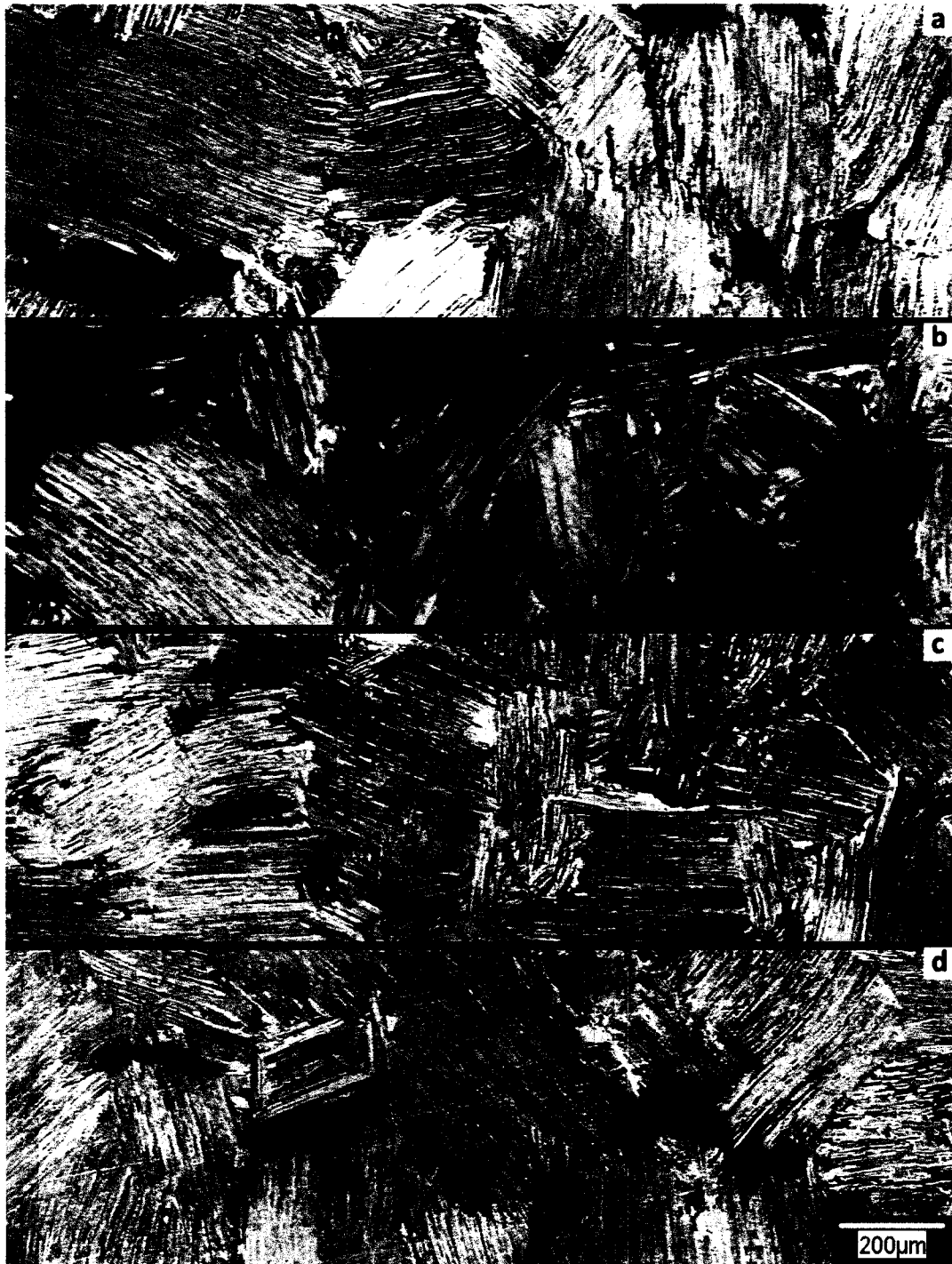


Figure 95 - OM micrographs showing cracking in the 0.5%W sample after creep testing in the a) unaged, b) aged for 8 hrs, c) stepped aging, and d) aged for 144 hrs conditions. Loading was in the vertical direction on the page.



Figure 96 - OM micrographs showing cracking in the 1%W sample after creep testing in the a) unaged, b) aged for 8 hrs, c) stepped aging, and d) aged for 144 hrs conditions. Loading was in the vertical direction on the page.



Figure 97 - As crept 0%W sample aged for 144 hrs. Arrows indicate wavy lamellae.

Figure 98 is a series of SEM-BSE micrographs of the 1%W sample after creep testing. The dynamic precipitation of the β precipitates can be confirmed by comparison of SEM-BSE images in the 1%W unaged condition before and after creep testing as seen in Figure 98 and Figure 99. This was also obvious in the 0.5%W alloy in the unaged condition following creep testing. Both the gauge section and threaded sections of the 0.5%W and 1%W samples showed dynamic precipitation indicating that a combination of high temperature and stress is not required. The high creep testing temperature alone is producing the dynamic precipitation. Figure 98 shows voids nucleated at grain boundaries in each condition. A TEM analysis conducted on the 1%W alloy revealed that both small and large precipitate types were present as indicated by arrows in Figure 100, which is analogous to the undeformed condition. It can be seen that there is extensive interaction between the dislocations and precipitates indicating that the precipitates act as barriers against dislocation movement as shown in Figure 100 b).

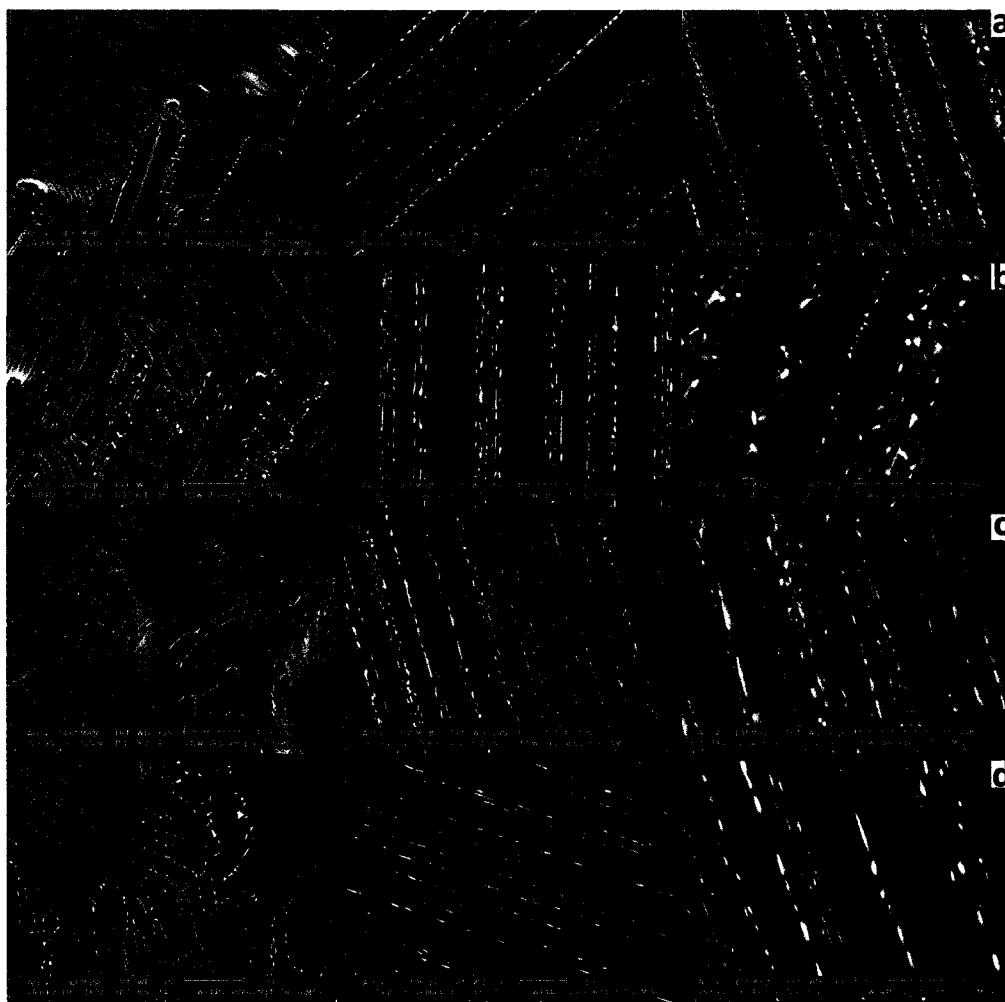


Figure 98 - SEM micrographs of the 1%W sample after creep testing in the a) unaged, b) aged for 8 hrs, c) stepped aging, and d) aged for 144 hrs conditions

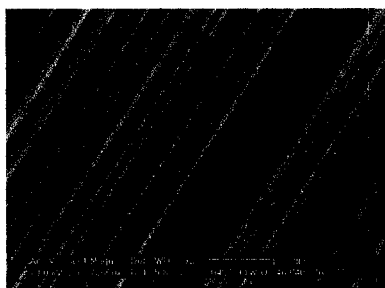


Figure 99 - 1%W unaged before creep testing, no precipitates visible

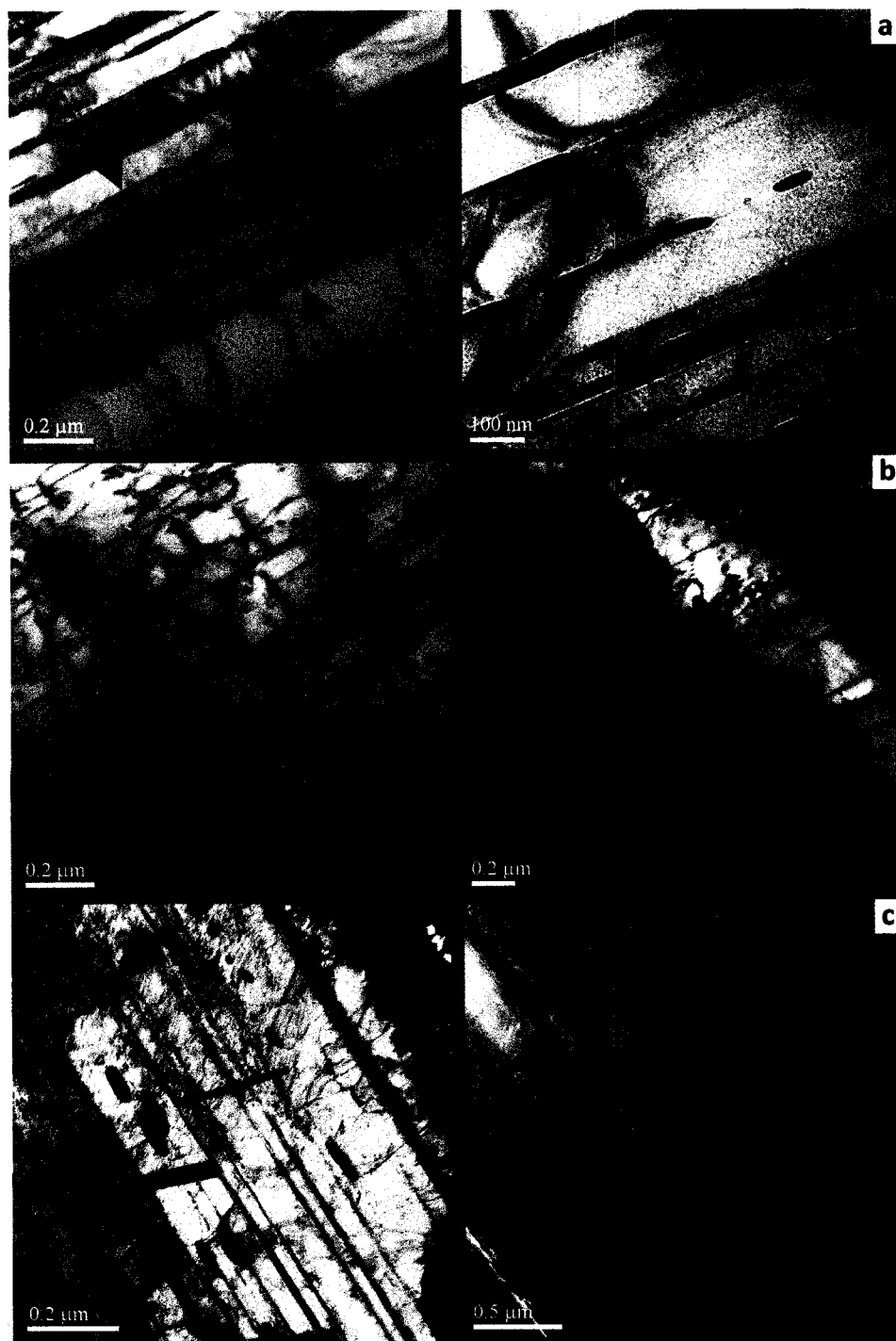


Figure 100 - TEM images taken of the 1%W sample after creep testing in the a) unaged, b) aged for 8 hrs and c) aged for 144 hrs conditions. Small precipitates indicated by short arrows and large precipitates indicated by long arrows.

Tables 14 - 17 show that generally as isothermal aging time and W content are increased, the creep properties are improved. The 0%W samples have improved creep resistance as aging time is increased even though the microstructure appears to be degrading. There is discontinuous and continuous coarsening in addition to the formation of equiaxed γ grains at the lamellar grain boundaries, all of which are detrimental to creep properties. It is possible that aging the 0%W alloys improve creep resistance by reducing the volume fraction of α_2 prior to creep testing. Karthikeyan et al. [96] have suggested that α_2 dissolution during creep liberates a large number of dislocations. By stabilizing the microstructure and reducing the amount of α_2 to values closer to equilibrium, creep properties can be improved. In addition, by causing the dissolution of the α_2 phase, additional Cr is being rejected to the surrounding γ phase (Work from Maziasz et al. [92] has shown that before the α_2 phase can be dissolved, it must return to a more stoichiometric composition, thereby rejecting an alloying additions to the surrounding area). Cr has been shown to strengthen the γ phase [5] so it is possible that a portion of the improved creep properties come from this solid solution strengthening mechanism. The 0.5%W and 1%W have improved creep resistance due to the precipitates at the lamellar interfaces. As discussed in section 2.3.1.4, TiAl alloys deformed at elevated temperatures primarily through dislocation emission and glide along the lamellar interfaces. The precipitates seem to effectively block the emission and motion of dislocations at and along the lamellar interfaces which is in agreement with other work [18].

It is noticed that the 0.5%W sample aged for 144 hrs showed the best creep properties as shown in Table 16, Table 17 and Figure 88. In each of the other aging conditions, increasing the W content improves the creep life. This was not the case with samples aged for 144 hrs where the 0.5%W sample had a creep life roughly 200 hrs longer than the 1%W sample and roughly 350 hrs longer than the 0%W sample. To explain this, work from Seo et al. [18] is used which examined a fully lamellar Ti-48-2W alloy and found that following aging, creep life was reduced. It was suggested the cause of the reduced creep life to be related to precipitate size at the grain boundaries. The large grain boundary precipitates caused inter-granular void formation and reduced tertiary creep life leading to shorter overall creep lives. It is possible that due to the higher W content in the 1%W sample aged for 144 hrs, the precipitates at the grain boundaries have grown large enough to act as sources of inter-granular voids. Whereas in the 0.5%W alloy, the W content is not high enough to support the growth of large inter-granular precipitates. It could be that after 144 hrs, the 0.5%W alloy has an ideal size and distribution of precipitates at both the grain boundaries and lamellar interfaces to show the improvements in creep properties seen in Figure 84.

Creep properties between the 8 hrs aged and stepped aged samples have been compared in Table 18. The comparison between the two was made since the stepped aging sample had a final hold of 8 hrs at 950 °C, identical to the isothermally aged 8 hrs sample at the same temperature. The difference between the two aging conditions was the total time for aging. The isothermally aged sample was placed in the furnace which was

pre-heated to 950 °C while the stepped aged sample slowly increased in temperature from room temperature. In addition to the comparisons made in Table 18, Figure 101 is a direct comparison of the creep curves between the two aging conditions.

Table 18 - Creep results comparing stepped aging to the isothermally aged 8 hr sample

Property	Result
Instantaneous Strain	Both the 0.5%W and 1%W alloys aged for 8 hrs show similar instantaneous strain compared to the stepped aged condition while the 0%W alloy shows an improvement with 8 hrs aging over the stepped aging.
Primary Creep	Primary creep times show similar values with the aged 8 hrs condition compared to stepped aging.
Minimum creep strain rate	0%W shows similar $\dot{\epsilon}_{min}$ between 8 hrs isothermal and stepped aging while the 0.5%W and 1%W alloys show an increase with stepped aging.
Tertiary Creep	Both W containing alloys showed a slightly lengthened tertiary creep phase in the 8 hrs aged condition compared to stepped aging while the 0%W alloy showed similar tertiary creep in both aging conditions.
Creep Life	8 hrs isothermal aging showed improved creep life over the stepped aging and the margin of that increase grew as W content increased.

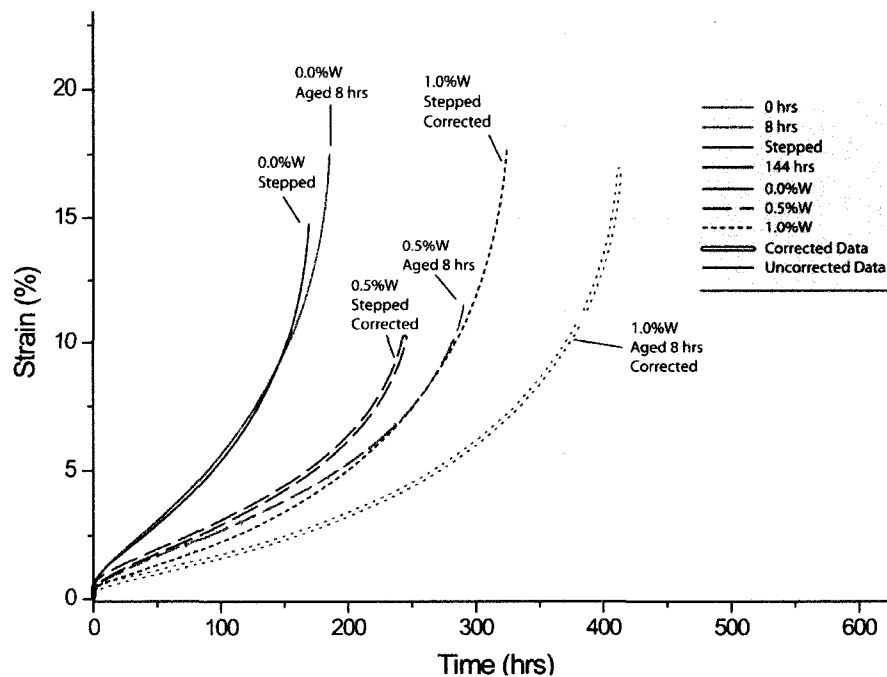


Figure 101 - Creep curves from each alloy comparing the 8 hrs aged and stepped aged conditions (760 °C and 276 MPa load)

It is interesting to note that although the microstructure of the 8 hrs isothermally aged samples appear to have undergone more severe coarsening and formed more equiaxed γ compared to the stepped aging, the 8 hrs isothermally aged samples seem to have improved instantaneous strain, tertiary creep and overall creep life compared to the stepped aged samples. The 0%W alloy had similar minimum creep strain rates between the two aging conditions while the 0.5%W and 1%W alloys produced a reduced minimum creep strain rate with stepped aging.

The reason for the 8 hrs aged samples performing better (in the case of the 0%W alloy, performing similarly) in creep tests than the stepped aged samples is unclear. The microstructures after aging would suggest that the stepped aged samples would perform

better during creep testing. Each of the alloys in the stepped aged condition have no equiaxed γ around the grain boundaries, show limited discontinuous coarsening and the continuous coarsening occurs in such a way that the α_2 lamellae are thinned but not broken up. Each of those features is likely to improve creep properties compared to the 8 hrs isothermally aged conditions. If the assumption is made that the volume fraction of α_2 is reduced to a similar amount in both aging conditions, stepped and isothermal (which is in agreement with work from Zhu et al. [35]), then some discussion is possible. Firstly, any solid solution strengthening of the γ phase caused by the dissolution of the α_2 phase should be similar when comparing stepped and isothermal conditions in each of the three alloys. As the α_2 lamellae are thinned, the solutes will repartition to either the remaining α_2 phase, the γ phase, or in the W containing alloys, to precipitates. In each of the three different alloy compositions (0, 0.5 and 1%W), similar repartitioning is expected when comparing stepped or isothermal aging. If the assumption that similar volume fractions of α_2 remain, then there are three expected differences between the two aging mechanisms; the manner in which the α_2 is transformed to γ , precipitate size and distribution and the amount of equiaxed γ at the grain boundaries.

As was discussed in section 5.1.3.3, it is believed that there are more precipitates present and that they are smaller in size in the stepped aged condition compared to the isothermal condition. It could be that the precipitate size may be too small to be effective at pinning dislocations during creep. This could explain why there was a more significant

difference in the creep curves between the stepped and isothermal aging conditions especially in the 1%W alloy.

It was also discussed in section 5.1.3.3 and suggested by Seo et al. [18] that the formation of precipitates could be detrimental to the stability of the α_2 phase since the β precipitates have higher partitioning coefficients for alloying elements such as W. W has been suggested to stabilize the α_2 lamellae against dissolution when it remains in solid solution at lamellar interfaces [80]. Additionally, aging at higher temperatures is thought to cause larger and more dispersed precipitates. Since the precipitates are more spaced out, the regions of α_2 in between the precipitates will be larger and the slow diffusing W will have larger distances to travel before it can leave the α_2 lamellae and partition to the precipitates. Compare this to the stepped aging process which will have more and smaller precipitates at lamellar interfaces due to the lower initial aging temperature. As the aging temperature continues to rise, the small precipitates that nucleated at the lower aging temperatures will continue to grow since diffusion becomes easier at higher temperatures. The fine spacing of the precipitates could mean that W will be removed from the α_2 lamellae at a higher rate in the stepped aged samples compared to those isothermally aged. If this is the case, dissolution of the α_2 lamellae may occur faster in stepped aged samples. If this was true, it would suggest that stepped aging would produce a more stable microstructure. Work from Karthikeyan et al. [96] has suggested that for improved creep strength, it may be more important to obtain a more stable microstructure than it is to maintain a high volume fraction of the harder α_2 phase. Again, these arguments would

suggest that stepped aging should have improved creep properties compared to the isothermally aged condition.

Additionally, Zhu et al. [35] has shown that α_2 undergoes longitudinal dissolution during stepped aging which produces improved creep results. It is thought to be beneficial since it does not cause breakup of the α_2 lamellae entirely while it reduces the fraction of α_2 to a value closer to equilibrium. In Zhu's work, however, no precipitates were formed that would act as a sink for alloying elements. It is unclear how the precipitates might affect the longitudinal dissolution process. If dissolution of the α_2 phase continues to occur in a longitudinal manner, then an improvement to the creep properties in each alloy should be realized. However, examination of the creep curves (Figure 101) shows no improvements compared to the isothermal aged condition and the W alloys show increasing reductions of creep properties with increasing W content.

Finally, previous studies have shown that equiaxed γ at grain boundaries is detrimental to creep properties [20, 39]. Since all of the stepped aged samples show no equiaxed γ formation, they should have better creep results compared to their respective W content after isothermal aging. Again, examination of the creep curves does not reflect this.

The above arguments are each made based on the assumption that similar amounts of α_2 remain in both stepped and isothermal aging. This assumption was made based on work from Zhu et al. [35]. However, Zhu did not have any precipitates which could change the kinetics of α_2 dissolution. There may indeed be a larger variation in α_2 volume

fractions comparing the two aging conditions then the variation that Zhu had seen since a difference could explain the difference in creep properties. The short tertiary creep stage in the stepped aging samples may suggest the microstructure is not completely stabilized as in the 8 hrs isothermal aging samples. Beddoes has written that the increasing $\dot{\epsilon}$ in the tertiary creep regime is generally associated with microstructural instabilities or the formation and coalescence of voids or cracks [20]. It was also stated that grain size can play an important role in tertiary creep. In the current investigation between the 8 hrs aging and stepped aging, grain size is not expected to vary significantly between samples since each underwent identical SHT's. A comparison of SEM micrographs between the two aging conditions reveals no gross difference between void nucleation and cracking. Figure 102 is a comparison between the 1%W alloy in the two aging conditions. It is, therefore, possible that the differences in tertiary creep between the two aging conditions is due to microstructural instabilities and more specifically, possibly a result of differences in the amount of retained α_2 following the heat treatments.

It is apparent from these discussions that more research is required in the area to discern the mechanisms for the reduction in creep resistance observed in the stepped aged samples compared to their isothermally aged counterparts, especially since stepped aged microstructures seem superior.

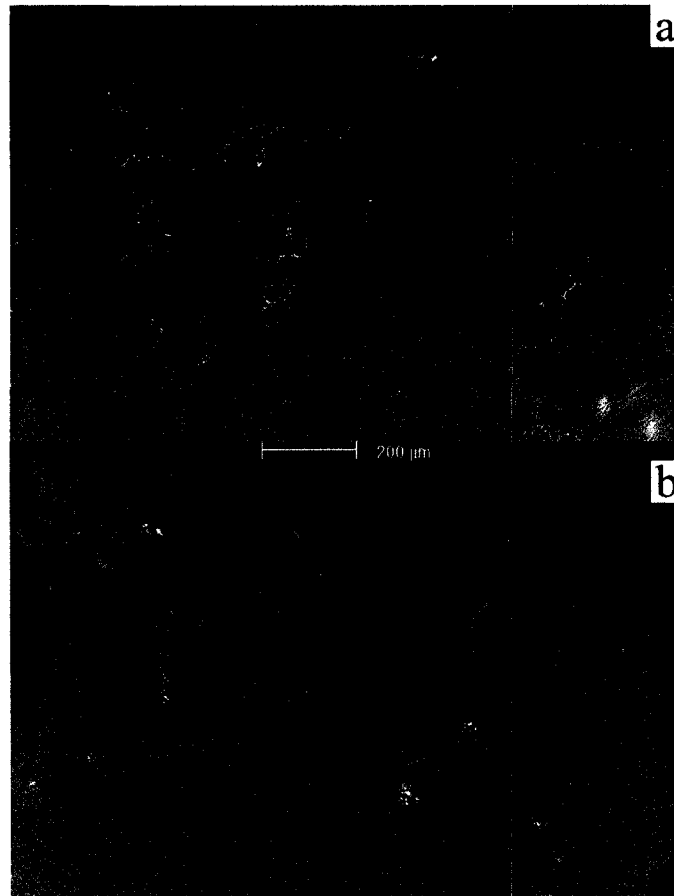


Figure 102 - Void nucleation comparison after creep in the 1%W alloy a) 8 hrs aging, b) stepped aging

5.3.2 Tensile Testing

Tensile tests were conducted on unaged and 8 hrs aged samples. The unaged condition was selected to understand the effect of aging on tensile properties by serving as a baseline with which to measure aging improvements. The aging time of 8 hrs was chosen since it showed limited microstructural degradation, Figure 59, as well as the formation of precipitates at lamellar interfaces and grain boundaries, Figure 69 and Figure 70.

Results from the room temperature tensile tests can be seen in Figure 103 and summarized in Table 19.

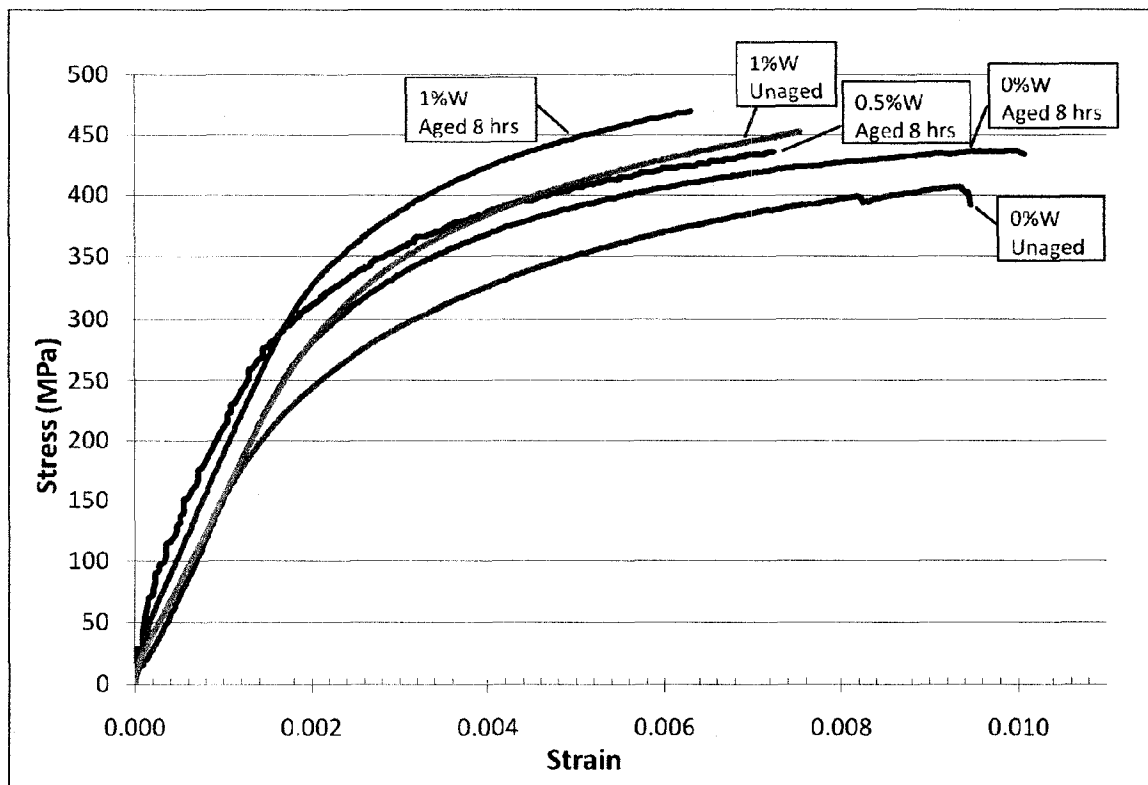


Figure 103 – Stress and strain curves for the three alloys in the unaged and aged for 8 hrs conditions

Table 19 - Summary of tensile data

Condition		Tensile Properties			
Aging	%W	Yield Strength (MPa)		% Elongation	UTS (MPa)
		0.02%	0.2%		
Unaged	0	241	337	0.95	406
	0.5	NA	NA	NA	NA
	1	310	406	0.75	453
Aged 8 hrs	0	278	378	1.05	436
	0.5	313	393	0.73	436
	1	346	441	0.63	470

Figure 103 and Table 19 show that increasing W content and aging time improve strength and reduce ductility. Comparing the results from tensile testing to those obtained through micro-hardness testing, Figure 82, the following observations were made on the effects of W additions as well as aging.

When comparing the 0%W and 1%W alloys in the unaged condition, it is apparent that the W addition improves the tensile strength and reduces elongation. Micro-hardness testing revealed similar hardness values for the lamellae of both the 0%W and 1%W alloys. Hardness tests are usually used as a quick method for determining a material's deformation behaviour and so the results from both tensile and hardness tests should reveal similar trends. The difference between the tensile and micro-hardness tests may be related to the nature of the micro-hardness test. Since the micro-hardness tests were conducted within the centers of each grain, any grain boundary effects would not play a role. Deformation caused by micro-hardness indentations are also very localized since the size of the indentations are very small.

When comparing the 8 hrs aged condition, W additions strengthen the 0.5%W and 1%W alloys in a nearly linear fashion. When examining the micro-hardness data, however, the addition of W seems to have a negative impact on hardness for the 0.5%W alloy in the 8 hrs aged condition and improvements in hardness are not seen until 1%W is added. As mentioned previously, it was postulated that the reduction in hardness was due to the increased lamellar spacing in the 0.5%W alloy and not because W directly reduces the strength of TiAl. W additions have been shown to improve the strength of TiAl, [36,

78], but it is possible that the addition of W could have the secondary effect of increasing lamellar spacing which in turn could cause the reduction in hardness seen in the micro-hardness data. By comparing tensile and hardness data for the 0.5%W and 0%W alloys, it would appear that the grain boundaries play an important role in the tensile strength of the material since the hardness in the 0.5%W alloy is lower compared to the 0%W alloy, however, the tensile strengths are reversed. Additional evidence for this is the similar hardness for the 0%W and 1%W alloys in the unaged condition and yet the 1%W alloy has improved yield strength.

Aging each of the compositions also improved strength. Aging the 0%W alloy stabilized the microstructure by reducing the α_2 volume fraction through the different coarsening mechanisms (discontinuous and continuous coarsening as well as equiaxed γ formation). Coarsening caused an increase in the γ phase near the grain boundaries through thickening of the γ lamellae and formation of equiaxed γ . Comparing tensile and hardness data for the two 0%W aging conditions show that the strength was improved yet the hardness decreased. Again, the grain boundaries seem to play a large role in improving the strength in the 0%W condition. It could be the formation of the equiaxed γ at the grain boundaries that may be the source of the improved strength in the 0%W alloy after aging. The room temperature strength of TiAl has a Hall-Petch type relationship between the grain size and the yield strength, so it could be that the equiaxed γ reduces the average grain size which results in improved strength with aging. Also duplex microstructures have superior room temperature strength and they are composed of a high

volume fraction of equiaxed γ (typically around 50%) [5]. The 0%W alloy seemed to show a small increase in the elongation following aging while the 1%W alloy showed a small reduction. It seems likely the small variations of roughly 0.1% strain are within the accuracy limits of the experiment and do not likely demonstrate quantitative changes in elongation. It is possible, however, some of the reduced elongation in the 1%W alloy could be linked to the precipitates at the lamellar interfaces and grain boundaries after aging. The reduced dislocation mobility could inhibit deformation of the test specimen and therefore reduce the amount of strain before failure. As in the 0%W alloy, aging the 1%W alloy also stabilized the microstructure through discontinuous and continuous coarsening as well as precipitation at lamellar interfaces and grain boundaries and through the nucleation and growth of a small amount of equiaxed γ . Comparing the 1%W aged for 8 hrs to the 0%W in the unaged condition, an increase of 16% for the UTS and a decrease of 34% for the elongation was observed.

The fracture surfaces of the tensile samples were examined to understand the fracture mode of the material using the SEM. The results are shown in Figures 104, 105 and 106.

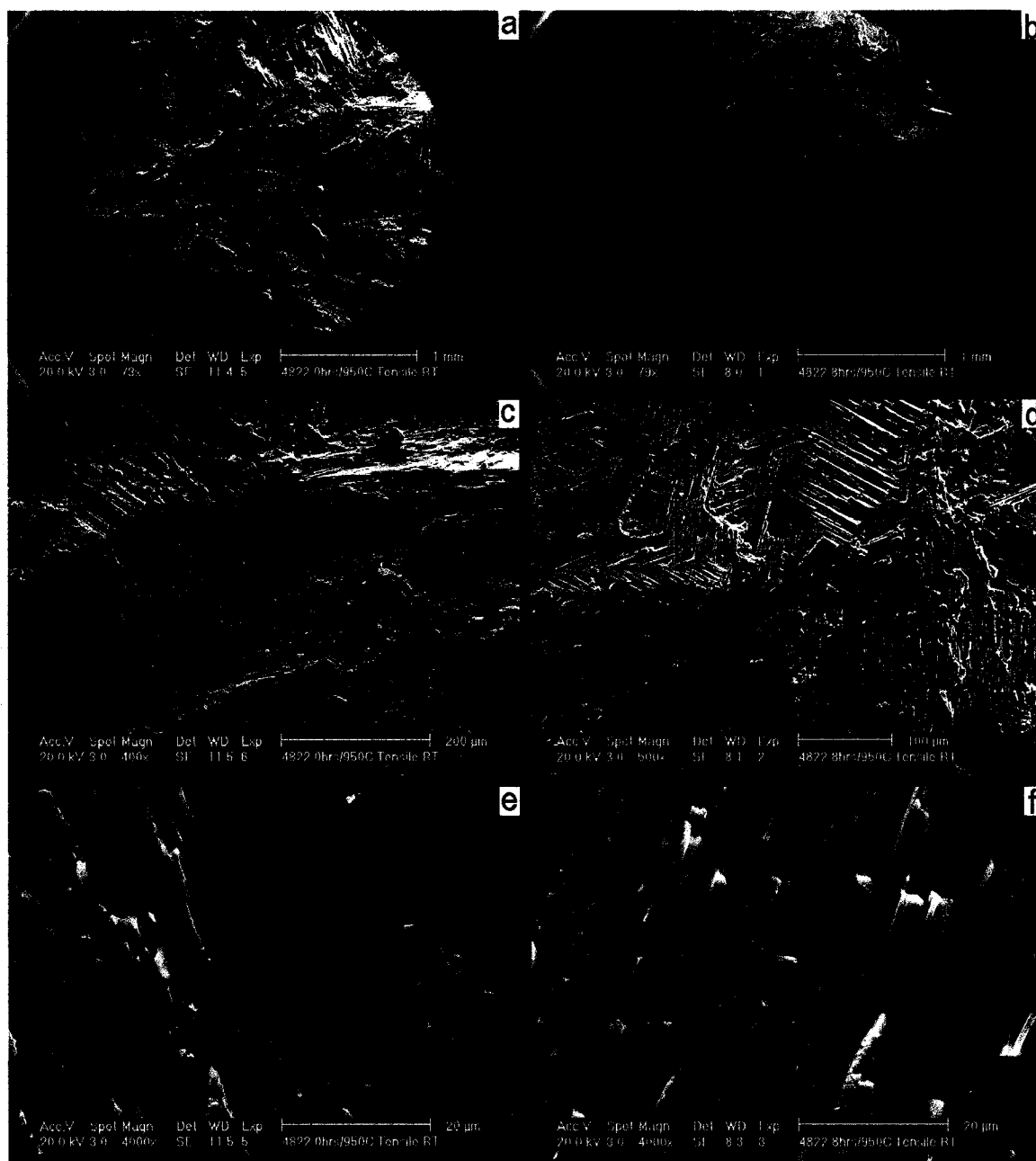


Figure 104 - Low and high magnification SEM-SE micrographs of the 0%W sample unaged (left column) and aged for 8 hrs (right column).

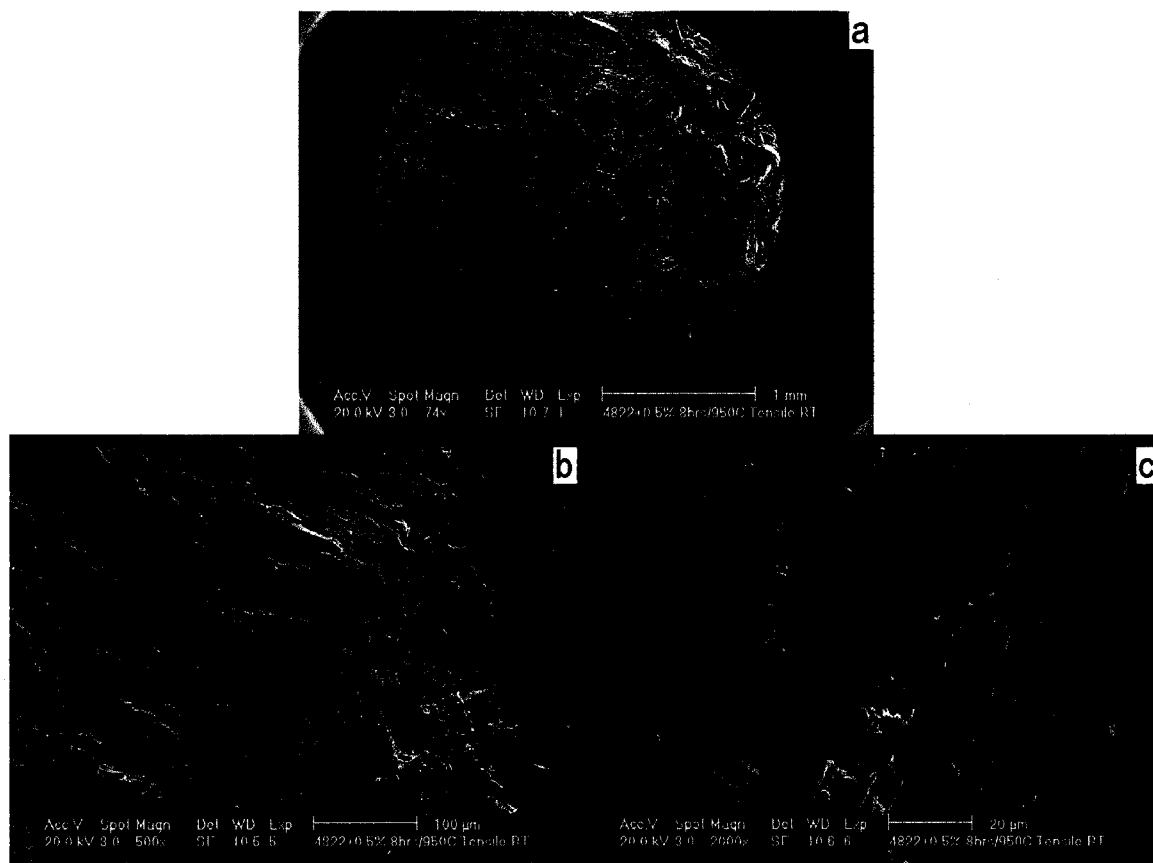


Figure 105 - Low and high magnification SEM-SE micrographs of the 0.5%W sample aged for 8 hrs. Arrow indicates de-lamination

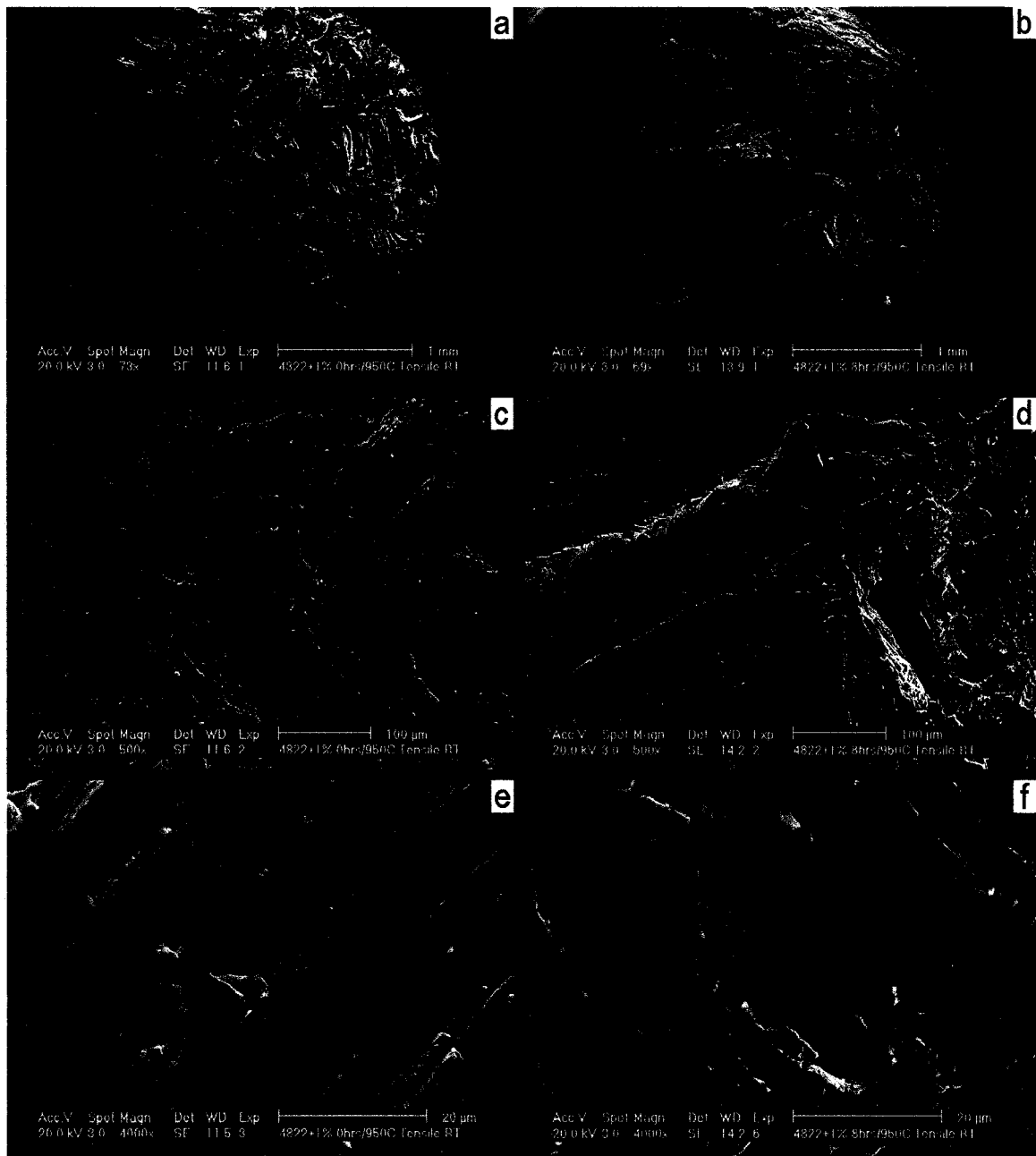


Figure 106 - Low and high magnification SEM-SE micrographs of the 1%W sample unaged (left column) and aged for 8 hrs (right column). Arrow indicates de-lamination.

The micrographs of the fracture surfaces of the alloys show three fracture modes, inter-granular (along the grain boundaries), intra-granular (across the grains) and inter-

lamellar (along the lamellar interfaces). There appears to be some inter-granular cracking as denoted by the mountainous fracture surfaces seen in the low magnification images in Figures 104, 105 and 106. In addition, intra-granular fracture was seen in the high magnification micrographs of the lamellae in Figures 104(e, f), 105(c) and 106(e, f). Finally, inter-lamellar fracture was also apparent (large flat fracture surfaces and delamination of the lamellae) but not as prominent as inter or intra-granular fracture.

Inter-granular fracture does not appear to be as prominent as intra-granular fracture in the samples examined. It would seem that the crack only followed the grain boundary when it was reasonably parallel to its current heading. If an easy grain boundary path was not available, the grain itself was fractured either along a lamellar interface or in an intra-granular fashion. Inter-lamellar fracture is an easy fracture mode [97] and would be preferred to intra-granular fracture. This illustrates a dependence on grain orientation which could possibly have a large impact on the tensile properties. Minimizing grain size would reduce the anisotropy of crack resistance depending on grain orientation but it highlights the potential variation of the results during tensile testing.

In thin tensile test specimens, inter-lamellar fracture occurs preferentially over plastic deformation [98]. Cao et al. [97] suggested that inter-lamellar cracking, or microcracking, occurs before final failure of the tensile specimen and is how the specimen accommodates the imposed deformation. Cao has suggested that the lack of any riverbed pattern on the surface of microcracks is a feature which can be used to identify them. Once the density of these microcracks is sufficiently high in any cross section of the test

specimen, final fracture occurs as a large crack links all the microcracks. It is this final linking crack that rapidly grows and produces surfaces with evidence of directional crack growth (riverbed pattern). Figure 107 shows a crack facet with the directional cleavage fracture denoted by the arrow.

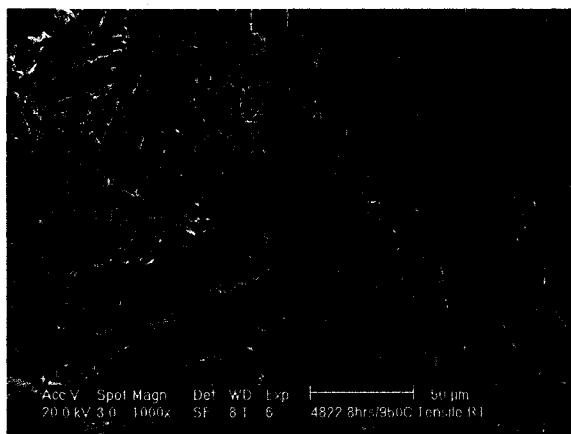


Figure 107 - 0%W alloy aged for 8 hrs showing a distinct cleavage river pattern. Arrow indicates direction of crack propagation

When comparing the fracture surfaces found from the different aging conditions and W additions (Figures 104, 105 and 106) to the fracture surfaces obtained by Cao et al. [97] (Figure 108), fewer microcracks or inter-lamellar fractures were apparent on the fracture surface in all of the test specimens. Cao's work had a comparatively large number of flat fracture surfaces which were roughly 700 - 1000 μm in size, which is also the grain size of his samples. Only the 0%W alloy had any apparent inter-lamellar cracking at the fracture surface as seen in Figure 104 a) and b). It would seem the precipitates at the lamellar interfaces make it less favourable for a crack to grow in this mode. In addition, by having a grain size smaller than Cao, if any inter-lamellar cracks do initiate, they will be limited by the smaller grain size.

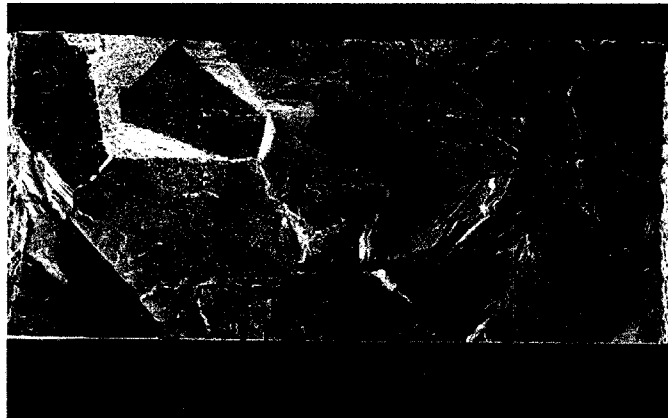


Figure 108 - Fracture surface of a FL thin tensile test specimen with microcracks encircled with a black line. Microcracks comprise 29% of the fracture surface [97]

Intra-granular fracture seems to occur in a manner typical to grains oriented in the “hard” direction (lamellar interfaces perpendicular to crack growth). Yamaguchi et al. [99] has suggested that a delamination-type separation occurs ahead of the crack tip due to triaxial stresses ahead of the crack tip as shown in Figure 109. The results from the current tensile testing seem to show similar features at the fracture surface. Rough non-uniform edges are apparent when examining the high magnification SEM micrographs in Figures 104(e, f), 105(c) and 106(e, f).

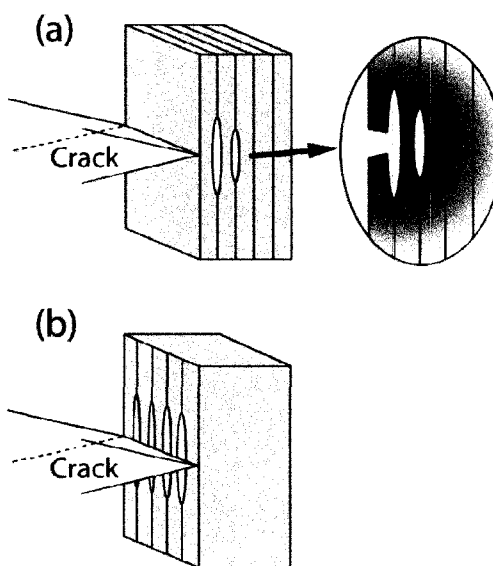


Figure 109 - Delamination occurring ahead of the crack tip [99]

There does not appear to be any significant difference between failure modes in the examined samples. However, the 0%W alloy does seem to show an increased propensity for inter-lamellar fracture compared to the 0.5%W and 1%W alloys. Work from Fuchs also shows that the failure mode is insensitive to processing and W additions (Fuch had examined both ingot metallurgy and powder metallurgy processing routes with a nearly lamellar microstructure) [36].

Chapter 6: Summary and Conclusions

To summarize, three powder metallurgy alloys were examined, Ti-48Al-2Cr-2Nb, Ti-48Al-2Cr-2Nb-0.5W and Ti-48Al-2Cr-2Nb-1W. Following HIP'ing, an optimised step cooled heat treatment (SCHT) was initially used to form a fully lamellar microstructure free of γ_m and Widmanstätten structures. The heat treatment consisted of heating to 1400 °C and holding for 40 min, followed by furnace cooling to 1270 °C and then air cooling to room temperature. It was found that a 40 min hold time at 1400 °C was required for the W containing samples to allow a reasonable amount of homogenization to occur without incurring excessive grain growth. W was also beneficial in reducing the propensity for γ_m formation for stepped cooling transition temperatures near 1270 °C. A $T_{F/A}$ of 1270 °C was found to be ideal since increasing $T_{F/A}$ caused γ_m to form while decreasing $T_{F/A}$ could cause undesirable thickening of the lamellae and could cause precipitation of the β phase.

Isothermal aging was then carried out at 950 °C for 8 - 432 hrs on samples to stabilize the microstructure. Precipitates were also formed at lamellar interfaces and grain boundaries in W containing samples. W additions were found to be beneficial during aging because they limited the amount of coarsening and the formation of equiaxed γ , which was visible in the non W containing alloy. The stepped aging process seemed to

yield an improved microstructure, for each composition, as compared to that produced by the isothermal aging process. The stepped aging stabilized the samples and produced no, or at least very limited, equiaxed γ , and reduced the amount of coarsening observed. Similar to isothermal aging, stepped aging caused precipitates to form at lamellar interfaces and grain boundaries in W containing samples.

Micro-hardness testing was used as a guide to select samples for further mechanical testing. The hardness tests showed that for limited or no aging, small W additions are not beneficial and only after 1%W is added, was an improvement in micro-hardness realized. This was likely linked to the finer lamellar spacing in the 0%W alloy compared to the two W containing alloys. At increased aging times, however, W additions were beneficial and the hardness increased with W content. Comparing isothermal aging times, a similar trend was visible in each of the three alloy compositions. There was an initial reduction in hardness which reached a minimum at 72 hrs and was then followed by a hardness peak at 144 hrs aging. Further aging to 432 hrs showed a small reduction in hardness with the W samples and a nearly unchanged hardness for the base 0%W alloy. The stepped aging condition was able to increase the hardness in the 1%W alloy and only produced a small hardness reduction in the 0.5%W alloy. A much larger reduction in hardness was produced in the 0%W alloy.

The results of creep tests in air at 760 °C and 276 MPa showed the improvement of creep resistance with W additions and aging. The W additions resulted in the formation of precipitates at grain boundaries and lamellar interfaces. The interfacial precipitates

work as an effective barrier against dislocation emission and motion. By blocking the emission of dislocations from lamellar interfaces, the primary creep in W containing alloys was improved. Also, minimum creep strain rates were reduced and creep life was increased in each aging condition with the addition of W. Especially the 0.5%W alloy in the 144 hr aged condition which demonstrated the lowest minimum creep strain rate and the longest creep life. In addition, stepped aging had a negative impact on the creep properties of the W containing alloys. The failure mode in each of the crept samples appeared to be of a mixed mode nature where voids nucleated at grain boundaries perpendicular to the load and at triple points. With time, the voids coalesced to form larger cracks eventually causing final fracture.

The results of room temperature tensile testing show improved yield strength and decreasing ductility with increasing W and aging. The fracture mode of the tensile tests specimens appeared similar in each case. Failure occurred through mixed mode fracture consisting of inter and intra-granular cracking as well as inter-lamellar cracking.

A summary of the effects of W on the base Ti-48Al-2Cr-2Nb alloy include;

- Increased the time required for complete homogenization during the SCHAT
- Likely caused the increased lamellar thickness during cooling from T_α
- Reduced the propensity for γ_m formation at stepped cooling transition temperatures near 1270 °C
- Reduced the amount of coarsening and nucleation and growth of equiaxed γ during aging

- Formed precipitates at lamellar interfaces and grain boundaries
- Longest creep life and lowest minimum creep strain rate obtained with the 0.5%W alloy after 144 hrs aging
- Showed the highest yield strength and lowest ductility in the 1%W alloy with 8 hrs aging

To conclude, the results from this study show that W additions demonstrated the improvement of creep and room temperature strength compared to the base Ti-48Al-2Cr-2Nb alloy. To achieve the largest improvements to creep and tensile properties, W additions in conjunction with an optimized step cooled heat treatment and aging should be used. The optimized SCHAT was found to consist of heating to 1400 °C for 40 min followed by furnace cooling to 1270 °C and air cooling to room temperature. The ideal aging time and composition, out of those analyzed, for creep resistance was found to be the 0.5%W alloy aged for 144 hrs. While the best tensile results were produced with the 1%W alloy aged for 8 hrs.

6.1 Future Research

Results discussed earlier have shown that there are some interesting questions that are still unanswered and are areas where future work may investigate. Specifically, the nucleation mechanisms and the morphology of the small precipitates found in the 1%W alloy and the strengthening mechanism which improved the micro-hardness in the 0%W alloy after aging for 144 hrs. Additionally, a study on why the creep results for the isothermally aged samples were generally better than the stepped aged samples even

though the stepped aged samples had what appeared to be a microstructure better suited for creep.

Detailed TEM work is required on the 1%W alloy near the lamellar interfaces to accurately describe the nucleation mechanisms and morphology of the small precipitates. Additionally, TEM-EDS work near the lamellar interfaces may provide some clues as to the strengthening mechanism in the 0%W alloy after aging for 144 hrs. It would be interesting to see if the Cr is indeed providing enough strengthening to produce the hardness increase. A residual stress analysis may also be beneficial for determining aging effects on the lamellar interfaces and could provide some insight into the strengthening mechanism in the 0%W alloy following aging. Adjusting the SCHAT for the 0%W alloy to produce thicker lamellae with sizes more comparable to the 0.5%W and 1%W alloys would also help remove an additional unknown and could make it easier to discover any strengthening mechanisms. Isolating lamellar coarsening from precipitation could also be beneficial. To discover why the stepped aged samples performed poorly during creep tests compared to the 8 hrs aged samples, a study similar to that performed by Zhu et al. [35] on the lamellar coarsening mechanisms may answer the question. Zhu's study did not consider precipitates and so it is unclear as to how the precipitates may affect the longitudinal and lateral coarsening mechanisms.

Beyond the work included in this thesis, the next step for improving the properties of the Ti-48Al-2Cr-2Nb-xW alloys may be to reduce grain size which has been shown to improve room temperature tensile properties. Cyclic heat treatments or boron additions

may be beneficial in this aspect. The reduced grain size ($\sim 100 \mu\text{m}$) would improve ductility while still maintaining good creep properties.

References

- [1] F. Appel and M. Oehring, "Gamma-Titanium Aluminide Alloys: Alloy Design and Properties," in *Titanium and Titanium Alloys; Fundamentals and Applications*, C. Leyens and M. Peters, Eds. Weinheim, Germany: Wiley-VCH GmbH & Co. KGaA, 2003.
- [2] S. C. Huang and J. C. Chesnutt, "Gamma TiAl and its Alloys," in *Structural Applications of Intermetallic Compounds*. vol. 3, J. H. Westbrook and R. L. Fleisher, Eds. Chichester, West Sussex, England: John Wiley & Sons Ltd, 2000.
- [3] H. M. J. Saari, "Process Modeling of the Directional Solidification of Gas Turbine Materials," Ph.D. dissertation, Ottawa: Carleton University, 2003.
- [4] *Smithells Metals Reference Book*. Burlington, MA, United States of America: Elsevier Inc., 2004.
- [5] F. Appel and R. Wagner, "Microstructure and Deformation of Two-Phase Gamma-Titanium Aluminides," *Materials Science and Engineering*, vol. R22, pp. 187-268, 1998.
- [6] D. Seo, "The Effect of Heat Treatments on Microstructures and Primary Creep Deformation of Investment Cast Titanium Aluminide Alloys and Polysynthetically Twinned (PST) Crystals," Ph.D. dissertation, Michigan: Michigan State University, 1998.
- [7] *The Jet Engine*. Derby, England: Rolls-Royce Ltd., 1996.
- [8] G. Norris, "Power House," in *Flight International*. Internet: <http://www.flightglobal.com/articles/2006/06/13/207148/power-house.html>, Jun. 13, 2006, [Aug. 8, 2008].

- [9] "Widebody Engine Update GENx and GE90," Internet: http://www.geae.com/aboutgeae/presscenter/genx/genx_20080714.html, Jul. 14 2008 [Aug. 8 2008].
- [10] "Emission Testing on GENx Engines Exceed Expectations and Validate TAPS Combustor Technology," Internet: http://www.geae.com/aboutgeae/presscenter/genx/genx_20070618b.html, Jun. 18 2007 [Aug 8 2008].
- [11] "GENx-1B Engine Receives FAA Certification," Internet: http://www.geae.com/aboutgeae/presscenter/genx/genx_20080331.html, Mar. 31 2008 [Aug 8 2008].
- [12] K. Liu, Y. C. Ma, M. Gao, G. B. Rao, Y. Y. Li, K. Wei, X. Wu, and M. H. Loretto, "Single step centrifugal casting TiAl automotive valves," *Intermetallics*, vol. 13, pp. 925-928, 2005.
- [13] T. Tetsui, "Development of a TiAl turbocharger for passenger vehicles," *Materials Science and Engineering A*, vol. A329-331, pp. 582-588, 2002.
- [14] K. Gebauer, "Performance, tolerance and cost of TiAl passenger car valves," *Intermetallics*, vol. 14, pp. 355-360, 2006.
- [15] F. H. Froes, C. Suryanarayana, and D. Eliezer, "Synthesis, properties and applications of titanium aluminides," *Journal of Materials Science*, vol. 27, pp. 5113-5140, 1992.
- [16] E. A. Loria, "Gamma titanium aluminides as prospective structural materials," *Intermetallics*, vol. 8, pp. 1339-1345, 2000.
- [17] J. Beddoes, D. Y. Seo, W. R. Chen, and L. Zhao, "Relationship Between Tensile and Primary Creep Properties of Near Gamma-TiAl Intermetallics," *Intermetallics* 9, pp. 915-922, 2001.
- [18] D. Y. Seo, J. Beddoes, L. Zhao, and G. A. Botton, "The Influence of Aging on the Microstructure and Creep Behaviour of a Gamma-Ti-48%Al-2%W Intermetallic," *Materials Science and Engineering A*, vol. A329-331, pp. 810-820, 2002.

- [19] H. Zhu, D. Y. SEO, K. Maruyama, and P. Au, "Interfacial strengthening of β phase in a fully lamellar structure of TiAl alloy containing W," *Philosophical Magazine Letters*, vol. 85, pp. 377–385, 2005.
- [20] J. Beddoes, W. Wallace, and L. Zhao, "Current Understanding of Creep Behaviour of Near Gamma-Titanium Aluminides," *International Materials Reviews*, vol. 40, pp. 197-217, 1995.
- [21] P. Au, "A Heat Treatment Procedure to Produce Fine-Grained Lamellar Microstructures in a P/M Titanium Aluminide Alloy," Ph.D. dissertation, Ottawa: Carleton University, 1997.
- [22] W. Chen, "Microstructure Modification and Mechanical Behaviour of an Investment Cast Near γ -TiAl Intermetallic Alloy," Ph.D. dissertation, Ottawa: Carleton University, 2000.
- [23] S. C. Huang, E. L. Hall, and D. S. Shih, "Microstructure and ductility of TiAl alloys modified by Cr additions," *ISIJ International*, vol. 31, pp. 1100-1105, 1991.
- [24] S.-C. Huang and E. L. Hall, "Effects of Cr additions to binary TiAl-base alloys," *Metallurgical Transactions A (Physical Metallurgy and Materials Science)*, vol. 22A, pp. 2619-2627, 1991.
- [25] G. B. Viswanathan, "Microstructural effects on the tensile and creep behavior of Ti-48Al based gamma titanium aluminides," Ph.D. dissertation, Ohio: University of Cincinnati, 1997.
- [26] L. Zhao, J. Beddoes, P. Au, and W. Wallace, "Evaluations of P/M Gamma Titanium Aluminides," *Advanced Performance Materials*, vol. 4, pp. 421-434, 1997.
- [27] S. A. Jones and M. J. Kaufman, "Phase equilibria and transformations in intermediate titanium---aluminum alloys," *Acta Metallurgica et Materialia*, vol. 41, pp. 387-398, 1993.

- [28] M. Beschliesser, A. Chatterjee, A. Lorich, W. Knabl, H. Kestler, G. Dehm, and H. Clemens, "Designed Fully Lamellar Microstructures in a Gamma-TiAl Based Alloy: Adjustment and Microstructural Changes Upon Long-Term Isothermal Exposure at 700 and 800 C," *Materials Science and Engineering A*, pp. 124 - 129, 2002.
- [29] Q. Xu, C. H. Lei, and Y. G. Zhang, "TEM in situ Observation of Alpha2 -> Alpha2/Gamma phase transformation in a Ti-45at.%Al alloy," in *Gamma Titanium Aluminides*, Las Vegas, NV, USA, 1995, pp. 189-196.
- [30] M. J. Blackburn, in *The Science, Technology and Applications of Titanium*, R. I. Jaffe and N. E. Promisel, Eds. Oxford: Pergamon Press, 1970, p. 663.
- [31] W. J. Zhang, L. Francesconi, and E. Evangelista, "Precipitation Kinetics of Lamellar (Gamma) Laths in a TiAl-Base Alloy," *Scripta Materialia*, vol. 36, pp. 981-987, 1997.
- [32] S. R. Dey, A. Hazotte, E. Bouzy, and S. Naka, "Development of Widmanstätten laths in a near-[gamma] TiAl alloy," *Acta Materialia*, vol. 53, pp. 3783-3794, 2005.
- [33] F. Appel, U. Brossmann, U. Christoph, S. Eggert, P. Janschek, U. Lorenz, J. Müllauer, M. Oehring, and J. Paul, "Recent Progress in the Development of Gamma Titanium Aluminide Alloys," *Advanced Engineering Materials*, vol. 2, pp. 699 - 720, 2000.
- [34] P. J. Maziasz, R. V. Ramanujan, C. T. Liu, and J. L. Wright, "Effects of B and W Alloying Additions on the Formation and Stability of Lamellar Structures in Two-Phase Gamma-TiAl," *Intermetallics*, vol. 5, pp. 83-95, 1997.
- [35] H. Zhu, D. Y. Seo, K. Maruyama, and P. Au, "Microstructural Stability of Fine-Grained Fully Lamellar XD TiAl Alloys by Step Aging," *Metallurgical and Materials Transactions A*, vol. 36A, pp. 1339-1351, May 2005.
- [36] F. E. Fuchs, "Effect of W Additions to Ti-48Al-2Nb-2Cr Alloys," *Materials Science and Engineering A*, vol. 192/193, pp. 707 - 715, 1995.

- [37] J. Beddoes, P. Au, L. Van de Mosselaer, L. Zhao, and W. Wallace, "Effect of heat treatment on the microstructure of near gamma-TiAl powder alloys," in *Proceedings of the International Symposium on Developments and Applications of Ceramics and New Metal Alloys*, Quebec City, 1993, pp. 435-446.
- [38] G. Cao, L. Fu, J. Lin, Y. Zhang, and C. Chen, "The relationships of microstructure and properties of a fully lamellar TiAl alloy," *Intermetallics*, vol. 8, pp. 647-653, 2000.
- [39] H. Y. Kim and S. H. Hong, "The Effect of Microstructures on Creep Behavior of Ti-48Al-2W Intermetallic Compounds," *Materials Science and Engineering*, vol. A, pp. 788-794, 2002.
- [40] S. Mitao, S. Tsuyama, and K. Minakawa, "Effect of Aluminum Content on Creep Deformation Behaviour of Gamma-Titanium Aluminides," in *Proceedings of the Symposium on Microstructure/Property Relationships in Titanium Aluminides and Alloys presented at the 1990 TMS Fall Meeting*, Detroit, MI, USA, 1991, pp. 297-311.
- [41] J. Beddoes, L. Zhao, P. Au, D. Dudzinski, and J. Triantafillou, "Microstructural Design of Near g-TiAl for Creep Resistance," in *Structural Intermetallics 1997*, Warrendale, PA, 1997, pp. 109-118.
- [42] R. A. Varin and Q. Gao, "The Effect of Chromium on the Microstructure and Micromechanical Properties of TiAl-Base Alloys," *Materials and Manufacturing Processes*, vol. 11, pp. 381 - 410, 1996.
- [43] J. N. Wang and K. Xie, "Refining of Course Lamellar Microstructure of TiAl Alloys by Rapid Heat Treatment," *Intermetallics* 8, pp. 545-548, 2000.
- [44] J. M. K. Wiezorek, X. D. Zhang, M. J. Mills, and H. L. Fraser, "On the Role of Lamellar Interfaces on the Strength and Ductility of Two-Phase Titanium-Aluminum," in *Symposium on High-Temperature Ordered Intermetallic Alloys VIII*, Boston, 1998, pp. KK3.5.1 - KK3.5.8.

- [45] J. Beddoes, D. Dudzinski, and L. Zhao, "Primary Creep of Near Gamma-TiAl Intermetallic," *High Temperature Materials and Processes*, vol. 18, pp. 173-185, 1999.
- [46] G. B. Viswanathan, S. Kartikeyan, M. J. Mills, and V. K. Vasudevan, "Creep Properties of a Fully-Lamellar Ti-48Al-2Cr-2Nb Alloy," *Materials Science and Engineering*, vol. A, pp. 833-837, 2001.
- [47] W. R. Chen, J. Beddoes, and L. Zhao, "Effect of Aging on the Tensile and Creep Behavior of a Fully Lamellar Near Gamma-TiAl Alloy," *Materials Science and Engineering A*, pp. 306-317, 2002.
- [48] H. Zhu, D. Y. Seo, K. Maruyama, and P. Au, "Effect of microstructural stability on creep behavior of 47XD TiAl alloys with fine-grained fully lamellar structure," *Scripta Materialia*, vol. 52, pp. 45-50, 2005.
- [49] H. Zhu, D. Y. Seo, K. Maruyama, and P. Au, "Strengthening of a Fully Lamellar TiAl + W Alloy by Dynamic Precipitation of Beta Phase During Long-Term Creep," *Scripta Materialia*, vol. 54, pp. 425-430, 2006.
- [50] W. F. Smith, *Foundations of Materials Science and Engineering*, 2nd ed. New York: McGraw-Hill, 1993.
- [51] M. F. Ashby and D. R. H. Jones, *Engineering Materials 2; An Introduction to Microstructures, Processing, and Design*. Oxford, England: Pergamon Press., 1998.
- [52] T.-K. Lee, S. K. Hwang, S. W. Nam, and N. J. Kim, "Control of beta phase in an EPM-processed intermetallic compound based on Ti---Al---Mn---Mo," *Scripta Materialia*, vol. 36, pp. 1249-1254, 1997.
- [53] M. A. Muñoz-Morris, I. Gil, and D. G. Morris, "Microstructural Stability of Gamma-Based TiAl Intermetallics Containing Beta Phase," *Intermetallics 13*, pp. 929-936, 2005.

- [54] H. A. Lipsitt, D. Shechtman, and R. E. Schafrick, "Deformation and Fracture of TiAl at Elevated Temperatures," *Metallurgical Transactions A (Physical Metallurgy and Materials Science)*, vol. 6A, pp. 1991-1996, 1975.
- [55] H. Zhang, L. L. He, H. Q. Ye, and D. Y. Seo, "An Analysis of Growth Direction of Beta Phase Precipitates in a TiAlW Alloy," *Scripta Materialia*, vol. 48, pp. 1231-1236, 2003.
- [56] V. Novikov, in *Concise Dictionary of Materials Science* United States of America: CRC Press LLC, 2003.
- [57] P. Wang and V. K. Vasudevan, "Composition Dependence of the Massive Transformation from Alpha to Gamma in Quenched TiAl Alloys," *Scripta Metallurgica et Materialia*, vol. 27, pp. 89-94, 1992.
- [58] U. Prasad and M. C. Chaturvedi, "Influence of Alloying Elements on the Kinetics of Massive Transformation in Gamma Titanium Aluminides," *Metallurgical and Materials Transactions A*, vol. 34A, pp. 2053-2066, Oct. 2003.
- [59] A. Huang, M. H. Loretto, D. Hu, K. Liu, and X. Wu, "The Role of Oxygen Content and Cooling Rate on Transformations in TiAl-Based Alloys," *Intermetallics*, vol. 14, pp. 838-847, 2006.
- [60] F. Herrouin, P. Bowen, and I. P. Jones, "Creep deformation of a fully lamellar gamma based titanium aluminide alloy," Boston, MA, USA, 1997, pp. 287-292.
- [61] U. Brossmann, M. Oehring, and F. Appel, "Microstructure and chemical homogeneity of high Nb gamma based TiAl alloys in different conditions of processing," in *Structural Intermetallics 2001*, Jackson Hole, WY, USA, 2001, pp. 191-200.
- [62] J. N. Wang and K. Xie, "Grain size refinement of a TiAl alloy by rapid heat treatment," *Scripta Materialia*, vol. 43, pp. 441-446, 2000.
- [63] Y. Wang, J. N. Wang, Q. Xia, and J. Yang, "Microstructure refinement of a TiAl alloy by heat treatment," *Materials Science and Engineering A*, vol. 293, pp. 102-106, 2000.

- [64] Q. Xia, J. N. Wang, Y. Wang, and J. Yang, "Effect of heating rate on the grain refinement of a TiAl alloy by cyclic heat treatment," *Materials Science and Engineering A*, vol. 300, pp. 309-311, 2000.
- [65] J. Yang, J. N. Wang, Q. Xia, and Y. Wang, "Effect of cooling rate on the grain refinement of TiAl-based alloys by rapid heat treatment," *Materials Letters*, vol. 46, pp. 193-197, 2000.
- [66] F.-S. Sun, C.-X. Cao, S.-E. Kim, Y.-T. Lee, and M.-G. Yan, "Alloying Mechanism of Beta Stabilizers in a TiAl Alloy," *Metallurgical and Materials Transactions A*, vol. 32A, pp. 1573-1589, July 2001.
- [67] C. Y. Nam, M. H. Oh, K. S. Kumar, and D. M. Wee, "Effect of Nitrogen on the Mean Lamellar Thickness of Fully Lamellar TiAl Alloys," *Scripta Materialia*, vol. 46, pp. 441 - 446, 2002.
- [68] J. Tang, B. Huang, K. Zhou, W. Liu, Y. He, and Y. Liu, "Factors affecting the lamellar spacing in two-phase TiAl alloys with fully lamellar microstructures," *Materials Research Bulletin*, vol. 36, pp. 1737-1742, 2001.
- [69] H. Umeda, K. Kishida, H. Inui, and M. Yamaguchi, "Effects of Al-concentration and lamellar spacing on room-temperature strength and ductility of PST crystals of TiAl," *Materials Science and Engineering A*, vol. A239-240, pp. 336-343, 1997.
- [70] S.-C. Huang, "Alloying Considerations in Gamma-Based Alloys," *Structural Intermetallics*, pp. 299-307, 1993.
- [71] M. Charpentier, D. Daloz, A. Hazotte, E. Gautier, G. Lesoult, and M. Grange, "Study of Microstructure and Solute Partitioning in a Cast Ti-48Al-2Cr-2Nb Alloy by Quenching during Directional Solidification Technique," *Metallurgical and Materials Transactions A*, vol. 34A, pp. 2139-2148, October 2003.
- [72] V. N. Moiseyev, *Titanium Alloys: Russian Aircraft and Aerospace Applications* vol. 5. Boca Raton, FL, United States of America: CRC Press, 2006.

- [73] Y. Mizuhara, K. Hashimoto, and N. Masahashi, "Microstructure and Phase Stability of TiAl-W Ternary Alloy," *Intermetallics*, vol. 11, pp. 807-816, 2003.
- [74] P. L. Martin, M. G. Mendiratta, and H. A. Lipsitt, "Creep Deformation of TiAl and TiAl+W Alloys," *Metallurgical Transactions A (Physical Metallurgy and Materials Science)*, vol. 14A, pp. 2170-2174, 1983.
- [75] D. W. McKee and S. C. Huang, "The Oxidation Behavior of Gamma-Titanium Aluminide Alloys Under Thermal Cycling Conditions," *Corrosion Science*, vol. 33, pp. 1899-1914, 1992.
- [76] C. M. Austin and T. J. Kelly, "Gas Turbine Engine Implementation of Gamma Titanium Aluminide," in *Superalloys 1996*, Warrendale, PA, 1996, pp. 539-543.
- [77] M. F. Stroosnijder, V. A. C. Haanappel, and H. Clemens, "Oxidation behaviour of TiAl-based intermetallics — influence of heat treatment," *Materials Science and Engineering*, vol. A239-240, pp. 842-846, 1997.
- [78] J. Beddoes, L. Zhao, P. Au, and W. Wallace, "The brittle-ductile transition in HIP consolidated near [gamma]-TiAl + W and TiAl + Cr powder alloys," *Materials Science and Engineering A*, vol. 192-193, pp. 324-332, 1995.
- [79] A. M. Hodge, L. M. Hsiung, and T. G. Nieh, "Creep of nearly lamellar TiAl alloy containing W," *Scripta Materialia*, vol. 51, pp. 411-415, 2004.
- [80] D. J. Larson, C. T. Liu, and M. K. Miller, "Microstructural characterization of segregation and precipitation in $\alpha_2 + \gamma$ titanium aluminides," *Materials Science and Engineering*, vol. A239-240, pp. 220-228, 1997.
- [81] P. L. Martin, H. A. Lipsitt, N. T. Nufler, and J. C. Williams, "The effects of alloying on the microstructure and properties of Ti₃Al and TiAl," in *Titanium'80, Science and Technology*, 1980.
- [82] R. Yu, L. L. He, and H. Q. Ye, "Effect of W on structural stability of TiAl intermetallics and the site preference of W," *Physical Review B*, vol. 65, pp. 184102-1 - 184102-5, 2002.

- [83] M. E. Kassner and M.-T. Pérez-Prado, *Fundamentals of Creep in Metals and Alloys*, First ed. Kidlington, Oxford, UK: Elsevier Ltd., 2004.
- [84] R. W. Evans and B. Wilshire, *Introduction to Creep*. London: The Institute of Materials, 1993.
- [85] Y.-W. Kim and F. H. Froes, "Physical Metallurgy of Titanium Aluminides," in *High Temperature Aluminides and Intermetallics*, 1990, pp. 465-492.
- [86] W. Wallace, L. Zhao, J. Beddoes, and D. Morphy, in *Hot Isostatic Pressing '93*, 1993.
- [87] J. M. Overton, "Thermophysical property and phase transformation determination of gamma-TiAl intermetallics," M.App.Sc. thesis, Ottawa: Carleton University, 2006.
- [88] A. Chatterjee, H. Mecking, E. Arzt, and H. Clemens, "Creep Behavior of Gamma-TiAl Sheet Material with Differently Spaced Fully Lamellar Microstructures," *Materials Science and Engineering*, vol. A, pp. 840-846, 2002.
- [89] "Standard Test Methods for Conducting Creep, Creep-Rupture, and Stress-Rupture Tests of Metallic Materials," ASTM International, West Conshohocken, PA ASTM E 139 – 06, 2006.
- [90] R. Kainuma, Y. Fujita, H. Mitsui, I. Ohnuma, and K. Ishida, "Phase Equilibria Among Alpha (hcp), Beta (bcc) and Gamma (L10) Phases in Ti-Al Based Ternary Alloys," *Intermetallics*, vol. 8, pp. 855-867, 2000.
- [91] G. Sreenivasulu, A. K. Singh, N. K. Mukhopadhyay, and G. V. S. Sastry, "Effect of Alloying and Aging on Morphological Changes from Lamellar to Equiaxed Microstructure of Alpha₂ + Gamma Titanium Aluminides," *Metallurgical and Materials Transactions A*, vol. 36A, pp. 2601-2613, 2005.
- [92] P. J. Maziasz, C. T. Liu, and J. L. Wright, "Stability of Ultrafine Lamellar Structures During Aging in Two-Phase Gamma-TiAl Alloys," *Structural Intermetallics*, pp. 245-252, 1997.

- [93] A. Denquin and S. Naka, "Phase transformation mechanisms involved in two-phase TiAl-based alloys--I. Lamellar structure formation," *Acta Materialia*, vol. 44, pp. 343-352, 1996.
- [94] R. E. Smallman and R. J. Bishop, *Modern physical metallurgy and materials engineering : science, process, applications*, 6th ed. Oxford ; Boston: Butterworth Heinemann, 1999.
- [95] H. Zhu, D. Y. Seo, K. Maruyama, and P. Au, "Effect of lamellar spacing on microstructural instability and creep behavior of a lamellar TiAl alloy," *Scripta Materialia*, vol. 54, pp. 1979-1984, 2006.
- [96] S. Karthikeyan, G. B. Viswanathan, P. I. Gouma, V. K. Vasudevan, Y. W. Kim, and M. J. Mills, "Mechanisms and effect of microstructure on creep of TiAl-based alloys," *Materials Science and Engineering A*, vol. 329-331, pp. 621-630, 2002.
- [97] R. Cao, M. X. Lei, J. H. Chen, and J. Zhang, "Effects of Loading Rate on Damage and Fracture Behavior of TiAl Alloys," *Materials Science and Engineering A*, vol. 465, pp. 183-193, 2007.
- [98] J. H. Chen, R. Cao, G. Z. Wang, and J. Zhang, "Study on notch fracture of TiAl alloys at room temperature," *Metallurgical and Materials Transactions A*, vol. 35A, pp. 439-457, 2004.
- [99] M. Yamaguchi, H. Inui, S. Yokoshima, K. Kishida, and D. R. Johnson, "Recent progress in our understanding of deformation and fracture of two-phase and single-phase TiAl alloys," *Materials Science and Engineering: A*, vol. 213, pp. 25-31, 1996.